Search for Cosmic Point Sources of High Energy Neutrinos with the AMANDA-II Detector

D I S S E R T A T I O N

zur Erlangung des akademischen Grades
doctor rerum naturalium
(Dr. rer. nat.)
im Fach Physik

eingereicht an der
Mathematisch-Naturwissenschaftlichen Fakultät I
Humboldt-Universität zu Berlin

von
Dipl.-Phys. Tonio Hauschildt
geboren am 10.04.1975 in Hamburg

Präsident der Humboldt-Universität zu Berlin:
Prof. Dr. Jürgen Mlynek

Dekan der Mathematisch-Naturwissenschaftlichen Fakultät I:
Prof. Thomas Buckhout, PhD

Gutachter:

1. Prof. Dr. Hermann Kolanoski
2. Prof. Dr. Nikolaj Pavel
3. Prof. Dr. Lutz Köpke

eingereicht am:	7. April 2004
Tag der mündlichen Prüfung:	15. Oktober 2004

Abstract

We describe the search for astrophysical sources of high energy neutrinos with the AMANDA-II detector. This detector allows for reconstruction of neutrino induced muon tracks by the Cherenkov radiation emitted by relativistic muons.

We analyze the AMANDA-II data recorded in the year 2000 with a lifetime of 197 days. A large fraction of the background of atmospheric muons can be suppressed by the selection of events reconstructed as upward moving tracks. We develop further quality criteria, which lead to the extraction of a sample of 699 neutrino event candidates, dominated by atmospheric neutrinos. We analyze this data sample in view of significant contributions from neutrino point sources, which would be observable as enhancements of the event density from certain directions.

We have not found a significant indication of the existence of astrophysical high energy neutrino sources, neither by the investigation of source candidates (e.g. Active Galactic Nuclei, microquasars, or supernova remnants), nor by a binned search in the complete Northern sky, nor by the investigation of angular distances between pairs of reconstructed event directions.

Assuming power-law neutrino spectra $\mathrm{d}\Phi_\nu/\mathrm{d}E_\nu \propto E_\nu^{-2}$, we calculate limits on the neutrino fluxes and the neutrino induced muons fluxes from a list of selected neutrino source candidates. The sensitivity of the AMANDA-II detector, i.e. the average neutrino and muon flux limits, amounts to $E_\nu^2 \mathrm{d}\Phi_\nu/\mathrm{d}E_\nu \approx 2 \cdot 10^{-7}$ GeV cm^{-2} s^{-1} and $\Phi_\mu \approx 2 \cdot 10^{-15}$ cm^{-2}s^{-2}, respectively. These are currently the best limits on neutrino fluxes from astrophysical objects in the Northern hemisphere.

Keywords:
AMANDA, neutrinos, astroparticle physics, point sources

Zusammenfassung

Diese Arbeit befasst sich mit der Suche nach astrophysikalischen Punktquellen hochenergetischer Neutrinos mit Hilfe des AMANDA-II-Detektors. Der AMANDA-Detektor erlaubt die Rekonstruktion neutrino-induzierter Myonen durch die Detektion des von diesen Myonen emittierten Cherenkov-Lichts.

Es wird der Datensatz des Jahres 2000 mit einer effektiven Datennahmezeit von 197 Tagen analysiert. Nach der Unterdrückung eines wesentlichen Teils des Untergrundes atmosphärischer Myonen durch Selektion als aufwärts laufend rekonstruierter Ereignisse werden weitere Selektionskriterien entwickelt, um einen Datensatz herauszufiltern, der von durch atmosphärische Neutrinos induzierten Myonen dominiert ist. Diese 699 Ereignisse werden im Hinblick auf signifikante Beiträge von Punktquellen untersucht, d.h. auf Überschüsse der Ereigniskonzentration aus bestimmten Richtungen.

Weder die Betrachtung einer Auswahl möglicher Neutrinoquellen (z.B. aktive galaktische Kerne, Mikroquasare oder Supernova-Überreste), noch eine Suche am gesamten Nordhimmel durch die Platzierung überlappender Suchfenster, noch die Untersuchung der Raumwinkel-Abstände zwischen Paaren selektierter Ereignisse ergeben einen signifikanten Hinweis auf die Existenz von Quellen astrophysikalischer hochenergetischer Neutrinos.

Unter der Annahme eines Neutrinospektrums $\mathrm{d}\Phi_\nu/\mathrm{d}E_\nu \propto E_\nu^{-2}$ werden Flussgrenzen für die Neutrino-Flüsse der ausgewählten Quellenkandidaten sowie für die neutrino-induzierten Myonflüsse angegeben, die im Mittel bei der Sensitivität von $E_\nu^2 \mathrm{d}\Phi_\nu/\mathrm{d}E_\nu \approx 2 \cdot 10^{-7}$ GeV cm^{-2} s^{-1} bzw. $\Phi_\mu \approx 2 \cdot 10^{-15}$ cm^{-2}s^{-2} liegen. Dies sind zur Zeit die besten Grenzen für die Neutrinoflüsse von astrophysikalischen Quellen in der nördlichen Hemisphäre.

Schlagwörter:
AMANDA, Neutrinos, Astroteilchenphysik, Punktquellen

Acknowledgments

I want to thank Prof. Dr. Hermann Kolanoski for taking the responsibility for this thesis and for his interest in an analysis not directly related to his usual research topics. I thank Dr. Christian Spiering for many fruitful discussions, for all the support during my work at DESY Zeuthen and of course for the opportunity to work in the AMANDA collaboration.

Dr. Marek Kowalski pointed me to the AMANDA experiment and provided valuable ideas to different AMANDA analyses. In addition to discussing physics and technical questions. Sebastian Böser repeatedly managed to organize recreational activities within the Zeuthen AMANDA group. Dr. Alexander Biron introduced me to the interesting topic of my analysis. Also the other diploma and PhD students, the post-docs, and the staff members of the AMANDA group in Zeuthen made the work very pleasant and often helped with discussions and encouragement: Markus Ackermann, Dr. Elisa Bernardini, Dr. David Boersma, Dr. Rolf Nahnhauer, Dr. Stefan Schlenstedt, Jutta Stegmaier, and Henrike Wissing.

It was a pleasure to work in close cooperation with David Steele from Madison. All members of the AMANDA collaboration created a very friendly and efficient working atmosphere and made the collaboration meetings as well as the intense working periods at the South Pole enjoyable.

Finally I thank my family and all my friends for their patience during more than three years and for all kinds of support.

Contents

List of Figures

List of Tables

Chapter 1

Introduction

For centuries, astronomers could only observe astrophysical objects which emit electromagnetic radiation in the optical wavelength range. In the previous century, astroparticle physicists discovered also charged particles (protons, heavier ions, and electrons) reaching the earth from the cosmos. Additionally, radio telescopes, satellite experiments, and Cherenkov telescopes extended the spectrum of detectable electromagnetic radiation both to lower and higher energies (up to a few TeV).

Charged cosmic rays have been detected up to energies of about 10^{20} eV. The origin of these highly energetic particles is still not well understood: Are these particles accelerated in the Milky Way or a nearby galaxy? Or are they produced by the decay of hypothetical superheavy particles? Knowledge about the distribution of the sources of high energy particles and especially about the acceleration mechanisms will improve our understanding. Multiwavelength observations of the electromagnetic radiation emitted by galactic and extragalactic sources led to considerable progress in the modelling and classification of these objects. An important question is whether the electromagnetic radiation is created exclusively by acceleration of electrons or if the sources of high energy radiation also accelerate hadrons.

Unlike photons, charged cosmic rays are deflected by interstellar and extragalactic magnetic fields. Therefore, except for the particles with the highest energies ($E \gtrsim 10^{19}$ eV), charged cosmic rays do not point back to their sources. Only with the Pierre Auger Observatory, which will cover an area of 3000 km^2, it might be possible in the near future to accumulate sufficient statistics to detect point sources of charged cosmic rays.

The detection of high energy neutrinos from cosmic accelerators would be an indirect proof for the presence of hadronic acceleration: High energy protons (and other hadrons) would interact with photons or hadronic matter in the vicinity of the acceleration region, and produce – among other particles – charged and neutral pions. In the decay of the charged pions, muon neutrinos, electron neutrinos, and charged leptons are created. Thus, the de-

tection of a significant flux of high energy neutrinos from an extraterrestrial source would indicate the acceleration of hadrons in that source.

Neutrinos have two advantages as astronomical messenger particles:

- Like gamma rays, they are not deflected on their way from the source to the earth.
- They interact only weakly.

The small interaction cross section enables them to escape from dense acceleration regions and to traverse large distances through the intergalactic medium without interactions. On the other hand, the small cross section requires huge detection volumes.

The AMANDA experiment makes use of the Antarctic glacier to measure the Cherenkov light emitted by charged leptons, which originate from charged current interactions of neutrinos with nucleons. High energy muons, produced by interactions of muon-neutrinos, can propagate long distances through the ice. The detection of Cherenkov photons in an array of 677 photomultipliers allows one to reconstruct the direction of the muon track to an accuracy of a few degrees. At neutrino energies $E_\nu \gtrsim 1$ TeV, the muon direction deviates from the neutrino direction by less than 1°, enabling us to approximately reconstruct the initial neutrino direction.

The aim of this work is the search for astrophysical point sources of muon neutrinos. Due to a large background of down-going muons from air showers produced by the aforementioned cosmic rays, we restrict the analysis to sources in the Northern sky. By applying quality cuts, we select a sample of predominantly well reconstructed up-going neutrino induced muon events. We describe different methods to analyze this event sample with respect to statistically significant enhancements of events coming from a certain direction in the sky.

Different models for neutrino production in astrophysical objects are summarized in chapter 2. We describe the principle of neutrino detection and the setup of the AMANDA detector in chapter 3. The Monte-Carlo simulation of signal and background events (chapter 4) is necessary to calculate expected event rates from hypothetical neutrino sources. After a brief review of limit calculation techniques and of statistical methods for point source searches in chapter 5, chapter 6 deals with the selection of candidates for neutrino induced up-going muon events, including the description of reconstruction algorithms and cut optimization and the estimation of systematic uncertainties in the simulation. In chapter 7 we investigate basic properties of the event selection, i.e. the effective detector area, detectable energy range, and the angular resolution. Finally, we apply the methods introduced in chapter 5 to the selected event sample and calculate limits on the neutrino flux and the neutrino induced muon flux for a list of source candidates.

Chapter 2

Sources of high energy neutrinos

The most obvious way to search for high energy neutrinos is to investigate astrophysical objects which are known to emit high energy charged particles or γ-rays. Models for this high energy emission usually assume the acceleration of electrons or protons to ultra-relativistic energies and the subsequent interaction of the highly energetic particles with ambient low energy photons or protons.

This interaction leads to high energy γ-rays produced by inverse Compton scattering of electrons on photons, or to high energy pions produced in photo-meson interactions of protons and photons:

$$p + \gamma \rightarrow \Delta^+ \rightarrow p + \pi^0 \text{ or } n + \pi^+, \tag{2.1}$$

or in proton-proton interactions:

$$p + p \rightarrow \pi^0, \pi^\pm, ... \tag{2.2}$$

High energy γ-rays are then produced in $\pi^0 \rightarrow \gamma + \gamma$ decays, high energy neutrinos in the reaction $\pi^+ \rightarrow \mu^+ + \nu_\mu$, $\mu^+ \rightarrow e^+ + \nu_e + \overline{\nu}_\mu$ (or the charge conjugated reaction).

In the following sections, we describe basic acceleration mechanisms, the classes of possible astrophysical neutrino sources, and high energy neutrino fluxes predicted by specific models for single source candidates. In section 8.2, we will compile a catalog of 30 source candidates, which will be analyzed for a significant signal of extraterrestrial neutrinos.

The last section of this chapter is not concerned with astrophysical neutrinos, but with the main sources of background for the presented analysis, namely muons and neutrinos produced in interactions of cosmic rays with the earth's atmosphere.

2.1 Fermi acceleration

A generic mechanism which is likely to be responsible for the acceleration of particles in supernova remnants or in shocks formed in the relativistic jets of Active Galactic Nuclei and microquasars (see below) is the Fermi acceleration [Fer49]. It can be understood by the analogy of a ball moving between two "mirrors" approaching each other and transferring a certain amount of kinetic energy onto the accelerated particles at each reflection.

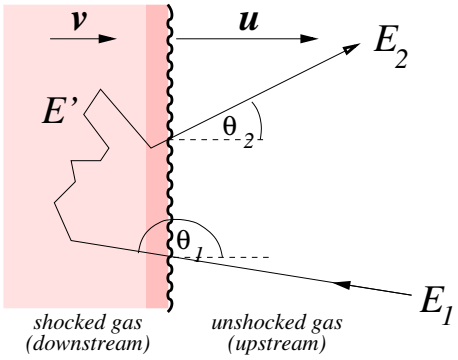

Figure 2.1: Principle of acceleration at a plane shock front moving with the velocity **u**. A particle enters the shocked plasma ("downstream", velocity **v**) with energy E_1, is scattered without collisions keeping the energy E' (in the downstream rest frame) constant, and leaves the shock front with an energy (in the upstream rest frame) $E_2 > E_1$.

Single acceleration cycle

We assume a plane shock front moving with velocity **u**, the shocked gas moving in the same direction with lower velocity **v** as indicated in Fig. 2.1. A relativistic particle ($E \approx pc$) crossing the shock front with an energy E_1 has the energy

$$E' = \gamma E_1 (1 - \beta \cos\theta_1) \tag{2.3}$$

in the "downstream" rest frame of the shocked region. $\gamma = 1/\sqrt{1-\beta^2}$ (with $\beta = |\mathbf{v}|/c$) denotes the Lorentz factor of the downstream region with respect to the "upstream" region in front of the shock. We assume elastic deflection of the particle by turbulent magnetic fields. After several deflections the particle can escape the shocked region. The energy in the upstream rest frame is then

$$E_2 = \gamma E' (1 + \beta \cos\theta_2). \tag{2.4}$$

The average relative gain in energy is obtained [Gai90] from (2.3, 2.4) by averaging over θ_1 and θ_2:

$$\xi \equiv \frac{\langle E_2 - E_1 \rangle}{E_1} = \frac{4}{3}\beta. \tag{2.5}$$

The described scenario of a plane shock front is called *first order Fermi acceleration* in contrast to the mechanism originally proposed by Fermi. For that mechanism he assumed acceleration in moving plasma clouds of finite size. Due to the different geometry (for a plane shock, the angles are restricted to $\cos\theta_1 < 0$ and $\cos\theta_2 > 0$, while for acceleration in clouds the angular range is not limited), this leads to a smaller average energy gain $\xi \approx \frac{4}{3}\beta^2$ of second order in β.

Resulting energy spectrum

In order to calculate the energy spectrum produced by this mechanism, we further assume that after each acceleration cycle the particle will either be elastically scattered back to the shock front and undergo another acceleration cycle or escape from the acceleration region with a probability P_{esc}.

The probability that a particle of initial energy E_0 remains in the acceleration region for n cycles and thus increases its energy to $E_0(1+\xi)^n$ is then $(1-P_{\mathrm{esc}})^n$, resulting in an energy spectrum:

$$\frac{\mathrm{d}N}{\mathrm{d}E} \propto \left(\frac{E}{E_0}\right)^{\alpha}, \tag{2.6}$$

$$\alpha = \frac{\ln(1-P_{\mathrm{esc}})}{\ln(1+\xi)} - 1. \tag{2.7}$$

The spectral index for strong shocks, with the shock velocity $|\mathbf{u}|$ much larger than the velocity of sound c_{sound} in the shocked gas, can be derived to be [Gai90]

$$\alpha \approx -(2 + 4/M^2), \text{ with } M \equiv |\mathbf{u}|/c_{\mathrm{sound}}. \tag{2.8}$$

Comparing this generation spectrum with $\alpha \approx -2.1$ to the observed cosmic ray spectrum, we have to take into account a steepening $\Delta\alpha \approx -0.6$ of the energy spectrum caused by an escape probability from our galaxy rising with energy. The combination of the source spectrum with an energy dependent escape probability can explain the observed approximate power-law

$$\frac{\mathrm{d}N}{\mathrm{d}E} \propto E^{\alpha},\ \alpha \approx -2.7 \tag{2.9}$$

of cosmic rays in the energy range 10 GeV $\lesssim E \lesssim$ 1 PeV.

2.2 Active Galactic Nuclei

Active Galactic Nuclei (AGNs) are the most luminous objects observed in the universe. They are the only extragalactic objects which have definitely been identified as sources of TeV γ-radiation so far. They are believed to be powered by a super-massive ($10^8 M_\odot$) black hole accreting matter from a surrounding galaxy.

AGNs have been observed with very different properties (spectral shape, width of emission lines, variability of the emitted γ-ray spectrum). It is believed that the diversity in appearance originates from a similar setup principle, viewed under different conditions: the system of black hole and accretion disk is surrounded by a dust "torus". The accreted matter provides energy for the acceleration of electrons and possibly of hadrons to relativistic energies, causing the formation of two jets emitted along the symmetry axis.

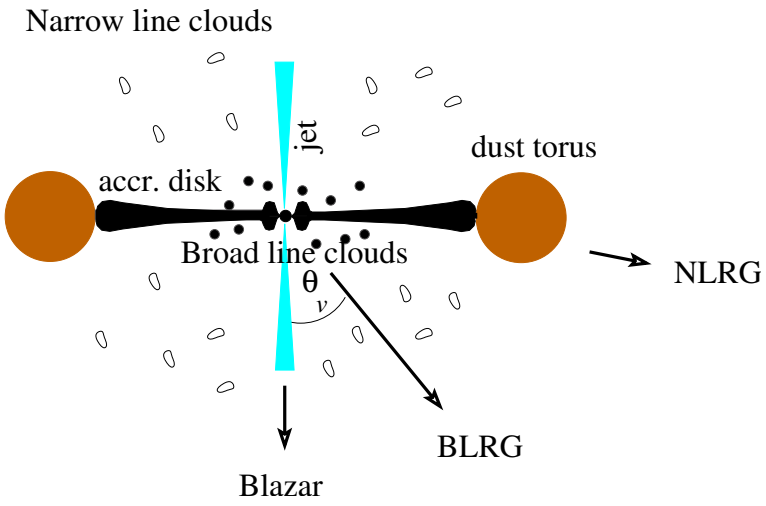

Figure 2.2: Sketch of an AGN according to the unification model. At large viewing angles, only narrow emission lines from clouds at a large distance from the accretion disk can be observed. The gas clouds close to the disk showing broad emission lines become visible only at intermediate viewing angles. If the line of sight to the earth coincides with the jet axis within about 10°, the beamed radiation from a relativistic jet is observed.

The different types of observed AGN phenomena have been combined in a unified model [Pad99, BD02] predicting spectral shapes which depend on the viewing angle between the jet axis and the line of sight: for large viewing angles $\theta_v \approx 90°$, the central source is obscured by the torus as demonstrated in Fig. 2.2. In contrast to these NLRGs (narrow line radio galaxies), BLRGs (broad line RGs) are observed with the line of sight oriented closer to the

jet axis[1] ($20^\circ \lesssim \theta_v \lesssim 40^\circ$). This allows the sight onto fast moving gas clouds close to the accretion disk featuring Doppler broadened emission lines. At still smaller angles ($\theta_v \lesssim 20^\circ$), the spectrum is dominated by non-thermal emission from the jets. AGNs viewed under small angles, called blazars, have comparatively high observable luminosities: if the velocity of the jet plasma is βc, $\gamma = (1-\beta^2)^{-1/2}$, the observed luminosity is enhanced by a factor $L_{\rm obs}/L_{\rm emit} = \delta^3$ compared to the emitted luminosity in the rest frame of the emission region. The Doppler factor $\delta = (\gamma(1-\beta\cos\theta_v))^{-1}$ typically reaches values of $\delta \approx 10$ (e.g. for $\gamma \approx 10$, $\theta_v \approx 5^\circ$).

The spectrum of electromagnetic radiation emitted by blazars shows two humps, one synchrotron peak at radio to soft X-ray frequencies and one peak at energies up to $\mathcal{O}(1$ TeV). Models which explain the high energy emission are separated into leptonic and hadronic models. Leptonic models assume that relativistic electrons interact with ambient photons (either from synchrotron radiation in the jet or from external UV photon fields [DS93]) by inverse Compton scattering. With the observations so far it cannot be determined whether this is the only mechanism of TeV γ-ray production or if also the acceleration of protons and subsequent photo-meson production leads to high energy γ-rays from π^0-decay. Since the simultaneously produced charged pions would decay and produce neutrinos (as well as muons and electrons), the detection of a neutrino flux associated with a TeV blazar would indicate the presence of hadronic acceleration.

Neutrino production is possible in two different regions of the AGN: The "core models" assume the acceleration of protons to relativistic energies in shock fronts in the accretion disc or in the jets close to the central black hole. Interaction of the high energy protons with matter in the accretion disk [NMB93] or with thermal photons [SS96] leads to neutral and charged pion production and subsequently to high energy neutrinos and photons. Photons from π^0 decays cascade down to X-ray energies by pair-production. Neutrino fluxes in these models can therefore be estimated by normalization of the model parameters to the observed X-ray flux. The expected neutrino flux for the AGN 3C273 is shown in Fig. 2.3 for both interaction with matter (a) and with photons (b) from the accretion disk.

In the other class of AGN models ("jet models"), neutrino emission is expected from protons accelerated in the relativistic jets and interacting with ambient photons (e.g. synchrotron photons from co-accelerated electrons). An estimation for the neutrino flux originating from proton acceleration in the jet of 3C273 is shown by curve (c) in Fig. 2.3. An interesting source of high energy γ-radiation and possibly of neutrinos is M87, a nearby AGN at redshift $z = 0.004$. This source has been discussed as a possible origin of the highest energy cosmic rays [PDR03], and its γ-ray flux and the expected

[1] Radio-quiet AGNs are similarly subdivided into Seyfert 1 (if broad emission lines are observed) and Seyfert 2 (showing only narrow emission lines) galaxies.

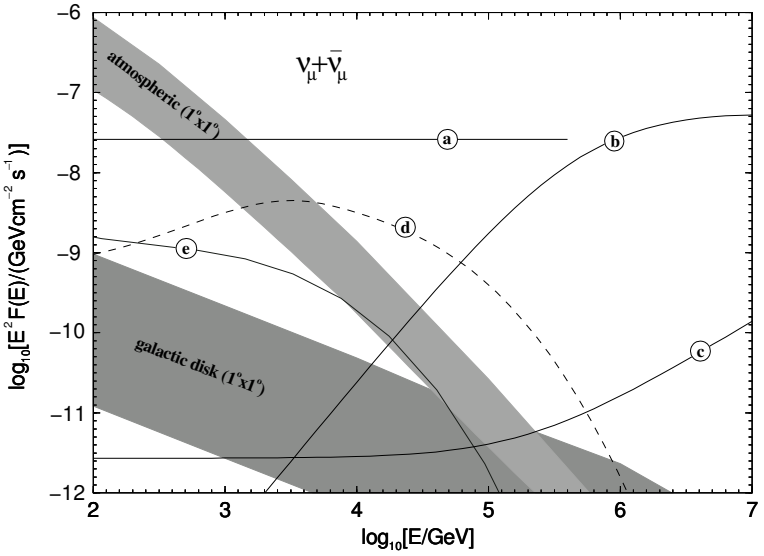

Figure 2.3: Expected neutrino fluxes from galactic and extragalactic source candidates. a) pp interactions in the core region of 3C273 [NMB93], b) pγ interactions in the 3C273 core [SS96], c) neutrino production in the jet of 3C273 [Man93], d) neutrino emission from the Crab nebula [BP97], e) neutrino emission estimated based on the γ-ray flux expected from Cassiopeia A [AATV00]. See text for details. The shaded areas show the already detected flux per square degree of atmospheric neutrinos from interactions of cosmic rays with the earth atmosphere and the expected neutrino flux from cosmic rays interacting with the galactic disk. Figure adapted from [LM00].

neutrino flux have been modeled according to the synchrotron proton blazar (SPB) model: in the SPB model γ-rays are assumed to be produced in the jet by the decay of pions from $p\gamma$ interactions as well as by synchrotron emission from high energy protons and muons. The neutrino flux expectation depends on the relative contributions of $p\gamma$ interactions and synchrotron radiation, i.e. on the density of (synchrotron) target photons for the $p\gamma$ interactions. The largest neutrino flux expected in the SPB model, which is compatible with the observed radio to X-ray emission, is below the sensitivity of the future Icecube detector [A$^+$04b] of $E^2 \mathrm{d}N_\nu/\mathrm{d}E = 5.5 \cdot 10^{-9}$ GeV cm^{-2} s^{-1}. The recent detection of γ-rays with energies above 730 GeV [A$^+$03a] and the proximity of this source to the earth however motivate the addition of this AGN to the source catalog.

Although AGN observations can be explained quite consistently in the unified scheme (summarized by Fig. 2.2), the basic process of the formation of relativistic jets is not yet understood. One possibility, under the assumption of a magnetic field rotating with the accretion disk, is the acceleration of charged particles in the electric field induced by the rotating magnetic field [CO96]. Another model, the Blandford-Znajek process [BZ77] explains

the emission of electromagnetic radiation and relativistic electron-positron plasma by the extraction of rotational energy from a rotating black hole. Hadronic acceleration would not take place in this model.

Preferred γ-ray energy range for neutrino emission

A possible approach to select AGNs with possible neutrino emission would be to choose the sources from which γ-rays have been observed at the highest energies: Markarian 421 and 501, 1ES 1426+428, 1ES 2344+514, and 1ES 1959+650 have been detected by γ-ray telescopes at energies up to $E_\gamma \approx 10$ TeV.

However, a consideration about $p\gamma$ interaction lengths (relevant for neutrino production in hadronic accelerators) and photon absorption lengths due to $\gamma\gamma$ interaction (reducing the observable γ-ray flux) leads to a preference of AGNs emitting photons at lower energies [NS02]: it is based on a model [N$^+$02] supported by X-ray observations of uniform synchrotron emission up to distances of 100 kpc from the core of the AGN, which assumes the production of γ-rays with $E_\gamma > 100$ TeV in the core region. For the efficient production of high energy photons by interaction of accelerated protons and soft photons of density n_{soft} in the central region, the mean free path $(\sigma_{p\gamma} n_{\text{soft}})^{-1}$ of the protons has to be smaller than the core region. On the other hand, so that TeV photons produced in the core can escape, the $\gamma\gamma$ interaction length $(\sigma_{\gamma\gamma} n_{\text{soft}})^{-1}$ must be larger than the core size. However, the comparison of the cross sections $\sigma_{\gamma\gamma} \approx 7 \cdot 10^{-25}$ cm^2 and $\sigma_{p\gamma} \approx 10^{-28}$ cm^2 leads to the conclusion that if TeV photons escape the core region, the density of the ambient photon field is too low for neutrino production.

Therefore, additionally to the blazars detected at TeV energies, we will search for high energy neutrinos from seven blazars emitting γ-rays at GeV energies and fulfilling further criteria [NS02] for efficient neutrino production.

2.3 Microquasars

Microquasars are galactic binary objects emitting X-ray radiation and producing relativistic jets. Similarly to AGNs, microquasars can be explained by a compact object (in this case a neutron star or solar mass black hole) with an accretion disk formed by matter falling from a companion star onto the compact object. Based on the assumption of both proton and electron acceleration at internal shocks in relativistic jets [LW01], expected neutrino fluxes from photo-meson production have been estimated [D$^+$02] using a lower limit for the kinetic jet power calculated from observed jet parameters (Lorentz factor, viewing angle, distance of the microquasar to the earth, size of the emission region and the measured radio flux density).

For the microquasar SS 433 a comparatively high neutrino induced muon flux of $\Phi_\mu = 0.8 \cdot 10^{-15}$ cm^{-2} s^{-1} resulting in 252 events per km^2 and year is expected. This source is especially interesting since the observation of

Doppler shifted H_α emission lines [M$^+$79] indicates proton acceleration in relativistic jets.

2.4 Supernova Remnants

A supernova can occur when a star gradually burns its hydrogen to helium, then to carbon etc. The burning of heavier elements begins in the center and proceeds in shells to the outer regions of the star. Finally, a core of iron is built. Before this stage, an equilibrium of radiation and gravitational pressure is sustained. Once an iron core is created, no more energy can be released in nuclear fusion in the central region, and the star will suffer a gravitational collapse: matter will be contracted in the center to a density similar to the densities of nuclei, if the mass of the progenitor star exceeds about 8 $M_\odot$.

The collapse leads to a shock wave ejecting the outer shell of the star at velocities of about 10^4 km/s, while a neutron star forms in the center. Most of the energy released in the collapse is emitted as neutrinos of energy ≈ 10 MeV. These neutrinos are detectable in the AMANDA detector [F$^+$03], but their low energy does not allow for directional reconstruction. Acceleration at the shock front of the ejected shell can create high energy particles which are believed to contribute significantly to the observed cosmic ray spectrum up to the "knee" ($\approx 10^{15}$ eV) [LM00].

Observations of supernova remnants (SNR) from radio to sub-millimeter wavelengths are interpreted as synchrotron radiation from electrons accelerated to relativistic energies. In the case of the SNR Cassiopeia A, also hard X-rays were detected. Assuming that these X-rays originate from synchrotron radiation as well, one can calculate the underlying electron energy spectrum [AATV00]. Bremsstrahlung and inverse Compton scattering of the electrons with ambient photons lead to high energy γ-ray emission, which however is low compared to an observation of γ-rays above 1 TeV with the HEGRA Cherenkov telescope system [A$^+$01a]. The observation is consistent with the additional production of high energy γ-rays by the decay of neutral pions originating from protons accelerated to $\mathcal{O}(10$ TeV) [BPV03]. High energy neutrino emission is expected from the decay of charged pions. Fig. 2.3 (e) shows an estimation of the neutrino flux from Cassiopeia A based on an estimation of the γ-ray flux from π^0 decay. Although the neutrino flux expected according to this model would be too low for a detection, we include Cassiopeia A in the list of neutrino source candidates due to the indication of hadronic acceleration in this source.

2.5 Pulsars

Related to supernovae, acceleration to high energies is also possible in pulsars, which emit pulses of electromagnetic radiation repeating at a period of down to 1 ms, first observed in 1967 at radio frequencies. They are quickly rotating neutron stars, which obtained a large rotational frequency and presumably a magnetic field of $\gtrsim 10^8$ T during the collapse of a supernova. The co-rotating magnetic field creates large electric potential differences by which charged particles can be accelerated to $\mathcal{O}(10^{18}$ eV). Neutrinos can be produced due to interaction of relativistic hadrons with the pulsar's environment. The expected neutrino flux has been explicitly calculated for the Crab pulsar [BP97] assuming the production of energetic neutrons by interaction of accelerated nuclei with a radiation field surrounding the pulsar. Protons from neutron decay inside the Crab nebula would then produce γ-rays and neutrinos by interaction with the matter in the nebula. The expected neutrino flux exceeds the atmospheric neutrino background in a 1° circular bin at neutrino energies above 5 TeV (cf. Fig. 2.3).

Two further objects belonging to the class of pulsars are included in the list of neutrino candidates used for this analysis: Geminga and SGR 1900+14. The former is one of the closest known neutron stars ($\approx$ 100 pc distance) and has been detected in γ-rays above 50 MeV. The latter is a soft gamma repeater (emitting bunches of low energy gamma rays) identified as a magnetar [K$^+$99] (a pulsar with extremely strong magnetic field $> 10^{10}$ T).

2.6 Individually selected neutrino source candidates

For the classes of astrophysical objects described so far, general models of high energy neutrino production exist. This analysis will also investigate a small number of individually selected neutrino source candidates:

- Two UHE cosmic ray triplets. A cluster analysis [U$^+$00] of ultra-high energy cosmic rays detected by four air shower experiments revealed several multiplets of cosmic rays with energies above 40 EeV, including two triplets separated by less than 2° in space angle. Since the deflection of cosmic rays with an energy above 10^{19} eV in the intergalactic magnetic field is small, the origin of the observed events might be sources of hadronic acceleration possibly implying high energy neutrino production.

- Blazars detected by EGRET [H$^+$99] in γ-rays of energies above 100 MeV are contained in the list of GeV emitting blazars. Additionally, 3EG J0450+1105 has been included in the list of source candidates be-

cause of its relatively strong detected flux of $1.1 \cdot 10^{-6}$ photons cm^{-2} s^{-1} above 100 MeV.

- NGC 1275 has been selected as the closest QSO (quasi-stellar object, an unresolved AGN with broad emission lines) at a redshift $z = 0.018$.
- Cygnus OB2 is a region of young stars, where recently a TeV γ-ray source (J2032+4131) has been detected by the HEGRA Cherenkov telescope array [A$^+$02]. Subsequent observations [B$^+$03b] of the source region by the Chandra X-Ray Observatory and the VLA radio telescope revealed a broadband spectrum that indicates a hadronic origin of the TeV γ-rays and therefore a possible high energy neutrino emission.

2.7 Further neutrino source candidates

The subject of this work is the search for steady, point-like sources of high energy neutrinos (or sources which are flaring over several weeks with accordingly higher maximum flux). For completeness we mention two other hypothetical point-like sources of high energy neutrinos: Gamma Ray Bursts (GRBs) and WIMP annihilation in the sun or in the center of the earth. For these sources, other dedicated analyses are being performed, which make use of additional timing information in the case of GRBs, and are optimized for lower neutrino energies (compared to the presented analysis) in the case of the search for neutrinos from WIMP annihilation.

2.7.1 Gamma Ray Bursts

Gamma Ray Bursts show a large gamma ray luminosity over a short time scale of milliseconds to a few seconds. Observations of optical to radio afterglows revealed that these events occur at cosmic distances leading to an estimate of the total released energy of $\mathcal{O}(10^{51})$ erg. The "fireball shock model" [MR93] explains the large luminosity and the short time scale by the formation of a relativistically expanding plasma, moving with typical Lorentz factors of $\Gamma \approx 300$. Acceleration of electrons at shock waves in the expanding fireball causes the emission of synchrotron radiation in the magnetic field of the fireball and thus explains the observed keV to MeV radiation. Protons accelerated in the shock region would interact with the synchrotron photons resulting in the emission of a burst of neutrinos with energies of about 100 TeV [WB97].

2.7.2 WIMP annihilation

The cosmological parameters show a discrepancy between the baryonic matter density $\Omega_B \approx 0.04$ (in units of the critical density required for a flat

universe) and the total matter density $\Omega_m \approx 0.27$. Candidates for the missing dark matter are weakly interacting massive particles (WIMPs), for example the neutralino χ as the lightest super-symmetric particle. If neutralinos lose energy by weak interactions in massive objects, e.g. in the earth, the sun, or in the galactic center, they may be gravitationally trapped close to the centers of these objects. Annihilation of neutralinos (e.g. via $\chi\chi \rightarrow W^+W^-$ or $q\overline{q}$) and subsequent decay of the produced particles would lead to a flux of high energy neutrinos escaping from the central dense region. However, since neutralino masses below 1 TeV are favored [JKG96], the energies of neutrinos from neutralino annihilation are relatively low compared to neutrino energies from proton acceleration in astrophysical objects. This requires a dedicated analysis with high reconstruction and cut efficiency at low energies to place limits on the neutrino flux from WIMP annihilation in the earth [Olb03].

2.8 Atmospheric muons and neutrinos

Cosmic rays hitting the earth's atmosphere lead to the production of mesons which decay or undergo further interactions with nitrogen and oxygen nuclei. The relative probabilities for a decay or an interaction depend on the meson energy E, since the mean range d after which the particle decays increases linearly with E: $d = \gamma c\tau, \gamma = E/m_{\mathrm{meson}}$. The interaction length is only weakly energy dependent. Atmospheric muons are created in pion and kaon decays with an energy dependence approximately following the primary spectrum $\mathrm{d}N_\mu/\mathrm{d}E_\mu \propto E_\mu^{-2.7}$ at energies below 100 GeV. The spectrum steepens to $E_\mu^{-3.7}$ at larger energies due to the smaller interaction length of pions compared to their decay length. With a mean range of about 2 km w.e. at 1 TeV, a substantial fraction of atmospheric muons generated at zenith angles $\theta \lesssim 80^\circ$ penetrates the South Polar ice and triggers the AMANDA detector (described in the following chapter) with a rate from 54 to 69 Hz. The variation of the trigger rate is caused by seasonal changes of the atmospheric density, since a higher density in the winter reduces the decay probability of pions and kaons compared to their interaction probability.

Together with the muons, atmospheric neutrinos are created in the decay of pions and kaons with a similar spectral shape $\mathrm{d}N_\nu/\mathrm{d}E_\nu \propto E_\nu^{-3.7}$ at energies $E_\nu \gg 100$ GeV. While the atmospheric muon flux at a depth of about 2 km is strongly suppressed at zenith angles $\theta \gtrsim 80^\circ$ due to the large distance traveled by the muons in a dense medium (e.g. in ice), the zenith dependence of atmospheric neutrinos is rather weak, so that upward moving high energy muons can only originate from atmospheric neutrinos or neutrinos from other not yet detected sources, e.g from astrophysical neutrino point sources.

Chapter 3

Neutrino Detection

The cross section for neutrino-nucleon interactions is small, but in a large volume of e.g. water or ice the interaction probability is large enough for the detection of atmospheric and possibly of extraterrestrial neutrinos. In a charged current interaction of a muon-neutrino, a muon of comparable energy is produced. This muon, moving relativistically through the ice, emits Cherenkov radiation which can be detected together with Cherenkov radiation from particles generated in energy loss processes of the muon.

In the following sections, we describe the kinematics of the interaction processes as well as the consequences of neutrino oscillations changing the flavor composition of astrophysical neutrino fluxes. After a brief review of the muon energy loss processes, including the emission of Cherenkov light, we come to the layout and functionality of the AMANDA detector.

3.1 Interaction of neutrinos with nucleons

Neutrinos interact with matter by weak interactions with nucleons or electrons:

$$\begin{aligned} \nu_\mu + N &\to \mu^- + X, \\ \nu_\mu + N &\to \nu_\mu + X, \\ \nu_\mu + e^\pm &\to \nu_\mu + e^\pm. \end{aligned}$$

The charge conjugated reactions and corresponding reactions for electron and tau neutrinos take place as well. For the detection of muon tracks, only the first (charged current) interaction is relevant. The differential cross section for this reaction with an isoscalar nucleon is [G$^+$98]

$$\frac{\mathrm{d}^2\sigma}{\mathrm{d}x\mathrm{d}y} = \frac{2G_F^2 M E_\nu}{\pi} \left(\frac{M_W^2}{Q^2 + M_W^2} \right)^2 (xq(x,Q^2) + x\overline{q}(x,Q^2)(1-y)^2). \quad (3.1)$$

Here $-Q^2$ is the squared 4-momentum transfer from the neutrino to the nucleon, M the nucleon mass, M_W the W boson mass, and G_F the Fermi

coupling constant of the weak interaction. The Bjorken scaling variables $x = Q^2/2M(E_\nu - E_\mu)$ and $y = 1 - E_\mu/E_\nu$ describe the reacting parton's fraction of the nucleon momentum and the fraction of the neutrino energy transferred to the muon, respectively. q and $\overline{q}$ are the parton density functions of (valence and sea) quarks and (sea) anti-quarks in a proton. The total cross section, shown in Fig. 3.1, increases approximately linearly with the neutrino energy below $\mathcal{O}(1\text{ TeV})$, and $\sigma_{\text{CC,NC}} \propto E_\nu^{0.36}$ at $E_\nu > 10$ TeV. The interaction length $\rho\Lambda = \frac{\rho}{\sigma_{\text{tot}}(E_\nu) n_N}$, where n_N is the number density of nucleons, is listed in Tab. 3.1 for different neutrino energies: at ultra-high energies ($E_\nu >$1 EeV), neutrinos are almost completely absorbed when traversing a distance of the earth diameter in dense matter. Neutrinos of 1 TeV energy cross the earth with negligible interaction probability.

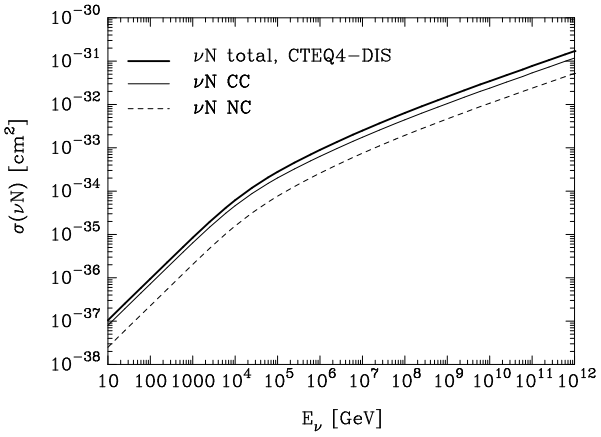

Figure 3.1: Energy dependence of the cross sections for the charged current (CC) reaction $\nu + N \to l + X$ (where l is the lepton of the same flavor as the neutrino), the neutral current (NC) reaction $\nu + N \to \nu + X$ and the sum of both cross sections. The CC and NC anti-neutrino nucleon cross sections are smaller by a factor of about 2 at low energies ($E_\nu \approx 10$ GeV). At large neutrino energies, $E_\nu \gtrsim 10^6$ GeV, interactions with sea quarks and anti-quarks dominate, resulting in approximately equal cross sections. Figure taken from [G+98].

E_ν [GeV]	10^3	10^6	10^9
$\sigma_{\text{tot}}(\nu N)$ [cm^2]	$8.4 \cdot 10^{-36}$	$8.9 \cdot 10^{-34}$	$1.5 \cdot 10^{-32}$
$\rho\Lambda$ [km w.e.]	$2.0 \cdot 10^6$	$1.9 \cdot 10^4$	$1.1 \cdot 10^3$

Table 3.1: Neutrino-nucleon interaction lengths at different energies.

The knowledge of the differential νN cross section (3.1) and the cross section for $\overline{\nu} N$ interactions[1] allows to calculate the mean scattering angle

[1]The expression for the differential cross section of antineutrino-nucleon interactions is

$\theta_{\nu\mu}$ between initial neutrino and produced muon. This is important for the detection of neutrino point sources, since in neutrino telescopes like AMANDA only the muon direction can be reconstructed, so that the angular resolution is eventually limited by the scattering angle.

The scattering angle can be derived in the following way:

$$\begin{aligned} -Q^2 &= (p_\nu - p_\mu)^2 && (3.2)\\ &= m_\nu^2 + m_\mu^2 - 2(E_\nu E_\mu - |\mathbf{p}_\nu||\mathbf{p}_\mu|\cos\theta_{\nu\mu}) && (3.3)\\ &\approx -2E_\nu E_\mu(1-\cos\theta_{\nu\mu}), && (3.4) \end{aligned}$$

where we have approximated $m_\nu \approx 0$ and $m_\mu \approx 0$. Therefore, the mean angle is obtained by averaging

$$\begin{aligned} \theta_{\nu\mu} &\approx \sqrt{2-2\cos\theta_{\nu\mu}} && (3.5)\\ &\approx \sqrt{\frac{Q^2}{E_\nu E_\mu}} && (3.6)\\ &= \sqrt{\frac{2x(1-y)}{y}}\sqrt{\frac{M}{E_\nu}}, && (3.7) \end{aligned}$$

weighted with the differential cross section:

$$\langle\theta_{\nu\mu}\rangle = \frac{\int\int \frac{\mathrm{d}^2\sigma}{\mathrm{d}x\mathrm{d}y}\theta_{\nu\mu}\mathrm{d}x\mathrm{d}y}{\int\int \frac{\mathrm{d}^2\sigma}{\mathrm{d}x\mathrm{d}y}\mathrm{d}x\mathrm{d}y}. \qquad (3.8)$$

In the energy range 10 GeV $\lesssim E_\nu \lesssim$ 3 TeV, the W propagator can be approximated by unity in the allowed kinematic range, and according to (3.7), $\langle\theta_{\nu\mu}\rangle \propto \sqrt{\frac{M}{E_\nu}}$. For large neutrino energies, the Q^2 dependence of the propagator suppresses large scattering angles resulting in a stronger decrease with the neutrino energy. A more precise description of the energy dependence of the scattering angle can be obtained using the full information of the quark distribution functions. Using the ANIS [GK03] neutrino simulation, the results shown in Fig. 3.2 (solid curve) are obtained, which are in good agreement with the previously calculated $1/\sqrt{E_\nu}$ dependence.

Also shown is the scattering angle for events which trigger the AMANDA detector and therefore have a muon energy above a threshold of about 100 GeV and which survive weak quality cuts (reconstructed track length larger than 50 m). For a fixed neutrino energy, the probability that a generated muon triggers the detector and passes the quality cuts increases with the muon energy due to the increased muon range. Since the scattering angle decreases with the muon energy, the mean scattering angle is reduced by the triggering condition and the quality cuts. In [LM00], the mean scattering

similar to (3.1), only the parton density functions $q(x,Q^2)$ and $\overline{q}(x,Q^2)$ are interchanged.

angle is estimated to be $\langle\theta_{\nu\mu}\rangle \approx 0.7^\circ \cdot (E_\nu/1\ \mathrm{TeV})^{-0.7}$ independent of a certain neutrino telescope setup. This estimate (dotted curve) is a good approximation to the AMANDA-II result in the energy range $10^2 - 10^6$ GeV.

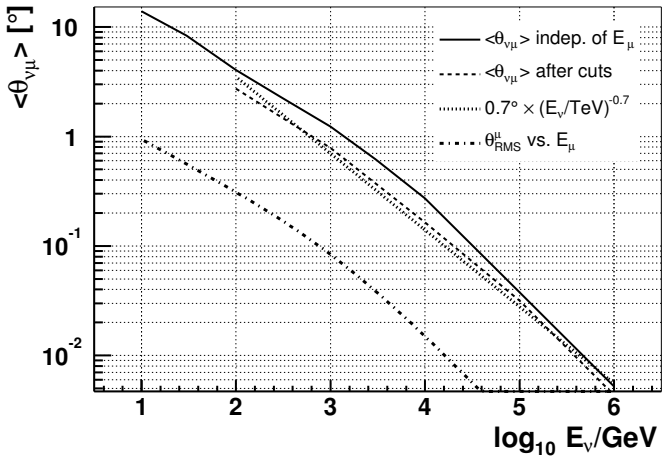

Figure 3.2: Energy dependence of the scattering angle between neutrino and muon. The solid curve shows the decrease of the mean scattering angle (approximately $\propto 1/\sqrt{E_\nu}$ at $E_\nu \lesssim 3000$ GeV) taking into account all neutrino-nucleon interactions, independently of the resulting muon's energy. The dashed curve represents the mean scattering angle after trigger and quality cuts. The parameterization in [LM00] is shown by the dotted line. The dependence of the muon scattering angle (section 3.3.1) on the muon energy is plotted by the lowest curve.

3.2 Vacuum oscillation of neutrinos

Detectable neutrino fluxes are affected by oscillation of neutrinos of one flavor into another. This oscillation is expected if the neutrino eigenstates of the weak interactions $|\nu_\alpha\rangle$ (α=e, μ, τ) are not identical to the mass eigenstates $|\nu_i\rangle$ ($i = 1, 2, 3$), but superpositions:

$$|\nu_\alpha\rangle = \sum_i U_{\alpha i} |\nu_i\rangle. \tag{3.9}$$

The different time development of the mass eigenstates

$$|\nu_i(t)\rangle = e^{-iE_i t/\hbar}|\nu_i(0)\rangle, E_i = \sqrt{p^2c^2 + m_i^2c^4} \approx pc + \frac{m_i^2 c^3}{2p} \tag{3.10}$$

leads to time dependent probabilities for a neutrino of initial flavor α to be detected as a neutrino of flavor β.

In the hypothetical case of 2-flavor mixing, e.g. $\nu_{e,\mu}$ being superpositions of $\nu_{1,2}$ whereas $\nu_\tau \equiv \nu_3$, the probability that a muon-neutrino of energy E oscillates to an electron neutrino after a traveled distance L is

$$P_{\mu\to e}(L) = \sin^2 2\theta_{12} \sin^2 \frac{\Delta m^2_{12} c^3 L}{4E\hbar} \tag{3.11}$$

where Δm^2_{12} is the difference of the squared masses of ν_1 and ν_2 and the mixing angle θ_{12} determines the coefficients $U_{\alpha i}$:

$$\begin{pmatrix} U_{e1} & U_{e2} \\ U_{\mu 1} & U_{\mu 2} \end{pmatrix} = \begin{pmatrix} \cos\theta_{12} & \sin\theta_{12} \\ -\sin\theta_{12} & \cos\theta_{12} \end{pmatrix}. \tag{3.12}$$

The parameters[2] Δm_{ij} and θ_{ij} are constrained by measurements of the atmospheric [F$^+$98] and solar [A$^+$01b, F$^+$02] neutrino fluxes and by measurements of neutrino fluxes from nuclear reactors [A$^+$99, E$^+$03].

Astrophysical neutrino fluxes are typically produced in pion decays $\pi^+ \to \mu^+ + \nu_\mu$, $\mu^+ \to e^+ + \nu_e + \overline{\nu}_\mu$ (or charge conjugated) with a flavor ratio $\nu_e : \nu_\mu : \nu_\tau = 1 : 2 : 0$ (denoting the proportions of summed neutrino and anti-neutrino flux of each flavor). Taking into account the experimental constraints on the mixing parameters, this ratio is converted to approximately $1 : 1 : 1$ over astrophysical distances [AJJ00]. This is of importance for comparing the flux limits to be derived in this analysis to models for specific sources: the flux limits are calculated for the muon-neutrino flux *arriving at the earth*, which is half of the muon neutrino flux emitted from the source.

3.3 Muon propagation

A muon traveling through matter loses energy by ionization of the surrounding matter and by stochastic processes like bremsstrahlung, e^+/e^- pair production and photo-nuclear interaction.

The energy loss due to ionization proceeds quasi continuously according to the Bethe-Bloch formula (e.g. in [H$^+$02]) at a rate of $\mathrm{d}E/\mathrm{d}X \approx -2.6$ MeV/(g cm^{-2}) for energies $E \gtrsim 10$ GeV [RC01].

The discrete energy losses increase approximately linearly with energy, resulting in a total average energy loss of

$$\mathrm{d}E/\mathrm{d}X = -a - bE \tag{3.13}$$

with $a \approx 2.6$ MeV/(g cm^{-2}) and $b \approx 4 \cdot 10^{-6}$/(g cm^{-2}) for the energy loss in ice. The coefficients slightly depend on the muon energy and on the traversed material.

[2] The case of oscillation between three neutrino flavors can be described by three squared mass differences Δm_{ij} and three mixing angles θ_{ij}. If CP conservation is not valid in neutrino interactions, an additional phase factor is required.

Integrating (3.13) for a muon of initial energy E_i and final energy E_f, assuming constant a and b and neglecting fluctuations, results in a muon range of

$$R = \frac{1}{b} \ln \frac{E_i + E_c}{E_f + E_c}. \tag{3.14}$$

The critical energy E_c at which continuous and stochastic energy losses are equal is $E_c = a/b \approx 650$ GeV.

The range (3.14) in ice varies from about 2 km w.e. to 35 km w.e. for muons of initial energies between $E_i = 1$ TeV and $E_i = 1$ EeV. As shown in Fig. 3.3 for the muon range in rock, the individual ranges of single muons of the same energy deviate considerably from the range (3.14), and the mean range is smaller than this value. The fluctuations of the energy loss are taken into account in the simulation of the muon propagation.

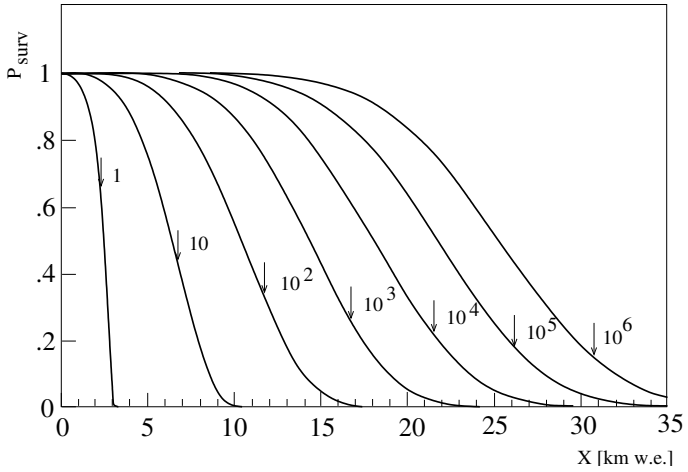

Figure 3.3: Probabilities for muons of different energies (1-10^6 TeV) to travel a range X in rock. The arrows (with energies written in TeV) indicate the range in absence of fluctuations from the average energy loss (3.13). Figure adapted from [LS91].

3.3.1 Muon scattering

Charged particles moving through matter undergo multiple small angle deflections due to Coulomb scattering off nuclei. The distribution of the scattering angle projected to a plane containing the initial muon track is approximately described by a Gaussian distribution with a width [H+02]

$$\theta_{RMS} = \frac{13.6 \text{ MeV}}{\beta cp} \sqrt{\frac{x}{X_0}} (1 + 0.038 \ln \frac{x}{X_0}), \tag{3.15}$$

where x/X_0 is the distance traveled by the muon of momentum p in units of the radiation length $X_0 \approx 36$ g cm^{-2}. The muon scattering angle calculated

for the energy dependent muon range (3.14) is compared to the neutrino muon scattering angle $\langle\theta_{\mu\nu}\rangle$ in Fig. 3.2. θ_{RMS} is small compared to $\langle\theta_{\mu\nu}\rangle$ for neutrinos and muons of comparable energy; the multiple scattering of muons is therefore not included in the AMANDA event simulation.

3.4 Cherenkov radiation

Charged particles traveling through a medium with refraction index $n > 1$ emit electromagnetic radiation if their speed βc_{vac} is larger than the speed of light in the medium, $c_{\text{medium}} = c_{\text{vac}}/n$. This Cherenkov light is the result of a coherent response of a polarizable medium to a perturbation by the passing particle. For a fixed spectral index, Cherenkov photons are emitted under an angle

$$\theta_c = \arccos \frac{1}{\beta n}, \tag{3.16}$$

resulting in the formation of a Cherenkov cone by the Cherenkov photons emitted at a certain time as illustrated in Fig. 3.4. For muons of energy $E > 10$ GeV ($\beta \approx 1$) traversing ice with refractive index $n \approx 1.32$ (at $\lambda = 400$ nm [War84]), the Cherenkov angle is $\theta_c \approx 41°$. The threshold for the emission of Cherenkov light by muons in ice is $E \gtrsim 160$ MeV, defined by $\beta = 1/n$.

The efficiency with which a muon can be detected by its Cherenkov radiation depends on the number of photons emitted per track length in the

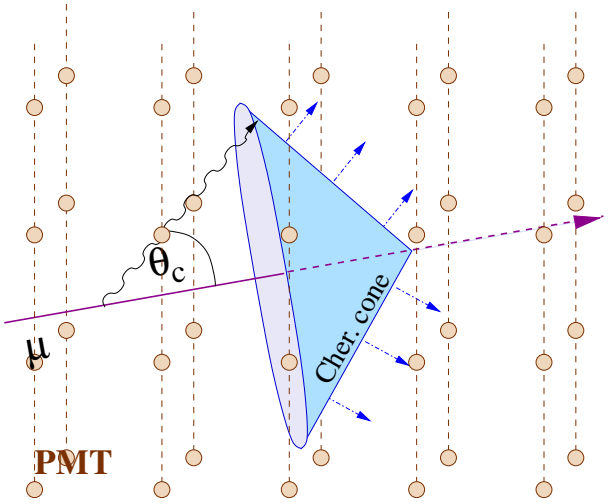

Figure 3.4: Cherenkov radiation emitted by a relativistic muon moving through an optically dense medium. The wave fronts of Cherenkov photons emitted simultaneously with an angle θ_c relative to the muon track form the Cherenkov cone.

sensitive wavelength range $\lambda \gtrsim 330$ nm of the Cherenkov light detectors (photomultipliers)[3], limited by the transparency of the ice to wavelengths $\lambda \lesssim 500$ nm (cf. Fig. 3.6). This number [Jac96]

$$\frac{\mathrm{d}N}{\mathrm{d}x} = 2\pi\alpha \int_{\lambda_{\min}}^{\lambda_{\max}} \lambda^{-2}(1 - \frac{1}{\beta^2 n^2(\lambda)})\mathrm{d}\lambda \tag{3.17}$$

(with $\alpha \approx 1/137$ the fine structure constant) amounts to approximately 260 photons/cm at wavelengths 300-500 nm or an energy loss of

$$\frac{\mathrm{d}E}{\mathrm{d}x} = \int_{\lambda_{\min}}^{\lambda_{\max}} \frac{\mathrm{d}^2 N}{\mathrm{d}x\mathrm{d}\lambda}\frac{hc}{\lambda}\mathrm{d}\lambda \approx 860 \text{ eV/cm} \tag{3.18}$$

in the sensitive energy range. A further contribution to the detectable Cherenkov light originates from secondary particles generated in stochastic energy loss processes.

3.5 The AMANDA detector

Neutrino Cherenkov telescopes (for a review, see [Spi03]) make use of large volumes of transparent media to compensate for the small cross section of neutrino interactions. The necessary detector size allows only the use of natural resources - water in oceans or deep lakes or the Antarctic glacier. The volume is instrumented by optical modules containing photomultiplier tubes (PMTs) for the detection of Cherenkov photons.

Currently, one water Cherenkov telescope is operating in Lake Baikal [B$^+$03a]. Two further detectors in the Mediterranean sea, ANTARES and NESTOR, have operated prototype detectors with a few optical modules. The AMANDA detector (Fig. 3.5) is the first neutrino telescope using ice as detection medium. It was built close to the geographic South Pole in several stages from 1994 to 2000. A first prototype of the detector, AMANDA-A, was built at a depth of less than 1 km, where due to air bubbles in the ice the effective scattering length (see below) is in the order of 1 m. This makes a track reconstruction difficult, so AMANDA-A is not used any longer for data analysis.

The completed AMANDA-II detector as used for this analysis consists of 677 optical modules deployed on vertical strings of 20–42 OMs, connected to the surface by optical and electrical cables. The detector contains 19 strings at a depth from 1500 to 2000 m (three strings extending from 1150 to 2350 m, one string from 1000 to 1530 m) with horizontal nearest neighbor distances

[3]Currently, the use of wavelength shifter (WLS) foils for the optical modules of the future Icecube detector is investigated [RS]. The WLS increases the detection efficiency for Cherenkov light by absorption of photons with low wavelength $\lambda \lesssim 330$ nm and emitting photons at $\lambda \gtrsim 340$ nm.

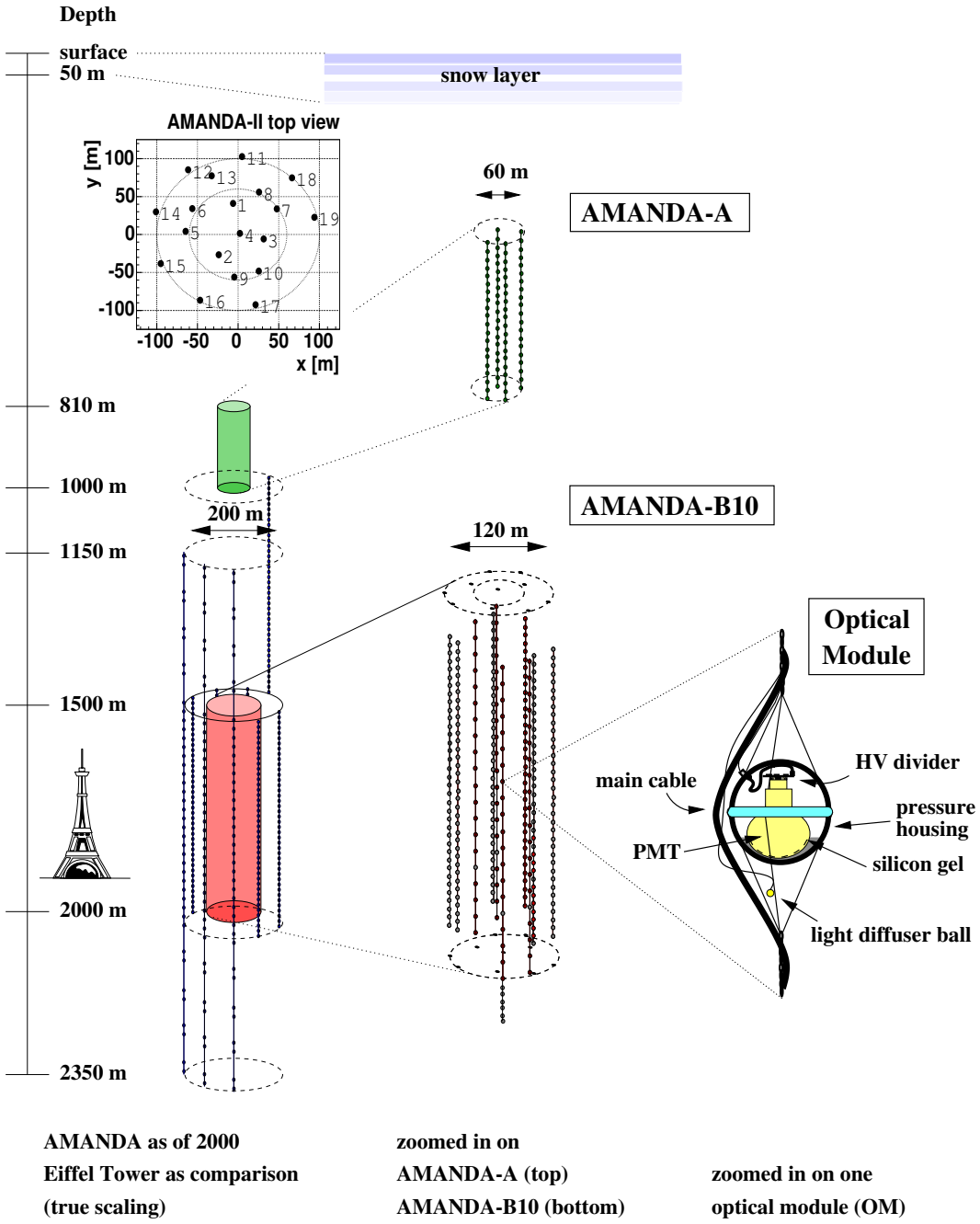

Figure 3.5: Layout of the AMANDA-II detector. 677 optical modules are deployed on 19 strings at a depth between 1150 and 2350 m. For comparison, the extent and position of the earlier stages of the detector, AMANDA-A and AMANDA-B10, are also shown. The top view of the detector shows the circular arrangement of the 19 strings. The origin of the AMANDA coordinate system is at a depth of 1730 m; Zenith angles θ of particle trajectories are defined with respect to the vertical z-axis, i.e. $\theta = 0°$ for a vertically down-going muon. The direction of the x-axis (detector azimuth $\Phi = 0°$) is given by the prime meridian.

of about 30 to 60 m and vertical distances between optical modules of 10 to 20 m. The instrumented volume has an approximately cylindrical shape with a diameter of 200 m, compared to the AMANDA-B10 sub-detector comprising 10 strings with 302 optical modules and a horizontal diameter of 120 m.

Optical modules and readout system

The main component of an optical module is a photomultiplier (8" cathode diameter) amplifying single photoelectron pulses. The PMT is optically coupled to a surrounding glass pressure sphere. Electrical cables[4] for the high voltage supply and the transmission of the measured signal connect the PMT to the readout electronics at the ice surface. Due to dispersion, the pulses read out electrically are broadened to several 100 ns. However, the photon arrival time can still be calculated with a resolution of 4–8 ns from the leading edge time shifted by an amplitude dependent correction (cf. section 6.1.1). The modules of the outer 9 strings are additionally equipped with LEDs converting the PMT pulse into an optical signal, which is transmitted to the surface in fiber optic cables. Small dispersion in the optical fibers leads to narrow pulses of approximately 30 ns width and a timing resolution of about 4 ns for the photon arrival time measurement.

At the surface, the signals are decoupled from the high voltage (in the case of electrical readout) or transformed from optical to electrical pulses. After amplification, the pulses are sent to discriminators with individual thresholds for each module and – via a delay of 2 μs – to a peak sensing Analog-to-Digital-Converter (ADC). The discriminator output is fed into a Time-to-Digital-Converter (TDC), which buffers up to 8 leading and 8 trailing edge times over 32 μs, and into the trigger logic. An independent part of the data acquisition system, installed since beginning of 2003, allows to measure not only the maximum pulse amplitude, but to register the time dependent wave form of each pulse: Transient Waveform Recorders (TWRs) sample the pulses from 597 channels with a timing resolution of 10 ns and increase the dynamic range of the amplitude measurement by two orders of magnitude. Especially the analysis of diffuse extraterrestrial neutrino fluxes, which essentially makes use of reconstructed energies for background suppression, will benefit from the TWR system.

The detector readout is triggered by the coincidence of at least 24 pulses within a time window of 2.5 μs. Alternative trigger conditions are lower hit multiplicities occurring in adjacent OMs in one string ("string trigger"), or an external trigger formed by the SPASE air shower array, located close to the AMANDA experiment. For this analysis, we only use events which fulfill the 24-fold coincidence. Cherenkov light emitted by atmospheric muons

[4] The central four strings are equipped with coaxial cables, the others with twisted pair cables.

penetrating the ice down to the AMANDA detector causes an average trigger rate of 63 Hz.

A TDC stop signal is sent after 10 μs delay with respect to the trigger time, so that the timing information is available from 22 μs before until 10 μs after the trigger signal. The peak-ADC gate is opened at the trigger time, so that for each module the maximum amplitude measured not earlier than 2 μs before the trigger time is recorded.

Optical ice properties

The accuracy of neutrino fluxes measured or constrained with the AMANDA detector depends on the knowledge of the parameters of the ice surrounding the detector. The most important parameters are

- the absorption length λ_a describing the reduction of detectable light with the distance between emitter and receiver and
- the scattering length λ_s and the average cosine of the scattering angle $\langle\cos\theta\rangle$. The effective scattering length $\lambda_s^{\text{eff}} = \frac{\lambda_s}{1-\langle\cos\theta\rangle}$ is a measure of the increase of the path length covered by photons due to scattering, taking into account the strongly anisotropic angular distribution of light scattered in ice. λ_s^{eff} determines the delay of photon arrival times with respect to the case of rectilinear propagation.

The optical properties of the ice surrounding the AMANDA detector have been measured using light sources located in the optical modules and pulses from a YAG-laser operated at the ice surface sent through optical fibers to diffuser balls in the modules. The scattering and absorption coefficients $1/\lambda_s^{\text{eff}}$ and $1/\lambda_a$ obtained by the evaluation of observed attenuation and arrival time delay distributions are shown in Fig. 3.6. At the depth of the AMANDA-II detector the scattering coefficient is relatively low ($\lambda_s^{\text{eff}} \approx 20 - 30$ m) compared to the shallower depth of AMANDA-A, but there are three layers labeled A, B, C in Fig. 3.6 (layer D is located below the main instrumented volume) of enhanced dust concentration and therefore smaller scattering length. The absorption coefficient slowly rises with depth because of increasing ice temperature with depth [WP01]. The wavelength dependence of absorption and scattering length has been measured using laser light of different wavelength ranging from UV (337 nm, emitted by nitrogen lasers) to green light (532 nm, frequency doubled from the YAG laser). It is in agreement with theoretical expectations [HP98].

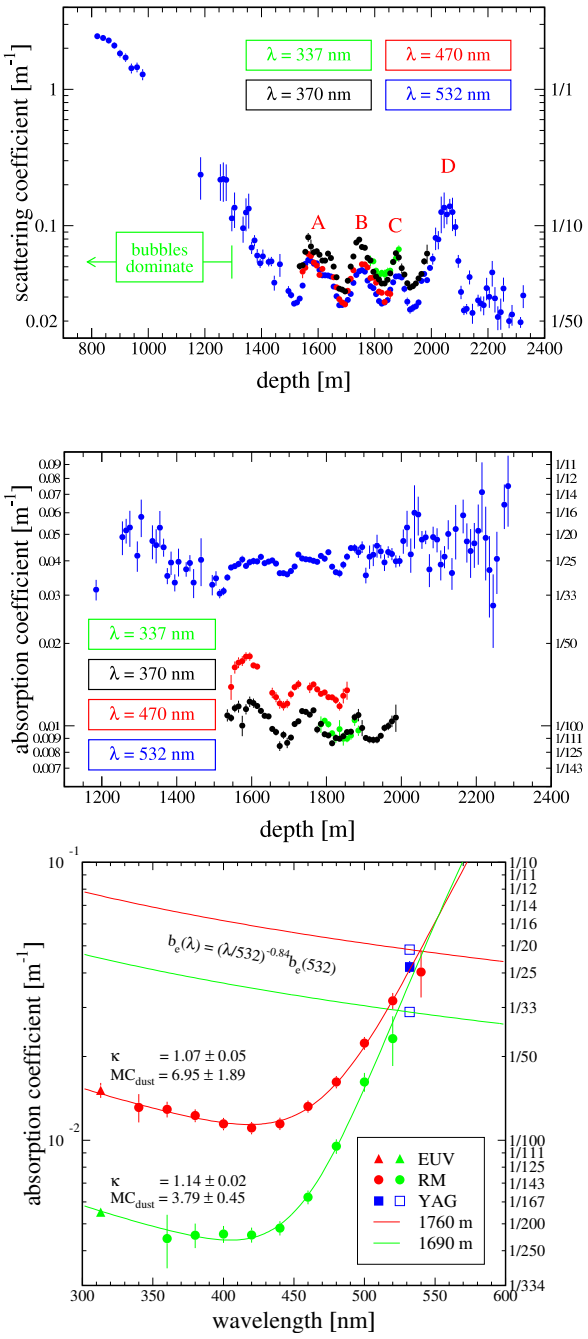

Figure 3.6: Depth dependence of scattering (*top*) and absorption (*middle*) coefficients. The modules of the AMANDA-II detector are located at depths between 1150-2350 m, with most modules between 1500 and 2000 m. This region shows relatively low, but varying scattering coefficients. *Bottom:* Wave length dependence of absorption ($1/\lambda_a$) and scattering coefficients ($b_e = 1/\lambda_s^{\text{eff}}$) at two depths within about 40 m from the center of the AMANDA detector. The curves show expectations from a "three-component-model" [HP98] for the wavelength dependence.

Chapter 4

Event simulation

The simulation of astrophysical neutrino events is essential for the determination of the signal detection efficiency and thereby for the calculation of flux limits or detected fluxes. Simulated atmospheric neutrinos and atmospheric muons serve as a cross check of the understanding of the detector.

This chapter describes the simulation chain starting with the generation of atmospheric neutrinos, neutrinos from astrophysical point sources, and atmospheric muons, and ending with the simulation of the detector response.

4.1 Event generation

4.1.1 Neutrino simulation

For this analysis, two neutrino event generators, NUSIM [Hil96] and ANIS [GK03], have been used. Initially, only NUSIM was available, allowing simulation of an E^{γ} muon neutrino spectrum with different angular distributions (either isotropic or a "point source" flux, i.e. neutrinos from a fixed zenith angle corresponding to a fixed declination, since the AMANDA detector is located at the South Pole). The propagation of the neutrinos through the earth is simulated by random charged and neutral current interactions leading to loss of the neutrino or reduction of its energy. At a distance to the detector of at most two times the approximated muon range (3.14), a charged current interaction is simulated, resulting in a hadronic cascade and a muon. The interaction probabilities are taken into account by assigning a weight to each simulated event.

Recently, the neutrino event generator ANIS was developed [GK03]. It has similar capabilities for muon neutrino simulation, but it correctly simulates the scattering angle between the neutrino and the detectable muon[1]. Addi-

[1]The neutrino induced muons generated with NUSIM have the same direction as the initial neutrino. The angular difference was neglected in AMANDA-B10 point source analyses with bin sizes of $7^{\circ} \times 7^{\circ}$ or larger, but the smaller bin sizes in the current analysis require the correct simulation of scattering angles.

tionally, ANIS can simulate the propagation of ν_e and ν_τ neutrinos through the earth and their final interaction in the detection volume.

Both neutrino generators can be used to simulate atmospheric neutrino spectra or point source signals with different energy spectra by application of appropriate weights.

4.1.2 Atmospheric muon simulation

Muons from cosmic rays interacting with the earth's atmosphere above the detector are the dominant background to any analysis of upward moving neutrinos at trigger level. They are simulated using the CORSIKA program [H$^+$98]. It simulates the generation of air showers by primary hadrons of energies up to 10^{20} eV. The event selection for the point source analysis efficiently rejects atmospheric muon events to a level of less than 10^{-7} of the trigger rate. Therefore, a large number of simulated air showers would be needed at trigger level for a comparison of data and simulation at final level. This number is reduced by 100-fold oversampling of the CORSIKA events, i.e. executing the following steps of the simulation chain for 100 identical events, which differ only by the azimuth angle and a horizontal translation. Due to the small passing rate, at higher cut levels the probability that two events from the same oversampling series survive is small.

Since the background for the point source analysis can be determined from observed data events, the precise simulation of atmospheric muon events is not crucial for this analysis. Nevertheless, a comparison of downgoing data and simulated events at the first cut levels serves as a cross check of the muon propagation and the detector simulation, which are executed for both signal and background simulation in the same way.

4.1.3 Muon propagation

Both atmospheric muons and muons created in neutrino nucleon interactions are propagated to the location of the detector using MMC [RC01]. This program simulates continuous ionization energy losses and stochastic energy losses by pair production, bremsstrahlung and photonuclear interaction. In the case of NUSIM, the muons induced by upward moving neutrinos in the rock below the detector are propagated by another algorithm, PROPMU [LS91], up to the bottom of the ice. Due to adaptable minimal energy losses and updated cross section parameterization, MMC is expected to give more precise results.

In section 6.6.6, we investigate the uncertainty of signal event rates due to different propagation codes.

4.2 Detector simulation

The detector simulation AMASIM [Hun99] consists of two parts: at first, the number of Cherenkov photons and their arrival times at each OM are simulated. Since the propagation of single photons is very time consuming, the presently applied method (program PTD, [Kar99]) makes use of tables containing the photon detection probability as a function of the residual time (between the photon arrival time and the time expected for unscattered light propagation) and of the position and orientation of the OM relative to the muon track. The parameterization tables have to be calculated only once for a given set of ice parameters.

A disadvantage of this method is that depth-dependent changes of the ice parameters are ignored: the parameters at the OM location are assumed to be valid for the whole path between origin and detection of the Cherenkov photons. This leads to imprecise simulation of a certain class of misreconstructed events with the (amplitude weighted) "center of gravity" of the positions of hit OMs being concentrated in three horizontal layers, as investigated e.g. in [Kow04].

For this analysis, we compare two models for the ice properties. One model (named KGM) is based on measurements of absorption and scattering length at fixed wavelengths. It shows an excess of photons with large arrival time delays when comparing the down-going muon simulation to observed data. This is possibly due to the simplified simulation of the photon propagation and has been compensated in the MAM model by a 15% increased absorption coefficient. By default, expected event numbers are obtained from simulation with the MAM ice model; the difference to the KGM model is taken into account in the systematic uncertainties.

The second step in the detector simulation is the translation from the number and time distribution of photoelectrons to the information delivered by the AMANDA data acquisition hardware as in experimental data: for each optical module, the number of photoelectrons and the Cherenkov photons' arrival times are sampled from the pre-calculated tables. Taking into account a time jitter in the PMT, the delay and dispersion in the approximately 2 km long cables or optical fibers, each photoelectron is translated to a pulse form. In the case of multiple photoelectrons, the single pulses are superimposed. The ADC, LE (leading edge), and TOT (time over threshold, i.e. duration) values of the pulse are obtained from the maximum amplitude and the points of time when the simulated pulse form exceeds or under-runs the discriminator threshold (stored individually for each OM).

Chapter 5

Limit calculation and detection probability

In a search for point sources, a signal is detectable as an accumulation of events coming from the same direction within the resolution of the reconstructed coordinates. Based on the average number of background events expected in a search bin and the number of events actually observed in this bin, one can calculate a limit on the possible contribution of signal events (section 5.1), or the probability that the observation is not caused only by a fluctuation of the background event number, i.e. the detection probability (section 5.2). In section 5.3, we discuss the placement of search bins for the point source search in a large fraction of the sky.

5.1 Limits and sensitivities

Once an event sample has been selected for the point source analysis, this sample will be searched for a significant excess of events coming from a certain direction. If no excess is found in the data, we will calculate flux limits which depend on the hypothesis about source location and spectrum.

The ingredients for a limit calculation are:

1. The number of observed events n_{obs}. For a given hypothesis of a source at location[1] (α_s, δ_s) we define a circular search bin $\{(\alpha, \delta) | \Psi((\alpha_s, \delta_s); (\alpha, \delta)) < R\}$, where

$$\Psi((\alpha_s, \delta_s); (\alpha, \delta)) \equiv \arccos(\cos\delta \cos\delta_s \cos(\alpha - \alpha_s) + \sin\delta \sin\delta_s) \quad (5.1)$$

   is the angular distance between the direction given by (α, δ) and the source direction. n_{obs} is the number of events with reconstructed directions (α, δ) in the search bin of radius R of a few degrees.

[1] In this analysis we use equatorial coordinates, declination δ and right ascension α, in the J2000 system.

2. The number n_b of background events (atmospheric neutrinos and misreconstructed atmospheric muons) expected in the search bin. This background is estimated based on the experimental data set alone: we assume that the observed up-going experimental data events mainly originate from atmospheric neutrinos and from misreconstructed atmospheric muons and that contributions from extraterrestrial point sources are small. In the case of the AMANDA detector, located at the geographic latitude 90°, the equatorial coordinates α and δ are calculated from the detector coordinates ϕ and θ by an offset $\alpha - \phi = f(T)$ increasing linearly with the time T at which the event is recorded, and $\delta = \theta - 90°$. Due to the rotation of the earth, variations of the event rates due to an azimuth-dependent detector acceptance are leveled out by the transformation to right ascension. Therefore, the number of background events in a small declination band $\{(\alpha, \delta) | R > |\delta - \delta_s|\}$ around the source is uniformly distributed in the right ascension and can be calculated by scaling the number of events observed in the band with the fraction of the solid angle of the search bin compared to the solid angle of the band (cf. Fig. 5.1):

$$n_b = \langle n_{\mathrm{bin}} \rangle = n_{\mathrm{band}} \cdot \frac{2\pi(1 - \cos R)}{2\pi(\sin(\delta_s + R) - \sin(\delta_s - R))}. \tag{5.2}$$

Close to $\delta = 90°$, the search bin covers a substantial fraction of the declination band. Therefore, we estimate the background density at $\delta > 85°$ from an adjacent declination region, as described in section 8.3.

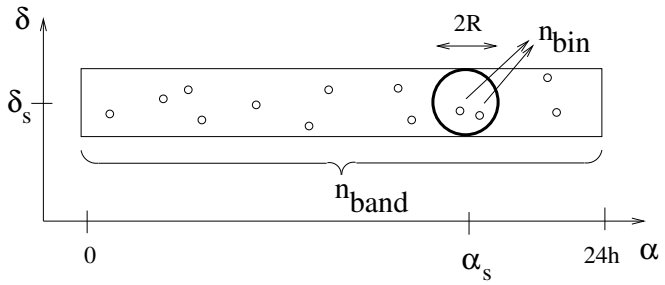

Figure 5.1: Background estimation from a declination band. Assuming that any signal contribution is small compared to the total number n_{band} of events (indicated by small circles) in the declination band, the expected background $\langle n_{\mathrm{bin}} \rangle$ can be obtained by scaling down the total number of events observed in the declination band, n_{band}, with the ratio of the solid angle of the search bin compared to the solid angle of the declination band.

We choose the approach by Feldman and Cousins [FC98] to calculate flux limits at a 90% confidence level. It can be briefly summarized as follows:

The Feldman/Cousins (FC) limit is obtained by calculating intervals ("confidence belts") $I(n_s|n_b) = [n_{\rm obs}^{\rm min}(n_b, n_s), n_{\rm obs}^{\rm max}(n_b, n_s)]$ for different hypothetical signal contributions of n_s events on average, so that the probability that this interval contains the observed number $n_{\rm obs}$ (given a Poissonian distribution with mean $n_b + n_s$) is at least 90% (cf. Fig. 5.2). This does not yet uniquely restrict the interval – the FC construction therefore specifies the order in which the $n_{\rm obs}$ values are to be included in the interval: for each value $n_{\rm obs}$, we calculate the Poissonian probability $P_{n_s+n_b}(n_{\rm obs}) \equiv e^{-n_s-n_b}(n_s+n_b)^{n_{\rm obs}}/n_{\rm obs}!$ to observe $n_{\rm obs}$ events in presence of mean signal and background event numbers n_s and n_b, respectively. We also calculate the number $n_s^{\rm best}$ which maximizes $P_{n_s^{\rm best}+n_b}(n_{\rm obs})$ and include the numbers $n_{\rm obs}$ in the confidence belt in the order of decreasing likelihood ratios $r(n_{\rm obs}) \equiv P_{n_s+n_b}(n_{\rm obs})/P_{n_s^{\rm best}+n_b}(n_{\rm obs})$.

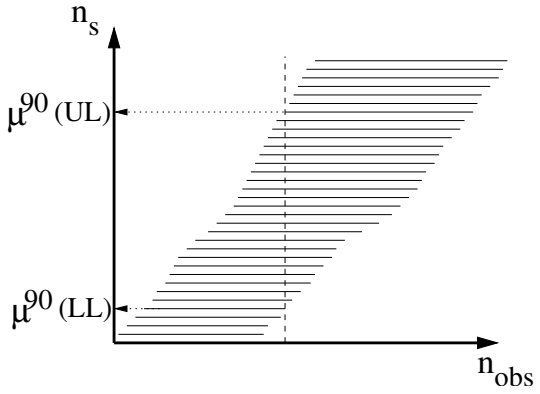

Figure 5.2: Illustration of the limit definition (for a fixed mean number of background events n_b). The horizontal lines indicate confidence belts $I(n_s|n_b)$ for different mean signal numbers n_s, such that the intervals contain a random number of observed events (given the sum of two Poissonian distributions with mean n_b and n_s) with a probability of 90%. For a certain number of observed events $n_{\rm obs}$ (vertical dashed line), the upper and lower limits μ^{90}(UL) and μ^{90}(LL) are given by the maximum and the minimum value of n_s, for which the confidence belt contains $n_{\rm obs}$.

The upper limit $\mu^{90}(n_b, n_{\rm obs})$ on the signal contribution is defined as the largest mean signal number n_s, for which $n_{\rm obs} \in I(n_s = \mu^{90}|n_b)$, and correspondingly the lower limit is the lowest value of n_s which fulfills this condition. A signal contribution of $\hat{n}_s > \mu^{90}(n_b, n_{\rm obs})$ to the events observed in the search bin is excluded at 90% confidence level in the following sense: In a series of identical experiments a fraction of at least 90% of the experiments would result in μ^{90} numbers which are larger than the true signal contribution $\hat{n}_s$.

Under the hypothesis of no signal contribution, repeating the same experiment or looking at independent search bins with constant mean background yields varying observed event numbers $n_{\rm obs}$ with Poissonian probabilities

$P_{n_b}(n_{\mathrm{obs}})$. Averaging the upper limit μ^{90} on the number of signal events leads to the sensitivity, defined as the expectation value of the limit in absence of any signal:

$$\langle \mu^{90}(n_b) \rangle = \sum_{n_{\mathrm{obs}}=0}^{\infty} P_{n_b}(n_{\mathrm{obs}}) \mu^{90}(n_b, n_{\mathrm{obs}}). \tag{5.3}$$

This sensitivity depends only on the expected mean background but not on the number of observed events in individual bins. The sensitivity is therefore suitable for cut optimization – choosing the cuts which lead to the best sensitivity results in the best average limits, without biasing the selection due to fluctuations in the observed data.

$\mu^{90}(n_b, n_{\mathrm{obs}})$ and $\langle \mu^{90}(n_b) \rangle$ limit the number of signal events contributing to the number of observed events in the search bin, independently of an assumption about the source energy spectrum. From that, we can derive a flux limit or sensitivity for any given spectrum $\mathrm{d}\Phi_{\mathrm{model}}/\mathrm{d}E$: if the contribution of the assumed flux to the number of observed events in the source bin is n_{sig} (determined from Monte Carlo simulation), the model flux has to be scaled by $\mu^{90}(n_b, n_{\mathrm{obs}})/n_{\mathrm{sig}}$ to be excluded at 90% confidence level. The flux limit and sensitivity at 90% confidence level therefore are:

$$\frac{\mathrm{d}\Phi^{\mathrm{limit}}}{\mathrm{d}E} = \frac{\mu^{90}(n_b, n_{\mathrm{obs}})}{n_{\mathrm{sig}}} \frac{\mathrm{d}\Phi_{\mathrm{model}}}{\mathrm{d}E}, \tag{5.4}$$

$$\frac{\mathrm{d}\Phi^{\mathrm{sens}}}{\mathrm{d}E} = \frac{\langle \mu^{90}(n_b) \rangle}{n_{\mathrm{sig}}} \frac{\mathrm{d}\Phi_{\mathrm{model}}}{\mathrm{d}E}. \tag{5.5}$$

5.1.1 Limits in the presence of systematic uncertainties

In the presence of systematic (or statistical) uncertainties, the assumed signal detection efficiency and the estimated mean number of background events deviate from the true numbers.

Assuming that signal and background numbers can deviate from the nominal values n_{sig} and n_b by at most $\pm\sigma_s n_{\mathrm{sig}}$ and $\pm\sigma_b n_b$, conservative limits can be calculated by replacing $n_b \to n_b \cdot (1 + \sigma_b)$ and $n_{\mathrm{sig}} \to n_{\mathrm{sig}} \cdot (1 - \sigma_s)$. However, the confidence level of the limit derived in this way is $CL = 90\%$ only in the most extreme case of maximally reduced signal and increased background with respect to the expectation. In general, the limit will have a confidence level $CL > 90\%$ (over-coverage). Since the deviations are not known precisely, but only their maximum possible values $\sigma_{s,b}$ can be estimated, the AMANDA collaboration agreed to use a semi-Bayesian approach [C$^+$03b, Hil03], which is a modification of the FC limit calculation in absence of uncertainties: we introduce a signal efficiency ϵ, following a Gaussian distribution with mean $\langle \epsilon \rangle = 1$ and standard deviation σ_s. Also the mean

number of background events is varied, according to a Gaussian distribution[2] with mean n_b and standard deviation $\sigma_b n_b$. For the construction of the confidence belts, we replace the Poissonian probabilities $P_{n_s+n_b}(n_{\rm obs})$ by $\int_0^\infty \int_0^\infty P_{\epsilon n_s+b}(n_{\rm obs}) p_s(\epsilon) p_b(b) {\rm d}b{\rm d}\epsilon$, where p_s and p_b are the probability density functions of the signal efficiency and the background number. The upper limit derived with this modification is effectively an average of the limits which would be obtained in similar experiments with signal efficiencies and background numbers varying within the assumed uncertainties.

Following the way of calculating flux limits described in section 5.1, only the signal expectation can be influenced by systematic uncertainties, due to uncertainties in the calculation of $n_{\rm sig}$ by Monte Carlo simulation. The number of expected background events is based on observed data and is therefore only subject to statistical fluctuations.

We investigate the contributions to uncertainties of signal and background event numbers in section 6.6. Typical values of the mean background number $n_b = 1.5$, the signal uncertainty $\sigma_s = 33\%$, and the background uncertainty $\sigma_b = 15\%$ lead to a deterioration of the upper limits by about 13% (if $n_{\rm obs} = 1$) to 34% (if $n_{\rm obs} = 6$) compared to limits calculated according to the original FC method (not considering uncertainties). Detailed numbers for the investigated sources are included in Tab. 8.1 based on the uncertainties described in section 6.6.

5.2 Detection probabilities

While improving the sensitivity means reducing the maximum possible signal event number which is consistent with the observation, we are also interested in optimizing the probability for the detection of a source of high energy neutrinos, assuming the existence of a source with a sufficiently high flux.

The detection probability depends on the assumed signal strength, the background expectation, and the required "confidence level" of the detection. The latter can be quantified by the significance n_σ. An observation is said to have a significance of n_σ sigma, if the chance probability that this observation occurred as a fluctuation of background events is

$$P = \frac{1}{\sqrt{2\pi}} \int_{n_\sigma}^{\infty} e^{-x^2/2} {\rm d}x \tag{5.6}$$

$$\equiv \frac{1}{2} - \frac{1}{2} {\rm erf}(\frac{n_\sigma}{\sqrt{2}}). \tag{5.7}$$

(This is the probability to observe a value $x > n_\sigma \sigma + \mu$ for a Gaussian distribution with standard deviation σ and mean μ.)

[2] To be precise, ϵ and n_b are restricted to positive values. In the cases relevant for this analysis, the effect of the truncation is negligible.

An optimization for maximum detection probability would depend on the assumption about the signal strength and on the desired significance. Instead, a uniquely defined event sample, obtained by cuts optimized for best average upper limits, is used both for limit calculation and for the search for a significant excess. Since both sensitivity and detection probability improve with lower remaining background B and higher remaining signal number S approximately as $S/\sqrt{B}$, the optimization of the sensitivity will also result in relatively large detection probabilities.

5.3 Binned point source searches

In this section, we consider a set of events with reconstructed Cartesian coordinates (x_i, y_i) and unknown true coordinates $(x_i^0, y_i^0) \equiv (x_i, y_i) - (\Delta x_i, \Delta y_i)$. This is a simplification to the real subject of this thesis, the search for point sources of neutrinos from the Northern hemisphere which is described by equatorial coordinates (α, δ). However, any small part of the sky can be approximately parameterized by Cartesian coordinates, so these investigations are useful for non-Cartesian coordinates as well.

The aim of a binned search is the detection of a contribution from an assumed source at unknown position (x_s, y_s) and unknown strength n_s. If the reconstruction of x and y coordinates has a resolution σ_Ψ, i.e. if the reconstruction errors $\Psi_i = \sqrt{\Delta x_i^2 + \Delta y_i^2}$ are distributed according to

$$\frac{\mathrm{d}N}{\mathrm{d}\Psi} \propto \Psi \cdot e^{-\frac{\Psi^2}{2\sigma_\Psi^2}}, \tag{5.8}$$

a simple method is to divide the search region into square bins with a side length $2R = 2.8\sigma_\Psi$, which optimizes the detection significance for a source located in the center of any of the bins [Bir02]. However, since the source position is unknown, the possibility must be taken into account that a source can be located anywhere in the search bin. This reduces the average signal contribution and leads to a decreased average significance, which is usually overcome by quadrupling the number of search bins as indicated in Fig. 5.3 for circular search bins.

In this case, for each possible source there is one search bin for which the differences in x and y between source position and bin center are less than 1/4 of the bin width. The minimum distance of the source to the closest bin center is further decreased if the search grid is shifted $N_{\mathrm{shift}} > 2$ times by $\frac{2R}{N_{\mathrm{shift}}}$ in both x and y directions. However, with a larger number of shifts also the probability to observe a background fluctuation inside one bin increases.

A quantitative evaluation of the detection probabilities is possible with a simple simulation, based on typical bin size and event numbers of the AMANDA point source search: we define a grid of 10×10 bins of side length 7.2 ($R = 3.6^\circ$ is a typical bin size as optimized for the point source analysis).

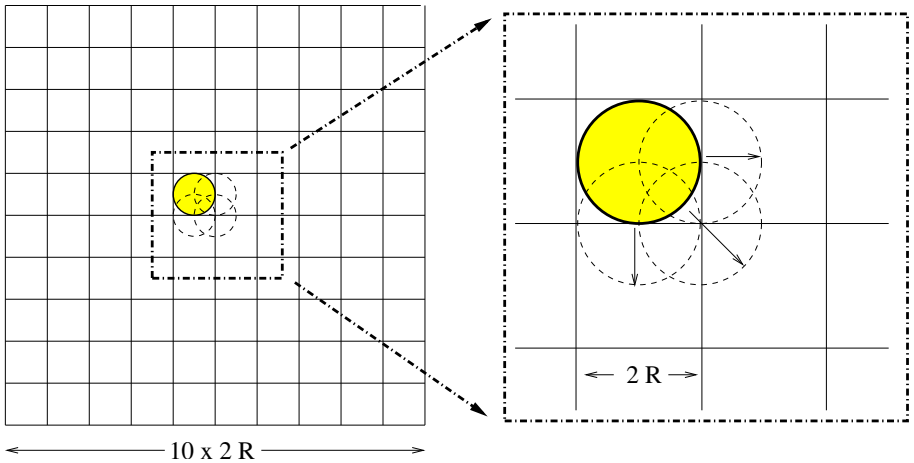

Figure 5.3: Geometry of the search bin placement. An array of 10×10 circular bins is used for evaluating detection probabilities. By shifting each bin $N_{\rm shift}$ times in x and y direction, we obtain $N_{\rm shift}^2$ overlapping sets of search bins. The shifted positions of the shaded bin are shown for $N_{\rm shift} = 2$.

$N_{\rm shift}^2 \times 100$ circular bins are placed in the grid ($N_{\rm shift} = 1, 2, ..., 8$). A mean background of 1.6 events per circular bin is simulated in this grid. We add a source, contributing a mean number of $\langle n_{\rm sig} \rangle$ events ($\langle n_{\rm sig} \rangle$ running from 0 to 10 in different simulations), with a resolution $\sigma_\Psi = 2.1$ at a random position in one of the four central grid squares.

Using 10^5 simulated event sets, we evaluate the probability for a detection with an overall significance of n_σ sigma in the following way: The relative occurrences of the maximum number $\hat{n}_{\rm obs}$ of events observed in any of the overlapping bins define the distributions $P_{\rm bg}(\hat{n}_{\rm obs})$ (if no signal is added) and $P_{\rm sig}(\hat{n}_{\rm obs})$ (depending on $\langle n_{\rm sig} \rangle$). For each simulated event set, $\hat{n}_{\rm obs}$ determines the n_σ significance of a "source detection" at the point where this number occurs: according to (5.6), the significance $n_\sigma(\hat{n}_{\rm obs})$ is given by:

$$\mathrm{erf}(n_\sigma(\hat{n}_{\rm obs})/\sqrt{2}) = 1 - 2 \sum_{k=\hat{n}_{\rm obs}}^{\infty} P_{\rm bg}(k), \tag{5.9}$$

where $\sum_{k=\hat{n}_{\rm obs}}^{\infty} P_{\rm bg}(k)$ is the probability that $\hat{n}_{\rm obs}$ occurs in absence of a signal. Counting the number of simulations with at least the minimum number $n_{\rm obs}(n_\sigma)$ of events observed in any search bin, which is necessary for an n_σ significance, yields the detection probability:

$$P_{\rm detect}(n_\sigma) = \sum_{\hat{n}_{\rm obs}=n_{\rm obs}(n_\sigma)}^{\infty} P_{\rm sig}(\hat{n}_{\rm obs}). \tag{5.10}$$

This probability is shown in Fig. 5.4 for two different signal strengths

$\langle n_{\mathrm{sig}} \rangle = 3$ and 7. For the larger signal, it can clearly be seen that for $N_{\mathrm{shift}} \geq 2$ a considerable improvement ($P_{\mathrm{detect}}(n_\sigma = 3) \approx 15\%$) compared to only one non-overlapping system of bins ($P_{\mathrm{detect}}(n_\sigma = 3) \approx 5\%$) is achieved. The smaller signal does not allow observation of a signal of sufficient significance (e.g. $n_\sigma \geq 3$) with a reasonable probability.

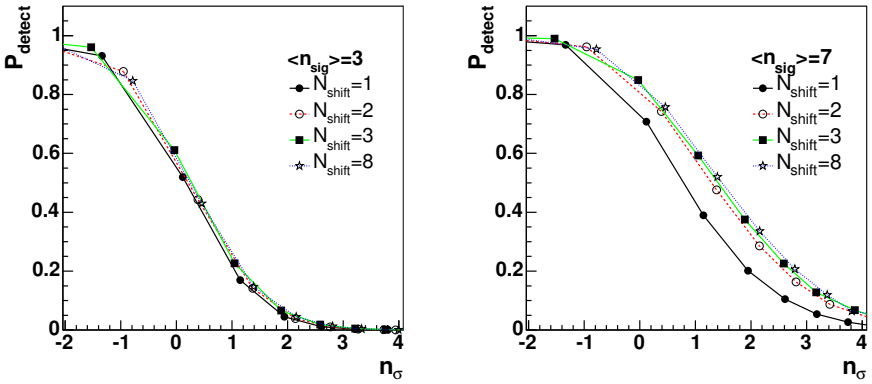

Figure 5.4: Detection probability as a function of the required significance for two different signal strengths (left: $\langle n_{\mathrm{sig}} \rangle = 3$, right: $\langle n_{\mathrm{sig}} \rangle = 7$) and varying number of bin shifts from $N_{\mathrm{shift}} = 1$ (no overlap) to $N_{\mathrm{shift}} = 8$.

Of course, the precise shape of these curves depends on many parameters like the declination dependence of the background density and the resolution σ_Ψ, the total number of bins (search area), and non-Gaussian contributions to the reconstruction error, but the qualitative behavior is independent of these parameters:

Already with $N_{\mathrm{shift}} = 2$ bin shifts in both dimensions, the optimum is almost reached. A larger number of bin shifts does not decrease the reachable significance, as one might expect due to the enlarged probability that events from a positive background fluctuation are contained in one bin. This conclusion motivates the method of the binned search presented in section 8.3: we cover the Northern hemisphere $\{(\alpha, \delta) | \delta > 0\}$ with strongly overlapping circular bins with declination dependent radii $R = 2.6°...4.6°$ and $1°$ distance between the bin centers corresponding to $N_{\mathrm{shift}} \approx 5...9$. This allows us to use the same grid of bins in a binned search and for the calculation of a "flux limit map", i.e. of flux limits as a quasi-continuous function of (α, δ).

Un-binned point source search

Recently, an alternative method to search for point sources in a sample of events with reconstructed coordinates $(x_i, y_i),\ i = 1...N$, has been developed [Neu03]. This method avoids the loss of signal efficiency caused by the finite bin size: assuming a source at position x_s, y_s contributing $n_s = s \cdot N$ events to the sample and a background probability density $\mathrm{bg}(x, y)$, the probability density function for the observation of an event at the position (x, y) is

$$f(x, y|s, x_s, y_s, \sigma) = s \cdot \mathrm{sg}(x_i, y_i|x_s, y_s, \sigma) + (1 - s) \cdot \mathrm{bg}(x_i, y_i) \qquad (5.11)$$

where $\mathrm{sg}(x_i, y_i|x_s, y_s, \sigma)$ is the Gaussian probability density function of signal events (assuming a resolution σ of the reconstructed coordinates), and $\mathrm{bg}(x_i, y_i)$ describes the background distribution. If the resolution σ_i is known or can be estimated for each single event, the maximization of

$$\mathcal{L}(s, x_s, y_s) \equiv \prod_{i=1}^{N} f(x_i, y_i|s, x_s, y_s, \sigma_i) \qquad (5.12)$$

results in estimators of the signal contribution s and source position (x_s, y_s).

Details about the estimation of reconstruction uncertainties σ_i for single events and a comparison of flux limit calculations and detection probabilities between the binned and the un-binned point source search can be found in [Neu03]. Sensitivities and detection probabilities obtained with the two different methods, based on the same event selection optimized for the un-binned search, are similar. In this work, we will only deal with the binned search.

Chapter 6

Event reconstruction and selection

The first task for the search for point sources of high energy neutrinos is the selection of well reconstructed events with a small angular mismatch compared to their true directions. Downward moving muons which are reconstructed as upward moving are to be rejected. After cuts on the directional information from a fast reconstruction method and a subsequent likelihood reconstruction, this separation is achieved by defining an event quality based on a neural network. Except for the directional information, the harder energy spectrum of extraterrestrial neutrinos (i.e. the larger relative contribution of high energy events) compared to atmospheric neutrinos can be utilized for the separation: the neural network has been trained with an E^{-2} signal spectrum; additionally, we investigate the effect of a cut on the number of hit optical modules, which is related to the energy of the neutrino induced muon.

All results presented in this chapter are obtained independently from the right ascension distribution of the observed events. Only the dependence of the acceptance on the zenith angle, which leads to varying cuts as a function of declination, plays a role for the optimization. This guarantees the "blindness" of this procedure to any accumulations in the (α, δ) distribution of the observed data events.

6.1 Low level reconstruction

In the following sections, we describe the preparation of the raw data for the reconstruction as well as the first reconstruction step. The data have been taken in the year 2000 from February 13th until November 4th (days 44-309), within a total measuring time of 248.2 days. The available lifetime after the removal of bad files and after the correction for detector deadtime (17%) is $T_{\text{life}} = 197.0$ d.

6.1.1 Preprocessing

Hit selection

The first step of the data selection for the point source analysis is the definition of a stable subset of the data taking time intervals as well as a stable sub-detector, i.e. a set of optical modules which do not show considerable fluctuations in the noise rate [Rib02].

This selection was performed in three steps:

1. We define the TDC noise level R_{TDC} as the number of TDC leading edges recorded per second in the first 15 μs of the 32 μs event time window. Channels with an average noise level of $R_{\mathrm{TDC}} < 0.1$ (*dead* channel) or $R_{\mathrm{TDC}} > 10$ (*noisy* channel) are rejected. A value of $R_{\mathrm{TDC}} = 10$ would be measured for a module with a noise rate of 8 kHz compared to typical noise rates of 500 to 1500 Hz.

2. Since a group of OMs having simultaneously increased noise rates was observed to influence other parts of the DAQ electronics as well, files with more than 50 additional, temporarily *noisy* OMs are rejected. Such a group of noisy OMs would contribute on average one noise hit in the trigger window of 2.5 μs and thereby effectively lower the trigger threshold from a multiplicity of 24 hits within 2.5 μs to 23.

3. OMs which were *noisy* in more than 3% or *dead* in at least 50% of the remaining files are rejected.

The first criterion defines a list of 115 OMs rejected in the whole data set of the year 2000. 95 out of these OMs are permanently *dead* in the year 2000, so they cannot contribute to the timing information, which is necessary for an event reconstruction. Only one OM (#18) is permanently noisy, 12 OMs temporarily show large noise rates. About 3% of the available lifetime is rejected by the requirement of at most 50 additional *noisy* OMs per file. The third criterion is not handled strictly, but used as a guideline to define three stable periods of the detector, each of which is characterized by a constant set of OMs used for the data analysis. The best description of the detector would be obtained if the OM behavior would be determined on the time scale of single files (with a duration of about 10 minutes) or even shorter. However, in view of the detector simulation a small number of detector configurations is aimed for. Good agreement between experimental data and the simulation is obtained with three OM configurations listed in Tab. 6.1.

After the rejection of noisy, dead, or unstable OMs, a further hit selection is performed in order to reject pulses originating from other sources than down-going muon tracks or high energy neutrino interactions, e.g. noise hits or hits from cross talk between adjacent cables in the ice or in the surface

Days	44-125	126-224	245-309
Number of rejected OMs	130	125	151

Table 6.1: Number of rejected OMs in three data taking periods. Most of the OMs are rejected due to low rate indicating that they are "dead". Days are counted from Jan 1st, 2000. In the following two years, the number of modules rejected due to high, low or unstable noise rates were reduced to 92 by switching from optical to electrical readout, or by adjusting the high voltage, the disciminator thresholds, or the amplification of single channels.

electronics. Cross talk hits can be identified by small pulse durations (time over threshold, TOT) compared to the usual widths of a few 100 ns for electrically transmitted pulses. Hits with TOT values considerably lower than the typical pulse durations are rejected from the further analysis:

$$\begin{aligned} &\mathrm{TOT} < 75\,\mathrm{ns} \quad \text{(electrically readout channels)} \\ &\mathrm{TOT} < 5\,\mathrm{ns} \quad \text{(optically readout channels)} \end{aligned}$$

The TOT distributions are shown in Fig. 6.1. The effect of this hit cleaning has been evaluated for the different OM configurations. From all hits with a valid TDC measurement, about 9% of the hits in electrically readout channels are rejected due to TOT$<$ 75 ns. 1.6% of the hits in the optically readout channels have short pulses TOT$<$ 5 ns. The fraction of rejected hits does not differ significantly between the periods with different OM configurations.

Cross talk hits are not included in the detector simulation, and the time dependent noise rates of rejected OMs are not precisely simulated. This

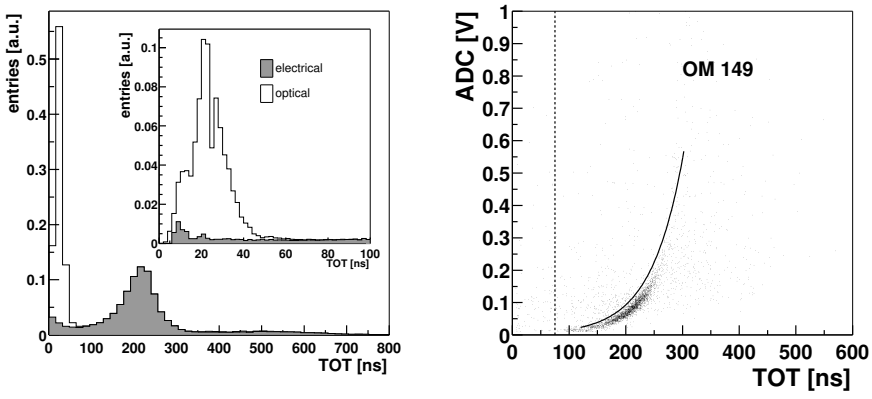

Figure 6.1: *Left:* TOT distributions of electrically and optically readout channels. The inset shows the range of TOTs for optical channels in more detail. *Right:* Principle of the cross talk filter. The dashed line indicates the cut at 75 ns for electrical channels. The dedicated cross talk filter removes hits to the left/top of the solid curve.

leads to a disagreement in the event rates between data and simulation which can be corrected by applying a software trigger condition after the hit cleaning: only events which still fulfill the condition of having 24 hits within 2.5 μs are accepted for the further analysis.

A more sophisticated cross talk cleaning is applied at a later stage of the analysis. This method does not only utilize the duration (TOT) of the recorded pulses, but also the ADC/TOT correlation and special knowledge about pairs of optical modules with a large contribution of cross talk hits [Tab02]. The distribution of amplitude vs. duration for one OM is shown in Fig. 6.1. Pulses with a low TOT/ADC ratio were identified as cross talk pulses in a dedicated measurement with high voltage of the measured photomultipliers switched off, implying that all observed pulses in this OM are due to cross talk or noise. Curves as shown in the figure, which approximately separate real hits from cross talk pulses, have been parameterized for all channels in strings 5–10. Cross talk occurs mainly in these strings because of transmission in twisted pair cables. Since these parameterizations became available only after the low level processing was finished, this filter has been applied afterwards, and the likelihood reconstructions have been repeated with the reduced set of hits. We will finally use these repeated reconstructions to determine the track direction and the event quality, while the outcome of the reconstructions before the application of the cross talk cleaning has been used for the low level filtering up to "level 2", as described below.

After the calibration (cf. following section), we apply a further rejection of hits: only hits with an event time 2 μs before until 4.5 μs after the trigger time are kept for the reconstruction. We also reject hits with a calibrated amplitude below 0.1 photoelectrons. The applied reconstructions are not dependent on a precise amplitude information; however, low amplitude hits are most likely due to noise and would only deteriorate the reconstruction results.

Calibration

The next step in the analysis chain is amplitude, time, and geometry calibration of the recorded hits. The amplitude calibration linearly converts the measured ADC voltage to an approximate number N_{pe} of detected photoelectrons:

$$N_{\mathrm{pe}} = ADC/ADC_{\mathrm{1pe}}, \tag{6.1}$$

where the ADC_{1pe} values (corresponding to the mean amplitude of single-photoelectron pulses) have been fitted for each channel using downgoing muon data. The time calibration corrects for the run time in electrical cables or optical fibers as well as for the amplitude dependent time after

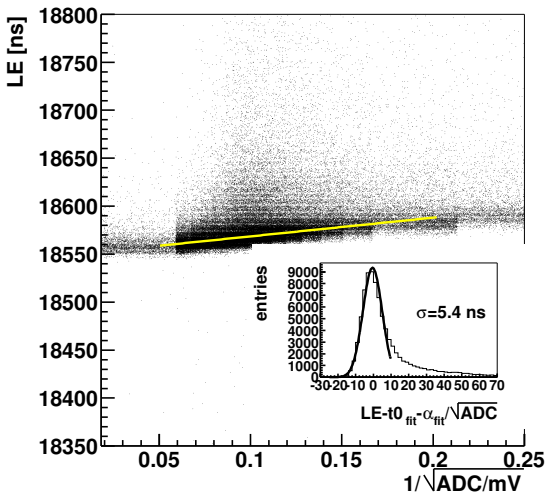

Figure 6.2: Derivation of the timing calibration constants for one optical module. The leading edge time LE of a pulse is approximately linearly dependent on the pulse amplitude ADC, as indicated by the fitted white line. The inset shows the distribution of the residuals $LE - t_{0,\mathrm{fit}} - \alpha_{\mathrm{fit}}/\sqrt{ADC}$ with the offset $t_{0,\mathrm{fit}}$ and slope α_{fit} determined by the fit. α_{fit} is identical to the slope α in (6.2), while $t_{0,\mathrm{fit}}$ still has to be corrected for the propagation time of the laser pulse through the optical fiber and through the ice. The width of this distribution ranges between 4 and 8 ns for different OMs. A tail towards positive residuals is caused by photons scattered between emitting and receiving OM.

which the pulse reaches the discriminator threshold:

$$t = LE - t_0 - \alpha/\sqrt{ADC} \tag{6.2}$$

The parameters t_0 and α are measured in special calibration runs: for each channel, laser pulses are transmitted in optical fibers to a diffuser ball in a near-by OM. The arrival time of the photons at the OM to be measured can be calculated using the known time when the laser pulse is fed into the fiber at the surface, the known run time of the laser pulse down to the diffuser ball and the time needed for the light propagation from the diffuser ball to the measured OM. Due to photon scattering in the ice, this propagation time is a lower bound for the observed propagation times, so that the parameters t_0 and α can be obtained from a fit to the LE vs. $1/\sqrt{ADC}$ distributions, as demonstrated in Fig. 6.2.

The timing calibration constants have been cross checked using downgoing muon data. This method makes use of well reconstructed muon tracks which allow detection and correction of wrong timing constants. This happens, for

example, in modules in which the light is not emitted from the diffuser ball but, due to a bad connection, at the entrance of the optical fiber into the glass sphere. The accuracy of the time calibration with down-going muons is ±8 ns [CH01].

The assignment of spatial coordinates to the optical modules is based on two different measurements. Rough information is available from the deployment of the AMANDA modules when the position of the 19 strings at the surface was measured and from pressure measurements and logging information during the process of drilling. An accuracy of about 1 m in x and y direction and 2 m in z direction can be reached using these data [Wos00]. The relative locations of the optical modules have also been measured by evaluating the time differences between the emission and the detection of light pulses in different optical modules [Wos99] and by an analysis of down-going atmospheric muons [C$^+$03a] with a precision of 1 m.

6.1.2 Fast reconstruction

With $\mathcal{O}(100)$ events per second triggering the detector, a full likelihood reconstruction of each event is not feasible. Therefore, a "first guess" reconstruction is applied as a first filtering step to distinguish clearly downward moving tracks from an expected signal of upward moving neutrinos. The vertex and the direction of this fast reconstruction are used as a seed for the following likelihood reconstruction.

A muon traveling through the AMANDA detector produces Cherenkov photons which reach the photomultipliers after possibly being scattered in the ice. The "direct walk" reconstruction [Ste02] is based on the assumption that close to a muon track there is a significant contribution of "direct" hits with small time residuals (compared to the arrival time if no scattering takes place). Pairs of hits $(\mathbf{r_1}, t_1; \mathbf{r_2}, t_2)_i$ which are separated by $D \equiv |\mathbf{r_1} - \mathbf{r_2}| > 50\,\mathrm{m}$ and with a time difference $\Delta t \equiv |t_1 - t_2|$,

$$\frac{D}{c_{ice}} - 30\,\mathrm{ns} < \Delta t < \frac{D}{c_{ice}} + 30\,\mathrm{ns} \tag{6.3}$$

are selected as track candidates (with the unit direction $\mathbf{u_i} \propto \mathbf{r_2} - \mathbf{r_1}$ and vertex coordinates defined by the two hits). Each of these candidates is assigned a quality Q_i based on the number and distribution of hits in a restricted range of the time residual and of the distance around the track. For the track hypothesis, all candidates with a quality $Q_i > 0.7 \max\{Q_i\}$ are searched for a cluster in direction: for each selected candidate i, we count the number of candidates j with $\angle(\mathbf{u_i}, \mathbf{u_j}) < 15°$. The averaged unit direction of the candidates in the cone with the largest number of close-by candidates determines the direction of the "direct walk" reconstruction.

A cut on the zenith angle of this reconstruction,

$$\theta_{\mathrm{DW}} > 70°, \tag{6.4}$$

reduces the experimental data set to 3% while keeping 91% of simulated upward moving neutrino events following an E^{-2} spectrum with $\frac{\mathrm{d}N}{\mathrm{d}\cos\theta} =$ const in the range $\theta > 90°$. 94% of simulated upward moving atmospheric neutrinos pass this cut. The slightly lower passing rate of events from the harder E^{-2} spectrum is due to the fact that with the muon energy the probability increases that a muon, crossing the detector close to its border or even passing by outside the instrumented volume, triggers the detector. However, these events are difficult to reconstruct, since especially muons not crossing the instrumented volume contribute mainly hits from scattered photons. If the event sample is restricted to neutrino induced muons with a closest distance to the detector center of less than 100 m, the passing rate is 95% irrespective of the neutrino energy spectrum (atmospheric or E^{-2}).

6.2 Likelihood reconstruction

More precise reconstruction results are expected if not only hits with a small distance to the assumed muon track are used, but if a maximum likelihood reconstruction evaluating the full event information is performed.

This reconstruction consists in the minimization of a likelihood[1] function

$$\mathcal{L}(\mathbf{r}, t, \theta, \phi) = -\sum_{i=1}^{N_{\mathrm{hit}}} \log(P(\mathbf{r_i}, t_i|\mathbf{r}, t, \theta, \phi)) \tag{6.5}$$

in a 5-dimensional parameter space. $e^{-\mathcal{L}}$ is the product of the individual probability density functions $P(\mathbf{r_i}, t_i|\mathbf{r}, t, \theta, \phi)$ to observe a photon emitted from a muon track defined by vertex coordinates and direction $\mathbf{r}, t, \theta, \phi$ at an optical module at position $\mathbf{r_i}$ and time t_i.

The likelihood value at the minimum found by the reconstruction serves as a cut variable. To make this cut less dependent on the number N_{hit} of recorded hits, the reduced likelihood is used:

$$\mathcal{L}^{\mathrm{red}} \equiv \frac{\mathcal{L}}{N_{\mathrm{hit}} - 5}. \tag{6.6}$$

Pandel reconstruction: For homogeneous ice with constant scattering and absorption length, the individual hit probabilities can be calculated analytically [Pan96] and depend on the distance ρ from the track, the time residual $\Delta t = t_i - t_{\mathrm{exp}}$ between measured time t_i of the photon detection and the time t_{exp} at which the photon would arrive at the optical module if no scattering took place, and on two free parameters τ and λ (and a normalization factor n):

$$P(\Delta t, \rho) = n \cdot \frac{\tau^{-\rho/\lambda} \Delta t^{\rho/\lambda - 1}}{\Gamma(\rho/\lambda)} e^{-\Delta t/\tau - c_{ice}\Delta t/\lambda_a - \rho/\lambda_a}. \tag{6.7}$$

[1] To be precise, the function to be minimized is the negative logarithm of the likelihood. However, the use of $\mathcal{L}$ is more convenient than $e^{-\mathcal{L}}$, and we refer to $\mathcal{L}$ as "likelihood function".

The parameters $\tau = 557$ ns and $\lambda = 33$ m were obtained by a fit [Wie99] to the photon arrival times simulated with PTD (cf. section 4.2). In practice, we use an approximated convolution of this function with a Gaussian distribution of Δt to account for the finite timing resolution of the optical module. This likelihood reconstruction is denoted as (patched) "Pandel" reconstruction.

We execute a corresponding likelihood reconstruction under the hypothesis of a cascade-like event [Kow04] originating from a hadronic or electromagnetic shower using a probability density function describing the approximately spherical light emission of these events. Since a good angular resolution which is necessary for a point source search can only be achieved for events with a well reconstructed muon track, we will reject cascade-like events by a cut on the difference $\mathcal{L}^{\mathrm{red}}_{\mathrm{track}} - \mathcal{L}^{\mathrm{red}}_{\mathrm{casc}}$ of reduced likelihoods under the hypotheses of either a muon track or a cascade.

MPE reconstruction: Inserting (6.7) into (6.5) does not lead to the correct likelihood if consecutive hits cannot be resolved. This was especially important in the case of events recorded with the AMANDA-B10 sub-detector in which all channels are read out via electrical cables with a pulse width of a few 100 ns. To treat pulses from multiple hits correctly, the number N of photons contributing to the pulse is estimated from the amplitude, and (6.7) is replaced by the probability density function for the first photon out of N to be observed with a time residual Δt at a distance ρ from the track:

$$P_N^{\mathrm{1st}}(\Delta t, \rho) = N \cdot P(\Delta t, \rho) \cdot \left(\int_{\Delta t}^{\infty} P(\Delta t, \rho) \mathrm{d}t \right)^{N-1}. \tag{6.8}$$

In the AMANDA-II detector with most channels in strings 11–19 read out via optical fibers, this multi-photoelectron (MPE) reconstruction does not improve the angular resolution. However, the comparison between standard and MPE reconstruction serves as a criterion for the reconstruction quality.

Zenith weighted reconstruction: By default, the whole zenith range $0 \ldots 180^\circ$ is allowed for the likelihood reconstruction. We perform an additional reconstruction with the zenith range restricted to downward pointing tracks. This results in the best hypothesis for the muon direction under the assumption that it is a downgoing muon track. Furthermore, a zenith dependent prior [Hil01] is added to the likelihood (6.5). This is motivated by the Bayesian theorem: if an observed event belongs to a set of events E (e.g. with a certain hit pattern) and is known to be contained in a set M (e.g. atmospheric muons with zenith angle $\theta \ldots \theta + d\theta$), the probability to observe this event class E is

$$P(E|M) = \frac{P(M|E) \cdot P(E)}{P(M)}. \tag{6.9}$$

We want to maximize $P(M|E)$, the probability that the event was caused

	selection cut	passing rate		
		exp. data	E^{-2} ν	atm ν
Direct walk	$\theta > 70^\circ$	3.0%	90.6%	93.6%
Pandel reconstruction	$\theta > 80^\circ$	0.4%	86.4%	90.6%

Table 6.2: Cuts on reconstruction observables at level 2. The cumulative passing rates of the two cuts are listed for experimental data and simulated up-going ($\theta > 90^\circ$) neutrino events.

by an atmospheric muon from a certain direction. Since $P(E)$ is constant (independent of the hypothesis M), we have to maximize

$$P(E|M) \cdot P(M) \propto P(M|E), \tag{6.10}$$

i.e. instead of maximizing the likelihood $e^{-\mathcal{L}} \equiv P(E|M)$ defined by 6.5, the product of $e^{-\mathcal{L}}$ and a prior $P(M)$ has to be maximized. The prior describes the probability of detecting events from a certain zenith angle which is proportional to the atmospheric muon flux from that direction at the depth of the AMANDA detector. This prior changes by six orders of magnitude from $\theta = 0^\circ$ (vertically downgoing) to $\theta \approx 85^\circ$.

Level 2 selection

Cuts based on zenith angles obtained from direct walk and Pandel reconstruction (Tab. 6.2) reduce the experimental data set to $4.9 \cdot 10^6$ events (0.4% of all triggered events). The passing rate (relative to the trigger level) for up-going E^{-2} signal events is 86%, for up-going atmospheric neutrino events 91%.

Based on this "level 2" data set[2], quality cuts have been developed to select an event sample containing almost no misreconstructed events.

6.3 High level cuts

The different track reconstructions and the cascade reconstruction described in the previous section provide a series of observables which are a measure for the quality of the Pandel reconstruction result.

- A subset of observables used for the separation of well reconstructed (mainly atmospheric) neutrino events and misreconstructed events is based on experiences from earlier point source searches [Bir02, You01] and an atmospheric neutrino selection [Boe02]: in these analyses, the

[2] A cut level 1 is defined by weaker cuts: $\theta_{\mathrm{DW}} > 70^\circ$ and $\theta_{\mathrm{Pandel}} > 70^\circ$. The additional reconstructions described in this section, which are needed for the further selection, are available only for the reduced level 2 data set.

concept of "direct" hits proved efficient for the selection of well reconstructed events.

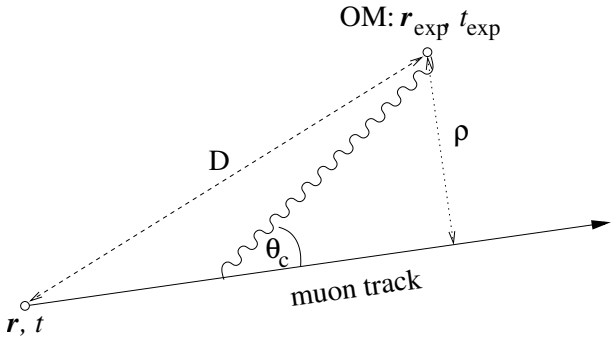

Figure 6.3: Notations for the calculation of the expected arrival time. A muon track with the vertex $(\mathbf{r}, t)$ emits photons under the Cherenkov angle which arrive at the OM at $(\mathbf{r}_{\rm exp}, t_{\rm exp})$ at a distance ρ from the track and at a distance D from the track vertex.

Under the assumption of a certain track hypothesis, direct hits are defined as hits which have an arrival time $t_{\rm hit}$ consistent with the expected arrival time of unscattered photons. The photons are assumed to be emitted under the Cherenkov angle from the muon track with vertex $(\mathbf{r}, t)$ and to travel unscattered to the optical module at a distance D from the vertex, as indicated in Fig. 6.3. The expected arrival time is then:

$$\begin{aligned} t_{\rm exp} &= t + ((\sqrt{D^2-\rho^2} - \frac{\rho}{\tan\theta_c}) \cdot \frac{1}{c_{\rm vac}} + \frac{\rho}{\sin\theta_c} \cdot \frac{1}{c_{\rm ice}} \\ &= t + (\sqrt{D^2-\rho^2} + \rho\sqrt{n^2-1})/c_{\rm vac}. \end{aligned}$$

The time residual in this analysis is restricted to

$$-15\text{ns} < \Delta t \equiv t_{\rm hit} - t_{\rm exp} < 25\text{ns}, \tag{6.11}$$

unless otherwise indicated. For the event selection, we use the number $N_{\rm dir}$ of these hits as well as the distance $L_{\rm dir}$ of the first and last direct hit, projected onto the reconstructed track.

- Another quality criterion is the "smoothness" of the hit distribution along the assumed muon track. This is motivated by the fact that, for a well reconstructed track, light is emitted continuously along this track (except for events with high energy secondary cascades produced along the muon track). In contrast, misreconstructed tracks typically show a good agreement with part of the hits, while hits are missing in the center or one or more additional clusters of hits are present in a remote part of the detector. This has been observed especially for downgoing muons from independent, almost simultaneous air showers [Boe02]: if one muon crosses the detector in the bottom of the detector a few μs before a second muon crossing a few 100 m above, this event

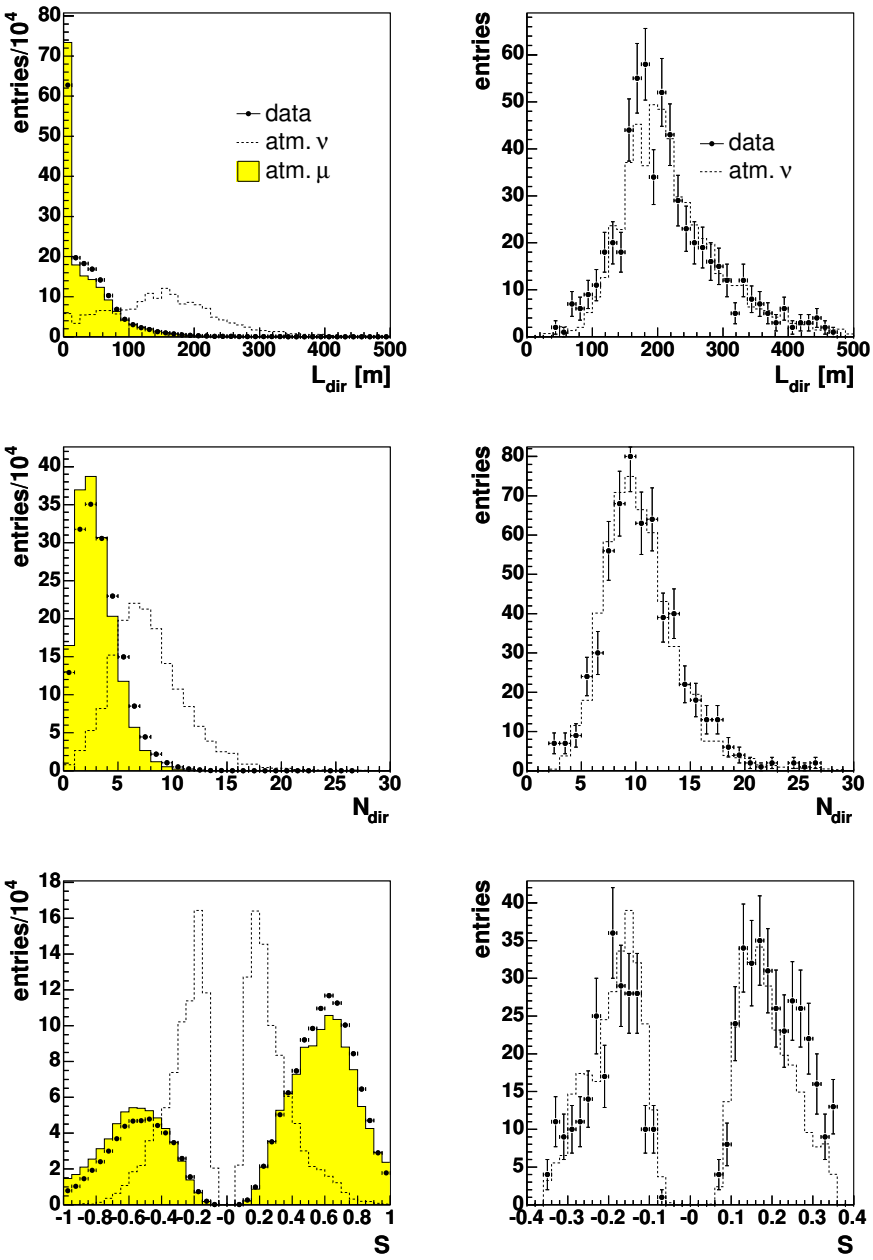

Figure 6.4: Distribution of the track length L_{dir}, number of direct hits N_{dir} and the smoothness $\mathcal{S}$ at level 2 (left; all three distributions normalized to the number of observed data events) and for the final data sample (right; atmospheric neutrino prediction scaled down by 14% as derived in section 6.6.1). Selected data events are shown in comparison to simulated atmospheric neutrino and muon events. Events with a reconstructed declination $\delta < 10^{\circ}$ are excluded from the plots. The simulated atmospheric muon events which remain after the final selection (4 events reconstructed with $\delta > 0^{\circ}$ in 54 d simulated lifetime) are not shown.

can be wrongly reconstructed as one upward moving muon connecting hits originating from two different muons.

To reject this type of misreconstructed tracks, all optical modules are numbered in the order of the projection $L_i = (\mathbf{r_i} - \mathbf{r}) \cdot \mathbf{u}$ of their location $\mathbf{r_i}$ onto the track (vertex and unit direction $\mathbf{r}$, $\mathbf{u}$). With $N_i = 0, 1$ denoting whether OM i recorded a hit and p_i the hit probability in each OM, the smoothness is defined as the maximum deviation of the observed and expected hit numbers:

$$\mathcal{S} \equiv \pm \max_{\{k=1..N_{\mathrm{OM}}\}} \left| \frac{\sum_{i=1}^{k} N_i}{\sum_{i=1}^{N_{\mathrm{OM}}} N_i} - \frac{\sum_{i=1}^{k} p_i}{\sum_{i=1}^{N_{\mathrm{OM}}} p_i} \right|. \tag{6.12}$$

The sign is chosen to be positive if at the maximum deviation the observed cumulative hit number is larger than expected, otherwise negative. For this calculation, only hits with a time residual -15 ns $< \Delta t < 75$ ns and a distance $\rho < 90$ m from the reconstructed track are considered.

- For well reconstructed tracks, different reconstruction methods (first guess, iterative likelihood reconstruction and MPE-reconstruction) are expected to yield similar results, while for misreconstructed events it is more likely that the three reconstructed directions differ considerably. This leads to the observable

$$\Delta\Psi \equiv \arccos\left(\frac{1}{N} \sum_{i=1}^{N} \mathbf{u_i} \cdot \mathbf{u_{mean}}\right), \tag{6.13}$$

the mean deviation of the direction vectors of the $N = 3$ reconstructions from their average direction $\mathbf{u_{mean}} = \frac{1}{N} \sum_{i=1}^{N} \mathbf{u_i}$.

- The likelihoods $\mathcal{L}^{\mathrm{red}}_{\mathrm{track}}$ and $\mathcal{L}^{\mathrm{red}}_{\mathrm{casc}}$ of the muon and the cascade likelihood reconstructions are related to the quality of the reconstruction: for well reconstructed track-like events, a good track likelihood (small $\mathcal{L}^{\mathrm{red}}_{\mathrm{track}}$) and a bad cascade likelihood are expected. The observables chosen for selection of well reconstructed tracks are $\mathcal{L}^{\mathrm{red}}_{\mathrm{track}}$ and $\mathcal{L}^{\mathrm{red}}_{\mathrm{track}} - \mathcal{L}^{\mathrm{red}}_{\mathrm{casc}}$.

- Many events reconstructed approximately horizontally (i.e. the minimum of the Pandel likelihood is at $0^\circ < \delta \lesssim 20^\circ$) have a maximum $e^{-\mathcal{L}_{\mathrm{ZW}}}$ of the zenith weighted likelihood which is only slightly worse than $e^{-\mathcal{L}_{\mathrm{Pandel}}}$. According to Bayes' theorem, these events are likely to be misreconstructed. Therefore, a cut on the difference

$$\Delta\mathcal{L} \equiv \mathcal{L}_{\mathrm{Pandel}} - \mathcal{L}_{\mathrm{ZW}}. \tag{6.14}$$

efficiently reduces the background of misreconstructed downward going muons.

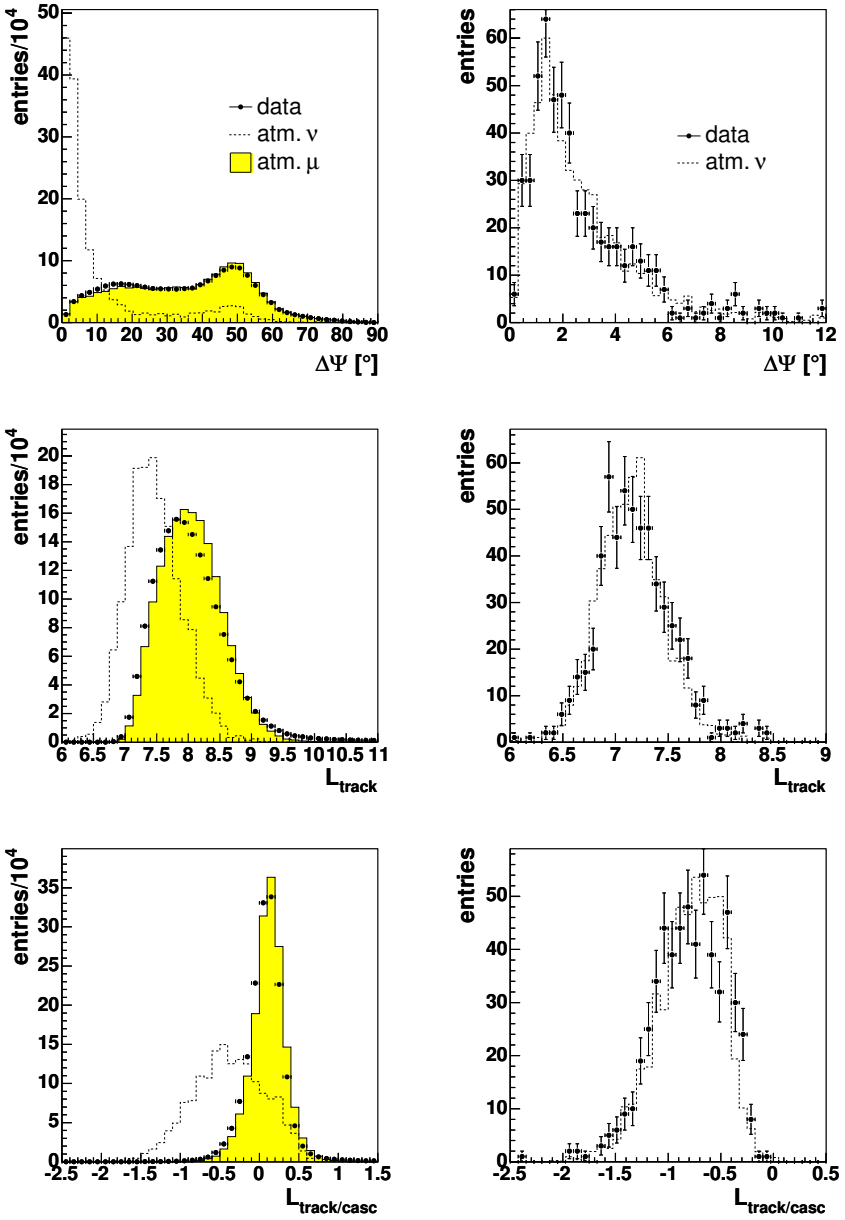

Figure 6.5: Distribution of the angular deviation $\Delta\Psi$, the track likelihood $\mathcal{L}^{\mathrm{red}}_{\mathrm{track}}$ and the difference of track and cascade likelihoods $\mathcal{L}^{\mathrm{red}}_{\mathrm{track}} - \mathcal{L}^{\mathrm{red}}_{\mathrm{casc}}$. Details are described in Fig. 6.4.

For the final event selection, the first 6 of the described variables are combined by a neural network (cf. following section) to a single variable related to the quality of the event reconstruction. In addition to a cut on

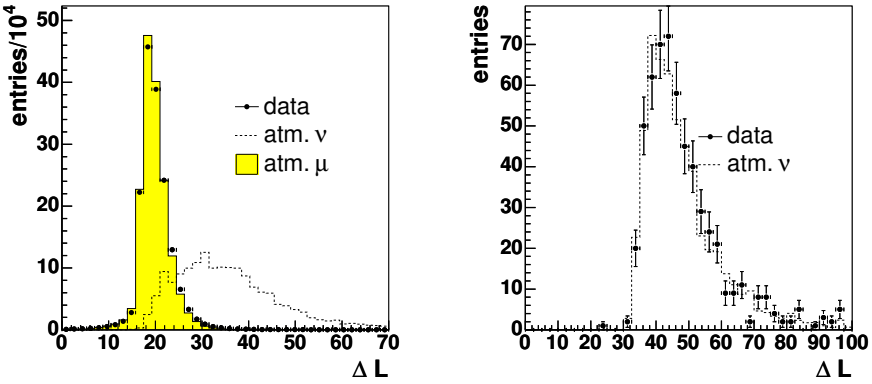

Figure 6.6: Distribution of $\Delta\mathcal{L} = \mathcal{L}_{\mathrm{Pandel}} - \mathcal{L}_{\mathrm{ZW}}$, the likelihood difference between Pandel and zenith weighted reconstruction at level 2 (*left*) and at final level (*right*). Details are described in Fig. 6.4.

this event quality, a cut on the likelihood difference $\mathcal{L}_{\mathrm{Pandel}} - \mathcal{L}_{\mathrm{ZW}}$ will be applied. The distributions of the 6 variables entering the neural network and of the likelihood ratio are shown in Fig. 6.4, 6.5, and 6.6 once after the level 2 selection and once for the final data sample (defined in section 6.4). At level 2, the separation power of the single variables to distinguish between well reconstructed up-going events (atmospheric or signal neutrinos) and misreconstructed events (simulated atmospheric muons and the dominant fraction of observed data at level 2) is obvious. At the final selection level, the distributions of remaining data events are in good agreement with the expectation from atmospheric neutrino simulation.

6.3.1 Neural network

The standard approach of applying several cuts on single variables each of which improves the separation of signal from background is not optimal for two reasons: firstly, correlations between the variables are not utilized. Secondly, the optimization of the cut values in a multidimensional space can be very time consuming. This is especially important in the case of this analysis in which cuts are optimized multiple times at different zenith angles.

Artificial neural networks (NN) have the advantage of reducing the multi-dimensional set of observables to a single event quality. The final cut for the selection of the point source analysis will be composed of a cut on an event quality based on a NN and a cut on the likelihood difference $\Delta\mathcal{L}$. These two cut parameters will be optimized separately for different declination bands of 5° width each.

A NN can be understood as a simplification of the structure of neurons connected via dendrites and axons in the human brain: a signal received at one of the dendrites contributes to the electrical potential of the neuron's nucleus. The neuron "fires" (emits an electrical pulse to neighboring neurons) if the potential reaches a threshold. The weights with which input signals contribute to the neuron's potential and the threshold are adapted during a learning phase.

The type of artificial NNs applied in this work, the feed-forward NN (e.g. [RMS91]), consists of several units $x_i^{(l)}$ (corresponding to the neurons) grouped in layers l. The layer $l = 0$ contains the input variables, i.e. the observables used for the classification of an event. These values are restricted to the interval [0, 1] by monotonous transformations. Each unit adds up the output values of the previous layer with different weights $w_{ij}^{(l)}$ and generates an output value according to

$$x_i^{(l)} = \Theta(\sum_j w_{ij}^{(l)} x_j^{(l-1)} - b_i^{(l)}). \tag{6.15}$$

$\Theta(x)$ is a sigmoid function, $\Theta(x) = (1 + e^{-x/\xi})^{-1}$. ξ defines the size of the interval in which the output changes from ≈ 0 to ≈ 1. This transition takes place around the threshold $b_i^{(l)}$. We choose $\xi = 1$.

The NN used for this analysis consists of 3 layers: input layer $l = 0$, hidden layer $l = 1$ and output layer $l = 2$. The output layer contains only one unit, which will be used as a measure of the reconstruction quality $Q_{\mathrm{NN}} \equiv x_0^{(2)}$. In the limit $\xi \to 0$, for n_0 input units and n_1 units in the hidden layer, the condition $x_0^{(2)} = 1$ selects a region in the n_0-dimensional cut space restricted by n_1 hyperplanes. For $n_1 \geq n_0$ this is a generalization of the application of single cuts $x_i^{(0)} \geq x_i^{\min}$, $i = 0 \ldots n_0$. A further generalization is introduced by $\xi > 0$ which allows variation in the tightness of the cut.

NN input variables

Six of the seven described observables are used as input variables for the NN: number N_{dir} and distance L_{dir} of direct hits, angular deviation $\Delta\Psi$ between three different track fits, track and cascade likelihood $\mathcal{L}_{\mathrm{track}}^{\mathrm{red}}$, $\mathcal{L}_{\mathrm{track}}^{\mathrm{red}} - \mathcal{L}_{\mathrm{casc}}^{\mathrm{red}}$, and the smoothness $|\mathcal{S}|$.

The input variables are transformed to the range $0 \ldots 1$ by affine transformations and truncation:

$$
\begin{aligned}
x'_0 &= |\mathcal{S}| && (6.16)\\
x'_1 &= L_{\mathrm{dir}}/400\mathrm{m} && (6.17)\\
x'_2 &= \Delta\Psi/90^\circ && (6.18)\\
x'_3 &= (\mathcal{L}^{\mathrm{red}}_{\mathrm{track}} - \mathcal{L}^{\mathrm{red}}_{\mathrm{casc}})/2 + 0.5 && (6.19)\\
x'_4 &= N_{\mathrm{dir}}/30 && (6.20)\\
x'_5 &= \mathcal{L}^{\mathrm{red}}_{\mathrm{track}}/9 - 2/3 && (6.21)\\
x_i^{(0)} &= \begin{cases} x'_i & \text{if } 0 \le x'_i \le 1 \\ 0 & \text{if } x'_i < 0 \\ 1 & \text{if } x'_i > 1 \end{cases} && (6.22)
\end{aligned}
$$

In the hidden layer, also six units are used, and one unit in the output layer is interpreted as event quality. The structure of the NN is visualized in Fig. 6.7.

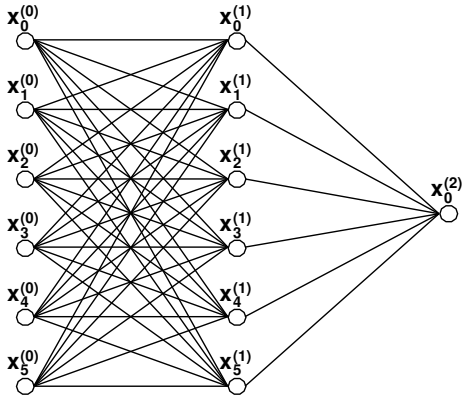

Figure 6.7: Structure of the NN: input and hidden layer with 6 units each, one unit in the output layer. Signals are propagated from left to right according to (6.15).

Training of the NN

The parameters of the NN (weights and thresholds) are obtained in a training phase. For this training, an event sample of simulated atmospheric muon events (*background* sample) and a simulated event sample of upward moving neutrinos following an E^{-2} spectrum (*signal* sample) are used[3]. Depending

[3] Usually neural networks are trained with an event sample composed of signal events with teaching output 1 and background events with teaching output 0. In the present analysis we cannot simply assign a quality 1 to all simulated up-going neutrino events, but must define the teaching output based on the reconstruction quality, i.e. the angular

on the space angle $\Psi(\text{true}, \text{reco})$ between the directions of the simulated and the reconstructed tracks, the teaching output value has been set to

$$Q_{\text{teach}} \equiv \frac{1}{1 + e^{-(\Psi(\text{true,reco})/(1^\circ)-3)}} \tag{6.23}$$

$$\approx \begin{cases} 0 & \text{if } \Psi \gg 3^\circ \\ 1 & \text{if } \Psi \approx 0. \end{cases} \tag{6.24}$$

The aim of training of the NN is to reduce the error of the obtained output values compared to the teaching values, averaged over the training sample:

$$\mathcal{E} \equiv \frac{1}{N_{\text{train}}} \sum_{i=1}^{N_{\text{train}}} |x_0^{(2)} - Q_{\text{teach}}| \stackrel{!}{=} \min, \tag{6.25}$$

i.e. in the optimum case ($x_0^{(2)} = Q_{\text{teach}}$ for all events) the NN output value $Q_{\text{NN}} = x_0^{(2)}$ increases with the accuracy of the angular reconstruction. The angle 3° for the transition from low to high teaching output values has been chosen according to the optimized search bin size obtained in a preliminary point source analysis, with an event selection independent of a NN. The sensitivity which can be reached with the NN selection depends only weakly on the precise definition of the teaching output values, as we will show in section 6.5.3.

This minimization problem (6.25) is approximately solved by the gradient descent method [RMS91] which iteratively adapts the (initially randomly chosen) NN parameters to reduce the average NN error $\mathcal{E}$ with the number of training cycles as shown in Fig. 6.8. In total, 150 training cycles have been executed. The learning parameter, which determines the step size of the gradient descent method, was decreased from initially 0.2 by a factor 0.9 after every five steps resulting in a learning parameter 0.009 for the last five cycles. The error has also been calculated for a validation sample consisting of a statistically independent set of simulated events. The separation of the two curves in Fig. 6.8 at more than 70 cycles is an indication of an "overtraining" of the NN, i.e. an adjustment of the parameters to features of the training sample caused by limited statistics. The learning actually could have been stopped after about 70 cycles, because the following cycles only decrease the error of the training sample. However, since the output error of the validation sample remains approximately constant after additional training cycles, there is no reason to expect a bad efficiency of the NN.

The obtained NN parameters for the calculation of the event quality according to (6.15) are listed in Tab. B.3 on page 114.

The small relative decrease of the average NN error from 0.21 to 0.17 (and even smaller for the validation sample) seems to indicate a bad performance

mismatch. Our *signal* sample will therefore contain both well reconstructed and badly reconstructed events, while the *background* sample comprises only misreconstructed events.

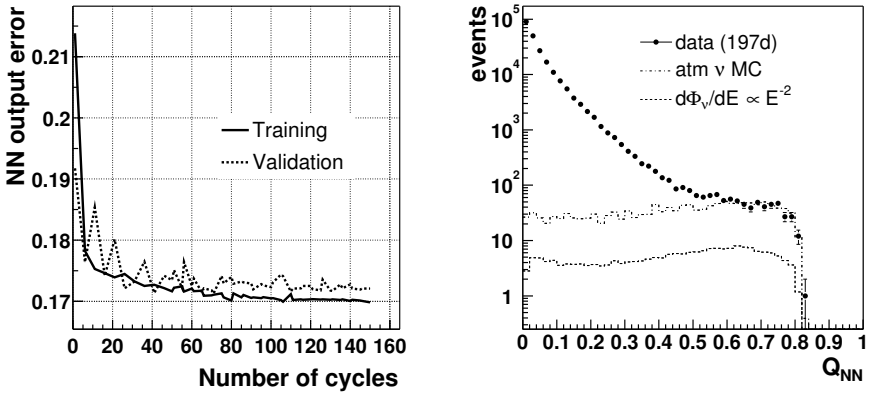

Figure 6.8: *Left:* Decrease of the output error averaged over the training (solid curve) and the validation sample (dashed curve) as a function of the number of training cycles. *Right:* Distribution of the NN output value Q_{NN} at level 2, restricted to reconstructed zenith angles $\theta > 100°$. The comparison to the atmospheric neutrino simulation shows that applying a cut $Q_{\mathrm{NN}} > 0.5$ leads to an event sample dominated by atmospheric neutrinos. Also shown is the Q_{NN} distribution for a hypothetical isotropical neutrino flux $\frac{\mathrm{d}\Phi_\nu}{\mathrm{d}E} = E^{-2} \cdot 10^{-6}$ GeV cm^{-2} s^{-1}. The passing rate of the cut at $Q_{\mathrm{NN}} > 0.5$ is 47% for both atmospheric and E^{-2} spectrum.

of the NN. However, as demonstrated in Fig. 6.9, there is a considerable improvement of the NN performance during the training: the random NN parameters before training result in small Q_{NN} output values for almost all events (peak at $Q_{\mathrm{NN}} \approx 0.09$). The combination of the *signal* sample containing about 36% badly reconstructed events ($\Delta\Psi_{\mathrm{true,reco}} > 6° \Rightarrow Q_{\mathrm{NN}} \approx 0$) and the *background* sample with only badly reconstructed events leads to the small average error. The reduction of the NN output error is obvious in Fig. 6.9(b) especially for well reconstructed events: in the region $\Delta\Psi \lesssim 3°$ the values of Q_{NN} are shifted from about 0.09 (obtained with random NN parameters, i.e. with an "untrained" NN) to larger values, which are close to the demanded teaching value Q_{teach}. The optimum would be a distribution $Q_{\mathrm{NN}} = Q_{\mathrm{teach}}$ for all $\Delta\Psi$. This cannot be reached, but the error $|Q_{\mathrm{NN}} - Q_{\mathrm{teach}}|$ is reduced to less than about 0.3 for most well reconstructed tracks and from 0.09 to about 0 for badly reconstructed events.

Finally, the performance of the NN is best demonstrated by the resulting sensitivity, as described in the following section.

6.4 Cut optimization

The level 2 data sample extracted with two cuts on reconstructed zenith angles as described in Tab. 6.2 still comprises mainly misreconstructed

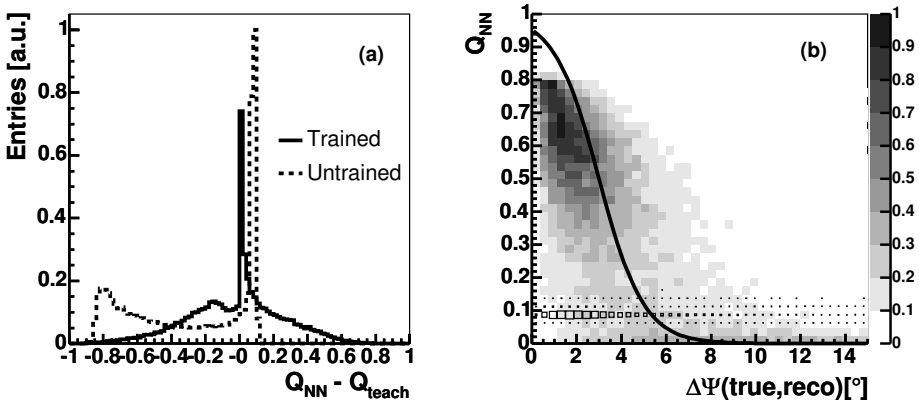

Figure 6.9: *Left*: NN error for output values from the *signal* sample calculated with random NN parameters ("untrained") and after NN training. *Right*: Q_{NN} versus space angle reconstruction mismatch. The grey scale histogram shows the distribution after NN training, the boxes indicate the distribution if random NN parameters are used. The solid curve shows the teaching value $Q_{\mathrm{teach}}(\Delta\Psi)$ defined by (6.23), which would be reached in the optimal case.

atmospheric muon events. Applying further quality cuts, we can achieve a strong enhancement of well reconstructed events, i.e. atmospheric neutrinos and a possible signal contribution from astrophysical neutrino point sources.

In the previous sections, the variables have been described which will be used for selection of well reconstructed events:

- the neural network output value Q_{NN}, a combination of six single observables (6.16)–(6.21),
- the likelihood difference $\Delta\mathcal{L}$ between Pandel and zenith weighted reconstruction, and
- the smoothness $\mathcal{S}$, which is used in the calculation of Q_{NN}, and also separately with a fixed cut $|\mathcal{S}| < 0.36$.

The latter cut has been applied to reduce the aforementioned background of coincident muons from approximately simultaneous air showers. This background class is not contained in the simulated background event sample for the training of the NN. Therefore, coincident muon events might be rejected only very inefficiently by the cut on Q_{NN}, and the separate cut on $\mathcal{S}$ has been chosen to avoid a significant contribution of this event class to the final data sample. 18% of level 2 experimental data reconstructed as up-going pass the cut, the passing rate for a signal of up-going neutrinos following an E^{-2} spectrum is 79% and for atmospheric neutrinos 78%.

δ	$R_{\mathrm{bin}}[^\circ]$	Q_{NN}	$\Delta\mathcal{L}$	n_{bg}	n_{sig}	μ^{90}	Φ^{sens}
-5.0	2.6	0.38	25	9.66	8.83 (13%)	6.67	7.55
0.0	4.0	0.40	28	3.11	17.79 (22%)	4.47	2.51
5.0	4.6	0.28	33	1.23	19.84 (26%)	3.44	1.73
10.0	4.0	0.26	36	0.89	17.76 (26%)	3.18	1.79
15.0	4.2	0.22	38	1.08	19.50 (29%)	3.33	1.71
20.0	4.4	0.30	33	2.27	22.69 (38%)	4.08	1.80
25.0	4.6	0.22	42	0.97	17.89 (33%)	3.25	1.82
30.0	4.6	0.26	37	1.83	20.05 (40%)	3.83	1.91
35.0	3.4	0.32	34	1.32	20.81 (42%)	3.51	1.68
40.0	3.6	0.32	34	1.56	18.49 (41%)	3.66	1.98
45.0	3.6	0.42	31	1.58	20.73 (49%)	3.68	1.77
50.0	3.0	0.32	41	0.86	18.37 (44%)	3.16	1.72
55.0	3.2	0.36	34	1.80	19.38 (49%)	3.82	1.97
60.0	2.6	0.44	41	0.84	14.75 (42%)	3.15	2.13
65.0	3.2	0.46	47	0.79	13.78 (45%)	3.11	2.26
70.0	2.6	0.60	21	0.80	15.10 (47%)	3.11	2.06
75.0	3.4	0.52	49	1.09	13.77 (46%)	3.34	2.42
80.0	2.8	0.50	38	1.62	13.94 (46%)	3.70	2.66
85.0	3.4	0.66	21	2.21	13.12 (46%)	4.05	3.09

Table 6.3: Optimized bin size and quality cuts and reached sensitivities at different declinations. n_{bg} is the number of expected background events in the search bin, derived from the number of observed data events at $|\delta - \delta_{\mathrm{reco}}| < R_{\mathrm{bin}}$. This defines the average upper limit on the signal contribution μ^{90}. n_{sig} is the number of expected signal events for a neutrino flux $\mathrm{d}N_\nu/\mathrm{d}E_\nu = E_\nu^{-2} \cdot 10^{-6}$ GeV s^{-1} cm^{-2} from a point source at declination δ. In brackets, the passing rate for signal events is listed, relative to cut level 2. $\Phi^{\mathrm{sens}} \cdot E^{-2} = \mu^{90}/n_{\mathrm{sig}} \cdot 10 \cdot E^{-2}$ is the sensitivity for a neutrino flux (assuming $\mathrm{d}\Phi/\mathrm{d}E \propto E^{-2}$) in units 10^{-7} GeV s^{-1} cm^{-2}.

We optimize the two cuts on Q_{NN} and $\Delta\mathcal{L}$, as described in section 5.2, with the aim of best average upper neutrino flux limits for point sources. For this purpose, we calculate at different declinations ($\delta = -5^\circ, 0^\circ, ..., 85^\circ$) the expected number of background events n_b and the expected number of signal events n_{sig} from a point source spectrum[4] $\mathrm{d}\Phi_\nu/\mathrm{d}E = E_\nu^{-2} \cdot 10^{-6} \cdot$ GeV cm^{-2} s^{-1} as a function of the two cut values and the radius R of the circular search bin. According to (5.5), the average flux limits for a certain assumed energy spectrum are proportional to the "model rejection factor"

$$\mathrm{MRF}(n_b, n_{\mathrm{sig}}) \equiv \frac{\langle \mu^{90}(n_b) \rangle}{n_{\mathrm{sig}}}. \tag{6.26}$$

With n_b and n_{sig} depending on the cut values and on the search bin radius

[4]The normalization of the source spectrum is arbitrary.

R, the MRF is a function of three variables. Its minimum is approximately found by evaluating the function with sufficiently small step sizes for each variable. The results are listed in Tab. 6.3, and the dependence of the MRF on the chosen cut and bin size are shown in Fig. 6.10 for a fixed declination. For each of the three sub-figures, we fix two of the three cut parameters to the optimum values listed in the table and vary only the cut parameter shown at the x-axis. The final selection cut changes every 5° in the zenith angle, i.e. we apply the cut parameters optimized for a source at the declination δ_{opt} to events with reconstructed zenith angles between $\delta_{\mathrm{opt}} + 90° - 2.5°$ and $\delta_{\mathrm{opt}} + 90° + 2.5°$.

A comparison of the reached neutrino flux sensitivity of about $\frac{\mathrm{d}\Phi}{\mathrm{d}E} \approx 2 \cdot 10^{-7}$ GeV s^{-1} cm$^{-2} \cdot E^{-2}$ at declinations $\delta > 5°$ to limits obtained with the B10-detector [A$^+$03c] shows an improvement[5] by a factor of 5. Close to the horizon ($0° < \delta \lesssim 15°$), the sensitivity is improved by more than one order of magnitude.

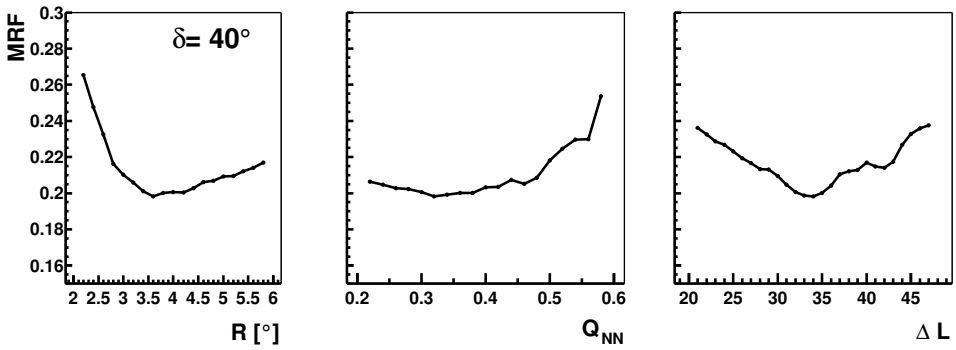

Figure 6.10: Dependence of the MRF on bin size and quality cuts on Q_{NN} and $\Delta\mathcal{L}$, for a neutrino flux $\mathrm{d}\Phi_\nu/\mathrm{d}E = E^{-2} \cdot 10^{-6}$ GeV s^{-1} cm^{-2} from a simulated point source at $\delta = 40°$. For each plot, the two other parameters have been fixed at the values listed in Tab. 6.3.

6.5 Possible improvements

Using a neural network for data analysis has the disadvantage of obscuring its functionality by calculating a multidimensional function, which depends on several input variables and parameters. This results in two difficulties:

[5] For this comparison, one should take into account the smaller lifetime (130 d) which was available for the B10 analysis, compared to 197 d in the current analysis. A recent analysis [Con03] of data recorded in 1999, restricted to the B10 sub-detector, with 224 d lifetime, reaches sensitivities in the range $\frac{\mathrm{d}\Phi}{\mathrm{d}E} \approx (6-8) \cdot 10^{-7}$ GeV s^{-1} cm$^{-2} \cdot E^{-2}$.

- to check if the optimal performance has been achieved and
- to check if there are systematic differences in the distributions of the NN input variables between observed and simulated data.

The second task is more critical, since underestimating the systematic uncertainties would lead to wrong results (e.g. possibly too low flux limits). We will investigate these uncertainties in the following section. In contrast, a suboptimal design of the NN would lead to non-optimal, but valid limits.

There are different possibilities of different NN training methods which are to be tested for yielding better results than the method described so far:

- Using experimental data instead of simulated background events or
- varying the contribution of well and badly reconstructed events to the training sample or
- varying the teaching output function.

We also investigate the possible improvement of limits if a cut on the number of hit channels (related to the muon energy) is added. The relative change in sensitivity is shown in Fig. 6.11 for the different modifications.

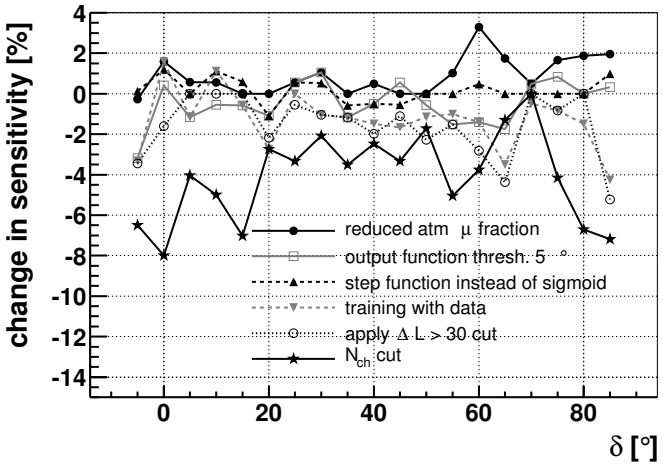

Figure 6.11: Relative change of the sensitivity vs. declination for E^{-2} neutrino fluxes with different NN training methods. For all methods, the cuts and the bin size have been optimized in 5° steps in declination. Note that a decrease of the sensitivity means that the altered method is better than the default method.

6.5.1 Training with experimental data

The NN has been trained with simulated signal and background events. Instead of the background simulation, experimental data might be used (with a teaching output 0), since the data set reduced to the level used for NN training contains about 99.9% misreconstructed events. The training with simulated events has the advantage that inaccuracies of the simulation would effect well reconstructed and misreconstructed tracks in the same way. The disadvantage is that mismatches in the distributions of the NN input variables between data and simulated background events (section 6.6.5) deteriorate the efficiency of the NN. For this reason, the NN has been alternatively trained with experimental data and simulated signal. The reachable sensitivities after the same optimization as for the default NN improve by at most 4% as shown in Fig. 6.11.

6.5.2 Training with varying signal and background contributions

The efficiency of the NN might be dependent on the relative contributions of well reconstructed and misreconstructed events in the training sample. For the default training, the ratio of *signal* to *background* events is about 2:1. With 39% of the *signal* events being well reconstructed ($\Delta\Psi < 3^\circ$), the fraction of well reconstructed events in the complete training sample (composed of *signal* and *background* events) is about 26%. The effect of increasing this fraction to 50% is shown in Fig. 6.11: The sensitivities get slightly worse at most simulated declinations. Also with other *signal* to *background* ratios in the training sample, no significant improvement could be observed.

Including only events which pass the $\Delta\mathcal{L}$ cut also changes the relative contribution of signal and background events. This cut has not been applied when the NN training sample was created, although it might be expected that training would be more efficient if the same cuts are applied which will also be used for the final analysis. The training was done with data events as *background*, since the number of simulated atmospheric muon events passing this cut is too low for the training of the NN. Compared to the corresponding curve ("training with data") in Fig. 6.11, training with events fulfilling $\Delta\mathcal{L}>$ 30 does not lead to a significant change in sensitivity.

6.5.3 Varying the teaching output function

The teaching output has been defined as a function of the space angle mismatch between the simulated and the reconstructed muon track with a smooth transition from 1 to 0 at $\Delta\Psi_{\mathrm{true,reco}} \approx 3^\circ$. The value of this threshold is motivated by the optimized bin size (cf. section 6.4) ranging

from 2.6° to 4.6°. If we increase the threshold to 5° or use a step function instead of the sigmoid function, the sensitivities remain similar to the default values.

6.5.4 Adding energy dependent cuts

Due to the assumed hard signal spectrum $\frac{\mathrm{d}N}{\mathrm{d}E} \propto E^{-2}$ compared to an $E^{-3.7}$ atmospheric neutrino spectrum, a cut on the energy of the initial neutrino would improve the sensitivity and the detection probability.

In practice, the initial neutrino spectrum is distorted by energy dependent absorption and detection efficiency, and we cannot reconstruct the neutrino energy, but only the muon energy with a finite resolution $\sigma(\log_{10} E_{\mathrm{reco}}/E_{\mathrm{true}}) \approx 0.4$ [Gee02]. We investigate the improvement of the sensitivity by adding a cut on the number of hit channels N_{ch}. This variable was also used in searches for a diffuse high energy neutrino flux to single out highly energetic events and proved to be competitive with more sophisticated energy reconstructions [A$^+$03b, Leu01, CS03]. It has been added as a fourth dimension to the cut space. The achievable improvement in sensitivity, as shown in Fig. 6.11, is below 8%.

Summary

The largest improvement can be achieved with the N_{ch} cut. However, in consideration of the still relatively small change and the dependence of the optimal cut position on the signal spectral index, this cut is not applied in the present analysis. Except for the N_{ch} cut, only the training with experimental data instead of simulated atmospheric muon events results in significantly (though only slightly) better sensitivities. For the analysis of data from 2001 on, one might therefore contemplate a training based on experimental data (and *signal* simulation).

6.6 Systematic uncertainties

In this section we describe the uncertainties of the event and the detector simulation, which influence limits on neutrino fluxes from astrophysical point sources. In the presented point source search, with the background being estimated from observed data events, only the signal expectation is affected by these uncertainties. The statistical error on the number of expected background events is accounted for in section 6.6.9.

6.6.1 Atmospheric neutrino flux

Uncertainties of ice and OM properties influence the expected flux of both atmospheric and astrophysical neutrinos. A comparison of the observed

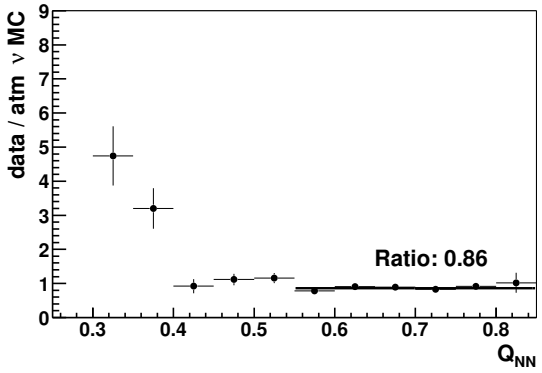

Figure 6.12: Cross check of atmospheric neutrino event rate. The event sample is reduced by tight cuts ($\Delta\mathcal{L} > 35, |\mathcal{S}| < 0.36, L_{\mathrm{dir}} > 150$ m), and the ratio of expected (atmospheric neutrino) to observed event numbers, detected at zenith angles $\theta > 100°$, is shown as a function of the NN quality Q_{NN}. At qualities $Q_{\mathrm{NN}} \gtrsim 0.55$, this ratio remains approximately constant.

to the expected atmospheric neutrino flux provides a possibility to cross check the simulated overall efficiency of the detector. Since the data sample selected for this analysis still contains a considerable number of misreconstructed events, especially close to the horizon, the zenith range for this comparison is restricted to $\delta > 10°$, and tight cuts are applied to achieve a high purity of atmospheric neutrinos. The ratio of the observed event rate compared to the expected atmospheric neutrino event rate [Lip93] is plotted as a function of the NN event quality (Fig. 6.12). An approximately constant ratio of 0.86 at $Q_{\mathrm{NN}} \gtrsim 0.55$ indicates that the observed data at this cut level make up an almost pure sample of atmospheric neutrinos.

In [A$^+$04a], this factor was taken as a normalization factor to the simulated detector efficiency. This leads to a systematic uncertainty of 25% (the uncertainty of the atmospheric neutrino flux [GH02]) for all simulated event rates, which accounts for the summed uncertainties of all detection and analysis efficiencies.

In the present analysis we choose another approach: The observed event rate being 14% smaller than the theoretical expectation is well within the 25% uncertainty of the expectation itself. Therefore, the expectation from atmospheric neutrino simulation is not normalized to the number of observed data events. Instead, the parameters which influence the detection efficiency for signal events are varied within reasonable ranges, and the resulting changes in the expected signal rate determine the systematic uncertainties. In view of the assumed harder signal spectra compared to the atmospheric neutrino spectrum, this additional effort is justified to obtain reliable estimates of the uncertainties.

6.6.2 Ice properties

As mentioned in section 4.2, the ice parameters like scattering and absorption length are known only with a limited precision. The adaptation of direct measurements (KGM model) to observed time residual distributions from atmospheric muon data requires an increased absorption coefficient. This leads to a lower over-all number of detected photons in the MAM model and therefore, for soft spectra, to a lower predicted signal detection efficiency in the MAM compared to the KGM ice model. At high muon energies however, the production of highly energetic secondaries can deteriorate the quality of the muon track reconstruction. Therefore, the smaller absorption length in the MAM model, leading to a reduced contribution from photons that traveled large distances, can result in better reconstruction qualities and hence larger predicted signal detection efficiencies in the case of hard spectra. As shown in Fig. 6.13 as a function of the declination, the maximum uncertainty due to different ice models is below 6% for an assumed E^{-2} signal spectrum. Uncertainties for different spectra are listed in Tab. 6.5 on page 69.

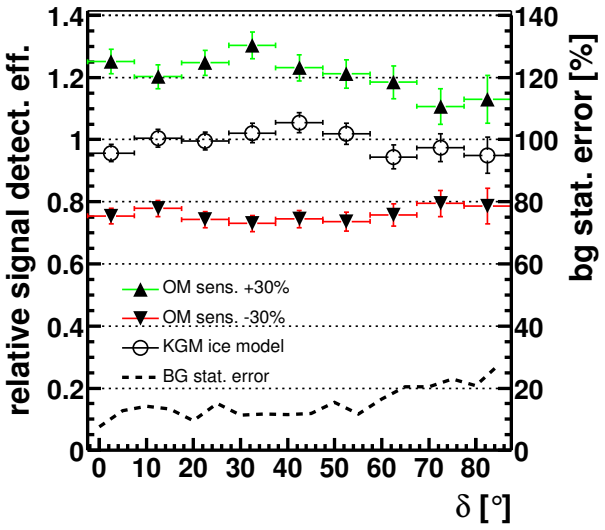

Figure 6.13: Change of E^{-2} signal detection efficiency with respect to the standard simulation versus assumed source declination (left scale). The effect of increased and decreased OM sensitivity as well as varied ice parameters (KGM instead of MAM ice model) is shown. The total systematic uncertainty of the signal detection efficiency is dominated by the uncertainty of the OM sensitivity. The statistical uncertainty of the background expectation described in section 6.6.9 is indicated by the dashed line (scale to the right).

6.6.3 OM sensitivity

The properties of the optical modules which are relevant for their sensitivities - quantum efficiency of the PMT and transmissivity of the glass sphere, gel, and PMT glass - have not been measured individually for each OM before the deployment. The sensitivity might decrease with time due to aging of the optical gel. Laboratory measurements of the transmissivities [Sud01] and an analysis of atmospheric muon events [OW01] indicate uncertainties in the OM sensitivity of ±30%.

We have simulated event samples of up-going E^{-2} signal events with varied OM sensitivities. Fig. 6.13 shows a resulting uncertainty of the number of detectable signal events of up to 30%. The loss or increase of the event numbers is due to events close to the trigger threshold of 24 hits or with a low reconstruction quality due to a relatively low number of hits. For hard energy spectra, there is a larger contribution from events with hit multiplicities well above the trigger threshold. Therefore, the uncertainty of signal event rates decreases with the hardness of the spectrum, as listed in Tab. 6.5.

6.6.4 Interpolation between simulated declinations

Point sources have been simulated at discrete values of the declination from $\delta = 85°$ to $180°$ in steps of $5°$. Between these values, expected signal numbers are obtained by linear interpolation:

$$n_{\mathrm{sig}}(\delta) = n_{\mathrm{sig}}(\delta^-) + (n_{\mathrm{sig}}(\delta^+) - n_{\mathrm{sig}}(\delta^-))\frac{\delta - \delta^-}{\delta^+ - \delta^-}. \qquad (6.27)$$

δ^- and $\delta^+ = \delta^- + 5°$ are the simulated declination values enclosing δ. Another possibility to estimate event numbers at arbitrary declinations would be to count signal event numbers from a small interval ($\Delta(\sin\delta) = 0.1$) using a continuously simulated declination spectrum. This leads to imprecise numbers due to averaging over a declination range with varying detection efficiency. The precision of both methods can be improved by decreasing the distance between simulated discrete declination values or decreasing the $\Delta(\sin\delta)$ interval (requiring a sufficiently large event number in the continuous sample). Comparing both methods, the maximum difference is 11%.

6.6.5 Simulation accuracy of NN input variables

Inaccuracies in the simulation may lead to wrong distributions of the NN input variables, which would result in overestimated or underestimated signal passing rates.

In section 6.3, small deviations between distributions expected from atmospheric neutrino simulation and experimental data (at the final cut level) and between atmospheric muon simulation and experimental data (at cut level 2) have been observed. However, we need not necessarily expect that

simulated distributions of the signal events are subject to inaccuracies of comparable size:

- A remaining contribution of misreconstructed down-going muon events to the experimental data at final cut level causes deviations from the distributions expected from atmospheric neutrino simulation.

- The experimental data and simulated atmospheric muon events at cut level 2 are dominated by misreconstructed events, which constitute less than 1% of all down-going muon events. Since the final event selection in contrast consists of mainly *well* reconstructed events, inaccuracies at cut level 2 do not imply significant inaccuracies of the finally selected signal events.

We choose another event sample to investigate the precision of the simulation: Down-going muon events are available with high statistics both in the experimental data and in the atmospheric muon simulation. Instead of the level 2 zenith cuts listed in Tab. 6.2, we only apply a cut $\theta < 90^\circ$ on the zenith angle obtained from the Pandel likelihood reconstruction to reject a small fraction of events reconstructed in the wrong[6] hemisphere. This event sample (in the following called "minimum bias sample") contains a large fraction of well reconstructed events (51% of the events have an angular mismatch below 3°, 90% below 10°) and can therefore be used for a cross check of the simulation accuracy for well reconstructed signal events. However, one should take into account two differences between the minimum bias data sample and the signal sample:

- The energy dependence of the signal spectrum is expected to be harder than the spectrum of down-going atmospheric muons.

- The detector is not up-down symmetric, since most PMTs are oriented downward. Additionally, the pulses from an upward moving muon with zenith angle θ_{up} arrive at the DAQ system in a shorter period of time than the pulses from a down-going muon with $\theta_{\mathrm{down}} = 180^\circ - \theta_{\mathrm{up}}$ (reflected at the plane $z = 0$ with respect to the up-going muon) due to the cable lengths and therefore pulse delays increasing with the depth.

Except for these differences, we expect similar distributions of the reconstructed variables for minimum bias down-going events and up-going signal events. The largest discrepancy at the final cut level has been observed in the smoothness variable $\mathcal{S}$ in Fig. 6.4. The comparison between minimum bias experimental data and simulated atmospheric muon events in Fig. 6.14

[6] Atmospheric muons, which dominate the event sample at trigger level, are restricted to zenith angles $\theta < 90^\circ$. A reconstruction in the hemisphere $\theta > 90^\circ$ can only be correct for muons from atmospheric (and possibly astrophysical) neutrinos, which however are negligible at trigger level.

shows a better agreement of the smoothness distributions, and the largest disagreement now appears in the N_{dir} variable.

We estimate the influence of the disagreements between simulated and observed distributions of NN input variables on the signal event rates by assigning weights to each event, which depend on one of the six NN variables. The weight functions are obtained from the ratio of histograms (as shown in Fig. 6.14) for experimental data and atmospheric muon simulation. Assuming that all variables except for that one, for which the weight is calculated, are correctly described, this will result in corrected event rates for the simulated minimum bias data sample. Applying the same weight functions to signal events, we can estimate the uncertainty of the signal event rates. The largest change of signal event rates, an increase by 6%, is caused by the N_{dir} dependent weight.

The NN is not only sensitive to one-dimensional distributions of its input variables, so we also investigate the correlation between any two of the six NN input variables, as shown exemplarily in Fig. 6.15 for the smoothness and the number of direct hits. The two-dimensional as well as the one-dimensional distributions for all six NN input variables are shown in appendix A, and the correlation coefficients are listed in Tab. 6.4. Similarly to the previously described method, we assign to each event a weight, which depends on L_{track} *and* $L_{\mathrm{track/casc}}$. For this pair of variables the largest difference of correlation coefficients has been observed between data (0.64) and simulation (0.68). The assignment of the two-dimensional weight function results in a change of the signal event rate by 6%.

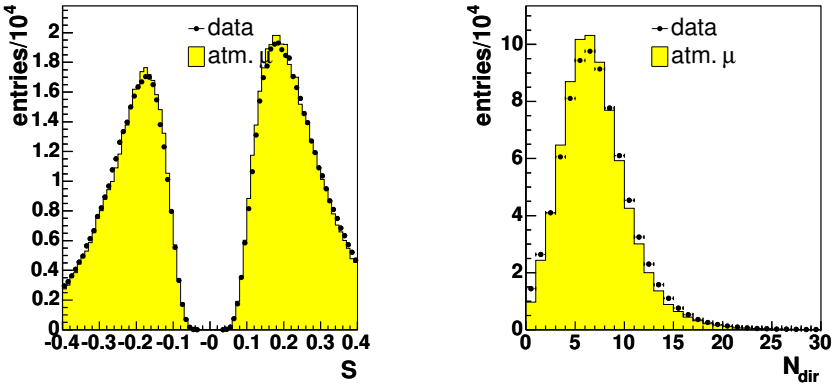

Figure 6.14: Distribution of smoothness (*left*) and number of direct hits (*right*) for minimum bias experimental data and atmospheric muon simulation.

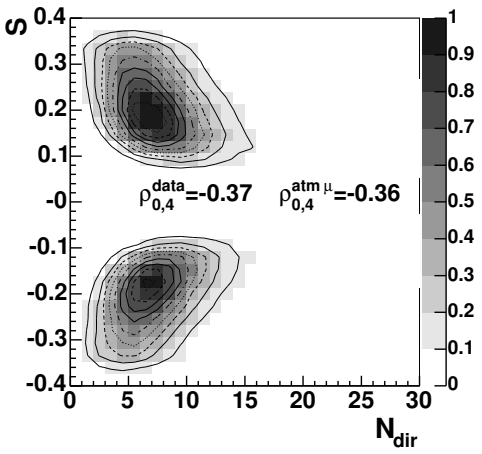

Figure 6.15: Correlation between smoothness and number of direct hits in the minimum bias event sample. Experimental data are shown as grey scale histogram, atmospheric muon simulation by the contour lines. Both distributions have been normalized to a maximum value of 1. The correlation coefficients ρ_{ij} have not been calculated for the shown variables, but for the actual NN input variables $x_i^{(0)}$, which are restricted to the interval [0,1].

	i=1	i=2	i=3	i=4	i=5
j=0	-0.25 (-0.25)	0.11 (0.11)	0.25 (0.27)	-0.37 (-0.36)	0.28 (0.30)
j=1		-0.34 (-0.31)	-0.62 (-0.64)	0.63 (0.64)	-0.44 (-0.48)
j=2			0.40 (0.39)	-0.24 (-0.23)	0.31 (0.34)
j=3				-0.54 (-0.57)	0.64 (0.68)
j=4					-0.60 (-0.63)

Table 6.4: Correlation coefficients ρ_{ij} of the NN input variables $x_i^{(0)}$ for the minimum bias samples of the experimental data and (in brackets) of the atmospheric muon simulation.

6.6.6 Muon propagation

The influence of different muon propagation codes, as described in section 4.1.3, is investigated by processing up-going simulated neutrino induced muons both with PROPMU and with MMC from their production vertex to the transition from rock to ice. In this region, NUSIM uses the PROPMU code for the muon propagation in rock, while in the ice MMC is used by default. Since the distance traveled by the muon in rock is largest for vertically up-going muons, the resulting uncertainties are an upper limit for the uncertainties at lower declinations. The signal event rate expected if MMC is

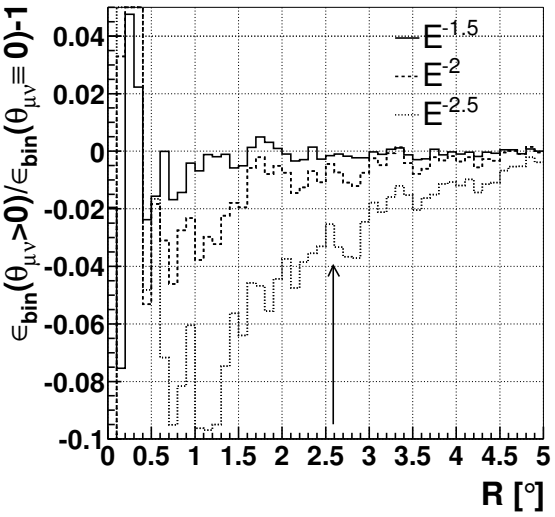

Figure 6.16: Relative correction to the fraction ϵ_{bin} of events reconstructed in a search bin of radius R around the source. Due to the simplified default Nusim simulation (assuming $\theta_{\mu\nu} \equiv 0$), the observable event rates are slightly overestimated. The arrow indicates the smallest bin size of 2.6° used in the present analysis.

used for the propagation in rock of up-going muons induced by neutrinos with an energy dependence $\mathrm{d}\Phi_\nu/\mathrm{d}E \propto E^\gamma$, $3.5 < -\gamma < 1$, differs by less than 2% from the rate obtained with the Propmu propagation.

6.6.7 Calibration uncertainties

Imprecise measurements of OM positions or cable lengths would lead to wrongly calculated time residuals. Uncertainties of 8 ns in the timing offsets and 1 m in OM position (corresponding to an uncertainty of about 4 ns in the time residuals) lead to signal event rate uncertainties of less than 5% [Bir00].

6.6.8 Scattering angle between muon and neutrino

The simplification of the Nusim event generator, to disregard the scattering angle between muon and neutrino, leads to systematically too low flux limits. The Anis generator has been used to calculate the fraction of events which are lost due to the deterioration of the angular resolution if not only the angular deviation between reconstructed and true muon track, but also the angle between neutrino and muon is considered. The result shown in Fig. 6.16 demonstrates that for spectra $\mathrm{d}\Phi/\mathrm{d}E_\nu \propto E_\nu^{-2}$ or harder, the overestimation of event rates in the search bins (with radii 2.6° or larger) is

	Uncertainty [%]		
	$E^{-1.5}$	E^{-2}	$E^{-2.5}$
OM sensitivity	± 19	± 30	± 50
Optical ice properties	$^{+0}_{-12}$	± 6	$^{+18}_{-2}$
Simulation of NN variables	± 6		
Muon propagation	< 2		
Calibration	± 5		
Interpolation	± 11		
Summation	$^{+18}_{-30}$	± 33	$^{+61}_{-45}$
$\theta_{\mu\nu}$ correction	≈ 0	$\lesssim 1$	$\lesssim 4$
Background event number	$\pm 10..27$ (δ dependent)		

Table 6.5: Summary of uncertainties in the signal and background event numbers for different energy spectra. For simplicity, only the maximum positive and negative uncertainties in the range $0° < \delta < 90°$ are listed. The correction for the unsimulated loss of event rate due to the muon neutrino scattering angle does not enter the summed signal uncertainty, but has to be applied separately.

negligible (below 1%). Only for softer spectra ($-\gamma \geq 2.5$) the correction reaches about 4% for the smallest bin size. This correction is still small compared to the systematic uncertainties of up to 50%. However, this correction deteriorates the limits by exactly the value obtained from simulation, while the chosen semi-Bayesian method of including the other systematic uncertainties (cf. section 5.1.1) leads to a smaller relative degradation of the limit than suggested by the estimated maximum uncertainties of the signal event rate.

6.6.9 Statistical error on the number of background events

The expected number of background events in the search bin is known with a relative statistical uncertainty of $1/\sqrt{n_{\text{band}}}$, where n_{band} is the number of events in a declination band with a half width of the search bin radius, as illustrated in Fig. 5.1. At declinations $5° \leq \delta \leq 85°$, n_{band} varies from 111 down to 13, resulting in the statistical uncertainties shown in Fig. 6.13 from about 10% at low declinations up to 27% at $\delta = 85°$.

6.6.10 Summary

The estimated contributions to the signal event rate uncertainties are listed in Tab. 6.5. To estimate the combined uncertainty of the signal event number, the single contributions have been added quadratically taking into account an overall shift in the case of asymmetric intervals. A more precise treatment of systematic errors would be possible if the dependence on the

declination of the assumed point source would be taken into account. For sake of simplicity, the same (maximum) signal uncertainty is assumed for all declinations. The statistical background uncertainty is individually calculated based on the declination of the assumed source position.

The quadratically summed signal uncertainties and the statistical background uncertainty will be used for the calculation of limits according to the method described in section 5.1.1. In the case of soft spectra and small bins, the neglect of the muon neutrino scattering angle in the Nusim simulation has to be separately corrected for by decreasing the simulated signal event numbers, resulting in increased flux limits.

Chapter 7

Characteristics of the event selection

7.1 Effective area

The detector acceptance for signal events can be quantified by the effective area of the detector. Although the effective area does not contain information on the remaining rate of misreconstructed background events, this quantity is useful for comparing different analysis methods or detectors.

The effective neutrino area averaged over an energy range $[E_1, E_2]$ for a certain flux $\mathrm{d}\Phi^{\nu}_{\mathrm{model}}/\mathrm{d}E$ is defined by relating the number of detected signal events n_{sig} to the product of effective area, lifetime and integrated flux:

$$n_{\mathrm{sig}}(E_1, E_2) = A^{\nu}_{\mathrm{eff}}(E_1, E_2) T_{\mathrm{life}} \int_{E_1}^{E_2} \frac{\mathrm{d}\Phi^{\nu}_{\mathrm{model}}}{\mathrm{d}E_{\nu}}(E_{\nu})\mathrm{d}E_{\nu}. \tag{7.1}$$

This is the number of particles moving in the lifetime T_{life} through the area $A^{\nu}_{\mathrm{eff}}(E_1, E_2)$. We choose the energy range $[E_1, E_2] = [10\ \mathrm{GeV}, 10^8\ \mathrm{GeV}]$, such that the contribution to the detectable event number from neutrinos with energies below E_1 or above E_2 is negligible for power-law spectra $\mathrm{d}\Phi^{\nu}_{\mathrm{model}}/\mathrm{d}E \propto E^{\gamma},\ -\gamma \gtrsim 1.5$. The effective area can be understood as the size of a perfect detector, detecting every single particle moving through its cross section and counting the same number of events as the real detector. Note that A^{ν}_{eff} depends on the assumed neutrino flux $\mathrm{d}\Phi^{\nu}_{\mathrm{model}}/\mathrm{d}E_{\nu}$, although this dependence is not apparent from the notation.

The effective area can be defined at different quality levels. At trigger level, the effective area is obtained if n_{sig} corresponds to all events triggering the detector in the time T_{life}. All effective areas in this work are calculated at the final analysis level, i.e. only events which fulfill all selection criteria are counted.

Integrating the flux limit (5.4) over $[E_1, E_2]$ and inserting (7.1) leads to

$$\int_{E_1}^{E_2} \frac{\mathrm{d}\Phi^{\nu,\mathrm{limit}}}{\mathrm{d}E_\nu} \mathrm{d}E_\nu = \frac{\mu^{90}(n_b, n_{\mathrm{obs}})}{A^\nu_{\mathrm{eff}}(E_1, E_2) T_{\mathrm{life}}}, \tag{7.2}$$

i.e. the integrated flux limit can easily be calculated from event upper limit, effective area and lifetime.

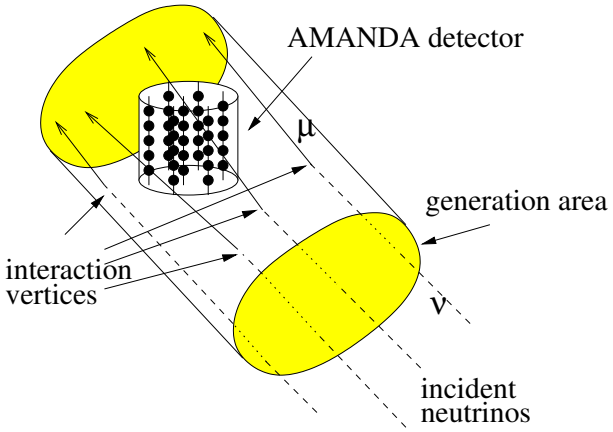

Figure 7.1: Geometry of event simulation. For a fixed direction θ of the incident neutrinos, interaction vertices are randomly distributed in the cylindrical generation volume. The cylinder height and the shaded generation area are chosen sufficiently large to cover all events that might trigger the detector.

The effective area is calculated using Monte Carlo simulations: for a certain zenith angle θ, neutrino interactions are simulated in a sufficiently large cylindrical volume as indicated in Fig. 7.1. A number n_{gen} of incident neutrino events simulated in the volume with generation area A_{gen} according to a spectrum $\mathrm{d}\Phi^\nu_{\mathrm{model}}/\mathrm{d}E$ corresponds to a simulated flux

$$\Phi^\nu_{\mathrm{model}} \equiv \int_{E_1}^{E_2} \frac{\mathrm{d}\Phi^\nu_{\mathrm{model}}}{\mathrm{d}E_\nu} \mathrm{d}E_\nu = \frac{n_{\mathrm{gen}}}{T_{\mathrm{life}} A_{\mathrm{gen}}}. \tag{7.3}$$

Inserting this into (7.1) results in

$$A^\nu_{\mathrm{eff}}(E_1, E_2) = A_{\mathrm{gen}} \frac{n_{\mathrm{sig}}}{n_{\mathrm{gen}}}, \tag{7.4}$$

i.e. the effective area is obtained by multiplying the generation area by the fraction of detected events (which trigger the detector and fulfill all selection criteria). The dependence of A^ν_{eff} on the declination is shown in Fig. 7.2 for different power-law spectra. At $\delta \lesssim 0^\circ$ (neutrinos coming from above the horizon), the effective area deteriorates, because background from downgoing muons requires strong quality cuts for a reasonable sensitivity. The

behavior at large declinations depends on the spectral index: for soft spectra, the effective area increases with the declination, since vertical muons can travel a larger distance through the instrumented volume than approximately horizontal muons. For harder spectra ($-\gamma \lesssim 2$), the absorption in the earth reduces the detectable neutrino flux significantly at large declinations.

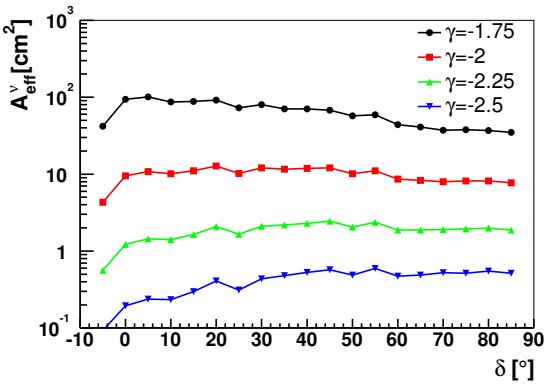

Figure 7.2: Neutrino effective areas averaged over the energy range $E_\nu = 10 \ldots 10^8$ GeV for neutrino spectra $\frac{\mathrm{d}\Phi^{\nu}_{\mathrm{model}}}{\mathrm{d}E_\nu} \propto E_\nu^{\gamma}$.

For the comparison with other point source analyses it should be mentioned that sometimes a factor ϵ_{bin} describing the loss of events due to the finite search bin size is separated from the effective area:

$$A_{\mathrm{eff}} = \epsilon_{\mathrm{bin}} A_{\mathrm{eff}}^{R\to\infty}. \tag{7.5}$$

$A_{\mathrm{eff}}^{R\to\infty}$ is the effective area for the application of quality cuts only (on $\mathcal{S}$, Q_{NN} and $\Delta\mathcal{L}$), if the the angular deviation of the reconstructed from the true event direction is not taken into account. The flux limits however are based on the detectable number of events *in the search bin*, which contains only $\epsilon_{\mathrm{bin}} \approx 80\%$ of all events passing the quality cuts. The efficiency ϵ_{bin} is shown in Fig. 7.3. The fluctuations are mainly caused by the changes of the bin size every 5° in declination (cf. Tab 6.3).

Muon effective area and flux limit

Although the main subject of this analysis is to measure neutrino fluxes, it is also interesting to investigate the neutrino induced muon fluxes which make the neutrino detection possible.

Equivalently to (7.1), the muon effective area is defined by:

$$n_{\mathrm{sig}}(E_1, E_2) = A^{\mu}_{\mathrm{eff}}(E_1, E_2) T_{\mathrm{life}} \int_{E_1}^{E_2} \frac{\mathrm{d}\Phi^{\mu}_{\mathrm{model}}}{\mathrm{d}E_\mu}(E_\mu)\mathrm{d}E_\mu. \tag{7.6}$$

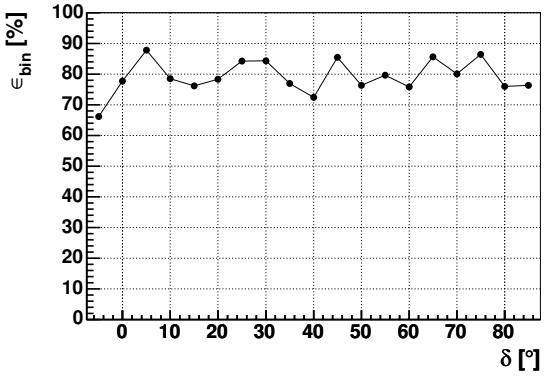

Figure 7.3: Bin reconstruction efficiency ϵ_{bin} as a function of the declination.

Since the muon energy decreases while the muon propagates from its production vertex to the detector, it has to be specified at which point the muon energy E_μ in (7.6) is to be measured. Here we use the muon energy E_{cdp} at the point of closest approach to the detector center, $\mathbf{x}_{\mathrm{cdp}}$. $\frac{\mathrm{d}\Phi^{\mu}_{\mathrm{model}}}{\mathrm{d}E_\mu}$ is the neutrino induced muon flux through a plane through the detector center perpendicular to the muon track.

The muon effective area is usually calculated for a given *neutrino* energy spectrum $\frac{\mathrm{d}\Phi^{\nu}_{\mathrm{model}}}{\mathrm{d}E_\nu}$. In this case, the muon energy spectrum has to be calculated from

- the initial neutrino spectrum,
- the probability $P_{\mathrm{abs}}(E_\nu)$ that a neutrino is absorbed in the earth before reaching the interaction volume,
- the probability $p^{\mu\to\nu}(E'_\mu; E_\nu)dE'_\mu$ that a muon of energy E'_μ is produced in the interaction volume, and
- the probability $p^{\mathrm{loss}}(E_\mu; E'_\mu, \mathbf{x}, \mathbf{x}_{\mathrm{cdp}})dE_\mu$ that a muon produced at the point $\mathbf{x}$ in the interaction volume[1] V loses the energy $E'_\mu - E_\mu$ while it propagates to $\mathbf{x}_{\mathrm{cdp}}$:

$$\begin{aligned}\frac{\mathrm{d}\Phi^{\mu}_{\mathrm{model}}}{\mathrm{d}E}(E_\mu) &= \int_0^\infty \frac{\mathrm{d}\Phi^{\nu}_{\mathrm{model}}}{\mathrm{d}E_\nu}(E_\nu)(1 - P_{\mathrm{abs}}(E_\nu)) \\ &\quad \int_0^{E_\nu} p^{\nu\to\mu}(E'_\mu; E_\nu) \\ &\quad \int_V p^{\mathrm{loss}}(E_\mu; E'_\mu, \mathbf{x}, \mathbf{x}_{\mathrm{cdp}})\mathrm{d}^3\mathbf{x}\mathrm{d}E'_\mu\mathrm{d}E_\nu\end{aligned}$$

[1] The interaction volume is not strictly defined. It should be sufficiently large to contain all production vertices of muons that might trigger the detector. On the other hand, its height should be small compared to the absorption length of neutrinos in the earth.

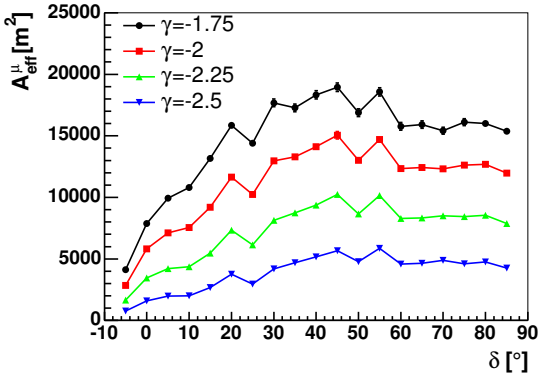

Figure 7.4: Muon effective areas for neutrino spectra $\frac{\mathrm{d}\Phi^{\nu}_{\rm model}}{\mathrm{d}E_{\nu}} \propto E_{\nu}^{\gamma}$, 10 GeV $< E_{\nu} < 10^8$ GeV.

In practice, the muon area is evaluated using Monte Carlo simulation of neutrino events similarly to (7.4):

$$A^{\mu}_{\rm eff}(E_1, E_2) = A_{\rm gen} \frac{n_{\rm sig}}{n^{\mu}_{\rm gen}}. \tag{7.7}$$

where $n^{\mu}_{\rm gen}$ is the number of muons originating from $n_{\rm gen}$ simulated neutrino events. For neutrino induced muon fluxes, the dependence of $A^{\mu}_{\rm eff}$ on the declination and spectral index is shown in Fig. 7.4. The effective area is practically averaged over muon energies from $m_{\mu}c^2 \approx 106$ MeV to 10^8 GeV, since due to the small muon range and negligible trigger efficiency for muons with an energy below 10 GeV mainly higher energetic muons contribute to $n_{\rm sig}$ and to the integrated muon flux at the detector[2]. With other words, the muon effective area does nearly not depend on the lower integration limit in (7.6), as long as this energy is below the threshold energy for muon detection, making this quantity suitable for the comparison of signal detection efficiencies between different detectors like Super-Kamiokande (threshold: about 1 GeV; effective area: 360-860 m^2 [Mat01] for an E^{-2} neutrino spectrum), MACRO (threshold: 1 GeV; effective area: up to 680 m^2 [Mon99]; $E^{-2.1}$ spectrum), and AMANDA-II (threshold: $\gtrsim$ 50 GeV; effective area: up to 15000 m^2; E^{-2} spectrum).

Having calculated a neutrino flux limit $\mathrm{d}\Phi^{\nu,\rm limit}/\mathrm{d}E$, we can derive a limit on the induced muon flux integrated over energy by equating the definitions of neutrino and muon effective area (7.1) and (7.6). Choosing $\mathrm{d}\Phi^{\nu}_{\rm model}/\mathrm{d}E \equiv \mathrm{d}\Phi^{\nu,\rm limit}/\mathrm{d}E$ (and correspondingly $\mathrm{d}\Phi^{\mu}_{\rm model}/\mathrm{d}E \equiv \mathrm{d}\Phi^{\mu,\rm limit}/\mathrm{d}E$ as the result-

[2] In contrast, the *neutrino* energy-averaged effective area does depend on the lower bound of the energy interval. If E_1 is below the detection threshold and $E_2 \gg E_1$, the definition (7.1) implies $A^{\nu}_{\rm eff}(E_1, E_2) \propto E_1^{-\gamma-1}$ for an assumed neutrino flux $\mathrm{d}\Phi^{\nu}/\mathrm{d}E \propto E^{\gamma}$.

ing muon flux) leads to

$$\int_{E_1}^{E_2} \frac{\mathrm{d}\Phi^{\mu,\mathrm{limit}}}{\mathrm{d}E}\mathrm{d}E = \frac{A^{\nu}_{\mathrm{eff}}(E_1,E_2)}{A^{\mu}_{\mathrm{eff}}(E_1,E_2)} \int_{E_1}^{E_2} \frac{\mathrm{d}\Phi^{\nu,\mathrm{limit}}}{\mathrm{d}E}\mathrm{d}E. \tag{7.8}$$

Monoenergetic effective area

The effective areas are strongly energy dependent. To understand the detector efficiency as a function of the neutrino or the muon energy, it is useful to calculate the effective areas $A^{\nu,\mu}_{\mathrm{eff}}(E) = \lim_{\Delta E \to 0} A^{\nu,\mu}_{\mathrm{eff}}(E, E+\Delta E)$. The distributions are shown in Fig. 7.5. The muon effective area reflects the combined trigger and reconstruction efficiency, while the neutrino effective area is also affected by the increase of the cross section (3.1) and of the muon range with energy. This results in the rise of the neutrino effective area by more than 5 orders of magnitude from $E_\nu = 10^2$ GeV to 10^5 GeV, but also in the decrease for $E_\nu > 10^5..10^6$ GeV for upward moving neutrinos ($\delta > 0°$) due to the neutrino absorption in the earth. The decrease of the muon effective area at energies $E_\mu > 10^5$ GeV is caused by inefficiencies in the event selection due to the production of high energy secondaries as discussed in section 6.6.2.

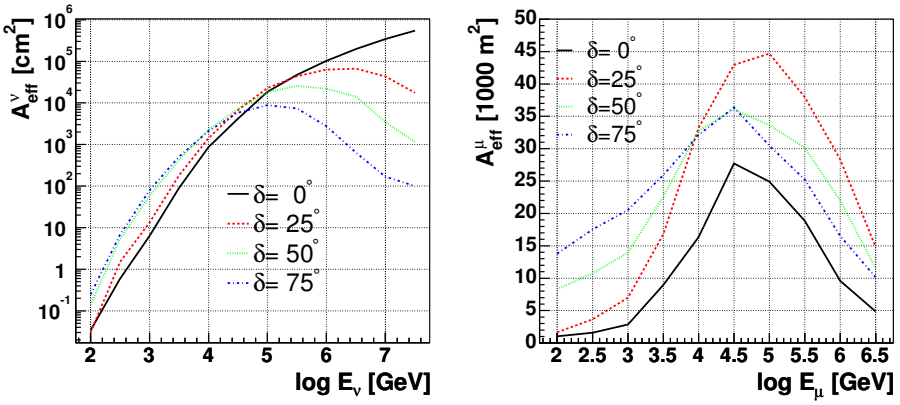

Figure 7.5: Effective neutrino and muon area as function of neutrino energy E_ν and muon energy $E_{\mu,\mathrm{cdp}}$ for different declinations δ.

.

Energy averaged effective areas for certain spectra $\mathrm{d}\Phi^{\nu,\mu}_{\mathrm{model}}/\mathrm{d}E$ can be calculated from the $A^{\nu,\mu}_{\mathrm{eff}}(E)$ distributions:

$$A^{\nu,\mu}_{\mathrm{eff}}(E_1,E_2) = \frac{\int_{E_1}^{E_2} A^{\nu,\mu}_{\mathrm{eff}}(E)\frac{\mathrm{d}\Phi^{\nu,\mu}}{\mathrm{d}E}\mathrm{d}E}{\int_{E_1}^{E_2} \frac{\mathrm{d}\Phi^{\nu,\mu}}{\mathrm{d}E}\mathrm{d}E}. \tag{7.9}$$

In this way one can derive flux limits for arbitrary spectra using the limits which will be presented in this work (for $\frac{\mathrm{d}\Phi^{\nu}_{\gamma=-2}}{\mathrm{d}E} \propto E^{-2}$). According to (7.2),

the flux limit for a neutrino spectrum $\frac{\mathrm{d}\Phi^{\nu}_{\mathrm{model}}}{\mathrm{d}E}$ integrated from E_1 to E_2 is

$$\int_{E_1}^{E_2} \frac{\mathrm{d}\Phi^{\mathrm{limit}}_{\mathrm{model}}}{\mathrm{d}E_\nu}\mathrm{d}E_\nu = \frac{A^{\gamma=-2}_{\mathrm{eff}}}{A^{\mathrm{model}}_{\mathrm{eff}}} \int_{E_1}^{E_2} \frac{\mathrm{d}\Phi^{\mathrm{limit}}_{\gamma=-2}}{\mathrm{d}E_\nu}\mathrm{d}E_\nu, \tag{7.10}$$

and correspondingly for muon flux limits.

This procedure has been explicitly carried out for power-law spectra with spectral indices from $\gamma = -1.5$ to -2.5. The effective area functions have been interpolated by piecewise power-law functions between the simulated energies, and linear interpolation in the declination was used. Compared to the limits calculated with continuously simulated neutrino energy spectra, the deviations are below 20%.

7.2 Angular resolution

Flux limits and detection probabilities which can be reached in a point source search depend on the deviation between the true and the reconstructed event direction: improving the resolution by a factor α (i.e. reducing the angular deviations $\Delta\psi$ on average by α) allows to use smaller search bins with the same signal detection efficiency as in the case of the worse resolution, but containing only a number of background events reduced by α^2.

As shown in Fig. 7.6, the angular resolution (defined here as the median of the $\Delta\psi$ distribution) after the final event selection ranges from about 1.5° to 2.5°. The improvement of the resolution at zenith angles $\theta \gtrsim 125°$ (declination $\delta \gtrsim 35°$) is caused by the cylindrical shape of the detector, involving on average longer muon track segments inside the detector for vertical compared to horizontal tracks. The reconstruction quality improves with the length of the muon track inside the detector, which is also reflected in the zenith dependence of the Q_{NN} variable: since the neural network has been designed to separate events with a small angular deviation between the true and the reconstructed event direction, the Q_{NN} variable takes larger values at $\delta \gtrsim 35°$. This leads to tighter cuts on this variables at $\delta \geq 35°$ compared to lower declinations $5° \leq \delta \leq 30°$ (cf. Tab. 6.3). The resolution deteriorates again at very large zenith angles $\theta \gtrsim 165°$. This is due to the fact that the hits from close to vertical events are often concentrated on one or two strings, especially if the muon track is located outside the instrumented volume. In this case, there is no unambiguous solution of the likelihood maximization, and the reconstructed track direction can depend on a few hits from scattered photons.

The resolution slightly improves with the spectral index, due to an increased number of hit OMs for high energy muon tracks. Only for hard spectra ($-\gamma \lesssim 1.8$), the increased contribution of delayed hits from highly energetic secondaries deteriorates the angular resolution.

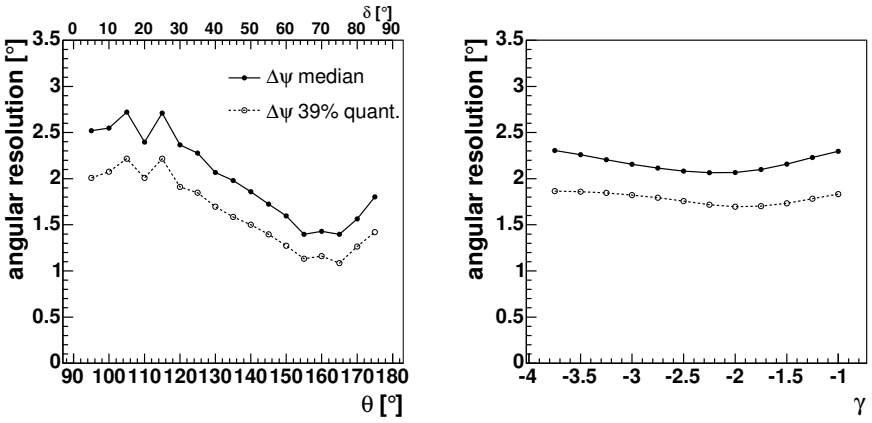

Figure 7.6: Angular resolution of the track reconstruction reconstruction after application of the final quality cuts. *Left:* The solid line shows the median of the $\Delta\psi$ distribution; the dashed line indicates the 39.3% quantile, which corresponds to the value $\sigma_{\Delta\psi}$ in the case of a (two dimensional) Gaussian distribution $\frac{\mathrm{d}N}{\mathrm{d}\Delta\psi} \propto \Delta\psi \cdot e^{-\frac{1}{2}\Delta\psi^2/\sigma^2_{\Delta\psi}}$. *Right:* Dependence of the angular resolution at $\delta = 40°$ (i.e. $\theta = 130°$) on the spectral index γ.

7.3 Energy distribution of the selected events

The energy dependent detection efficiency of the AMANDA detector for muons or neutrinos of a fixed energy is defined by the monoenergetic effective areas shown in Fig. 7.5. The energy distribution of the neutrinos which induce the detected muons can be directly obtained from the effective area for any initial neutrino spectrum $\mathrm{d}\Phi^\nu/\mathrm{d}E_\nu$:

$$\frac{\mathrm{d}N}{\mathrm{d}t\mathrm{d}E} = \frac{\mathrm{d}\Phi^\nu}{\mathrm{d}E_\nu}(E_\nu) A^\nu_{\mathrm{eff}}(E_\nu). \tag{7.11}$$

The neutrino induced *muon* energy spectrum can correspondingly be obtained by multiplying the muon effective area and the muon flux at the detector $\mathrm{d}\Phi^\mu/\mathrm{d}E_\mu$, which depends on the initial neutrino spectrum, neutrino absorption in the earth, the fraction of neutrino energy transferred to the muon and the muon energy loss between production vertex and the detector.

Muon energy distributions for different initial neutrino power-law spectra are shown in Fig. 7.7 for the events passing the selection criteria. The upper and lower "cutoff" (Fig. 7.7, right; defined by the energy range containing 90% of all accepted events induced by the assumed initial point source neutrino flux, with 5% below the lower cutoff) are due to the decrease of the neutrino flux with the energy and the drop of the detection efficiency for low energy muons. For a point source at $\delta = 40°$ emitting a neutrino flux $\mathrm{d}\Phi^\nu/\mathrm{d}E_\nu \propto E_\nu^{-2}$, the 90% interval ranges from 110 GeV to 85 TeV. The upper cutoff is shifted towards lower energies for softer neutrino spectra and

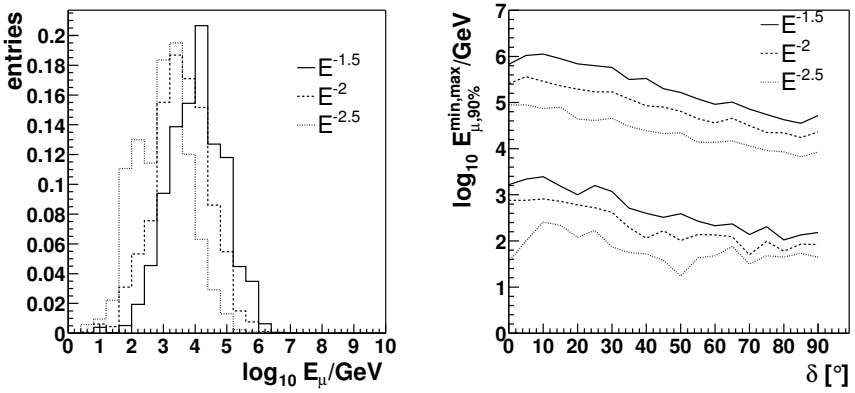

Figure 7.7: *Left:* Distribution of the muon energies (at the detector center) of the neutrino induced muons for a neutrino point source at $\delta = 40°$. The normalized distributions are shown for different spectral indices. *Right:* Muon energy range containing 90% of the events detected from a neutrino point source as a function of the declination.

– due to the neutrino absorption probability rising with energy – at higher declinations.

The distribution of the *neutrino* energies after selection cuts as well as the interval containing the neutrino energy of 90% of all accepted events caused by the assumed signal flux is shown in Fig. 7.8. This energy range is useful to estimate whether a certain predicted neutrino spectrum $\mathrm{d}\Phi^{\nu}_{\mathrm{model}}/\mathrm{d}E_{\nu}$, which does not strictly follow a power-law, is excluded by a limit $\mathrm{d}\Phi^{\nu,\mathrm{limit}}/\mathrm{d}E_{\nu} = c \cdot E_{\nu}^{\gamma}$ calculated for an assumed power-law spectrum: if for all energies in the 90%-interval the predicted flux is larger than the excluded power-law flux,

$$\frac{\mathrm{d}\Phi^{\nu}_{\mathrm{model}}}{\mathrm{d}E_{\nu}} \geq c \cdot E_{\nu}^{\gamma}, \tag{7.12}$$

then the predicted flux is excluded (unless $\mathrm{d}\Phi^{\nu}_{\mathrm{model}}/\mathrm{d}E_{\nu}$ is very close to $c \cdot E_{\nu}^{\gamma}$ in the 90% interval and $\mathrm{d}\Phi^{\nu}_{\mathrm{model}}/\mathrm{d}E_{\nu} \ll c \cdot E_{\nu}^{\gamma}$ outside the interval). In the opposite case ($\mathrm{d}\Phi^{\nu}_{\mathrm{model}}/\mathrm{d}E_{\nu} < c \cdot E_{\nu}^{\gamma}$ in the whole interval), the model is not excluded. If neither condition is fulfilled, one cannot judge without further information whether the model is excluded.

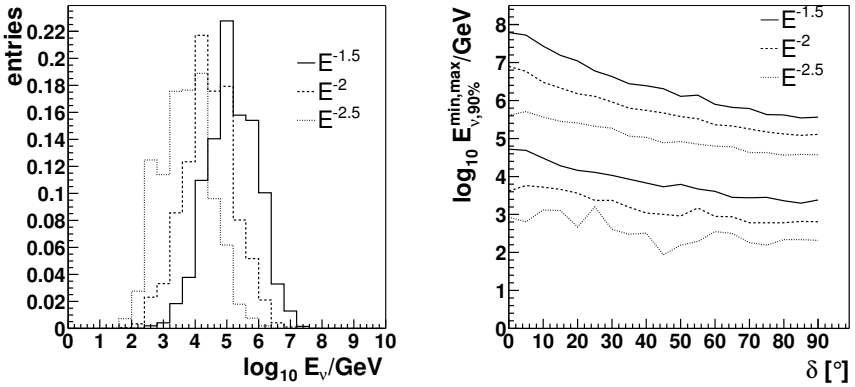

Figure 7.8: *Left:* Energy distribution of the detected neutrinos from a point source at declination $\delta = 40°$ for different power-law spectra. *Right:* Neutrino energy range containing 90% of the events detected from a point source as function of the declination.

Chapter 8

Results

8.1 Selected data sample

In chapter 6, we have described the selection and the optimization of quality cuts. Applying the quality cuts to the data sample recorded in the year 2000 yields a set of 1557 events with reconstructed zenith angles $\theta > 82.5°$. The distribution of the reconstructed event directions in equatorial coordinates is shown in Fig. 8.1. The chosen Hammer-Aithoff transformation ($\alpha' = 180° - \alpha \cdot 15°\mathrm{h}^{-1}$, $t = ((1 + \cos\delta\cos(\alpha'/2))/2)^{-1/2}$, $x = 2t\cos\delta\sin(\alpha'/2)$, $y = t\sin\delta$) is an equal-area projection, so that a significant contribution of events from a neutrino point source would be visible as an enhancement of the event density around the source position. The increasing event density above the horizon ($\delta < 0°$) is due to down-going atmospheric muons.

The atmospheric muon contribution is also visible at $\theta \lesssim 90°$ in Fig. 8.2,

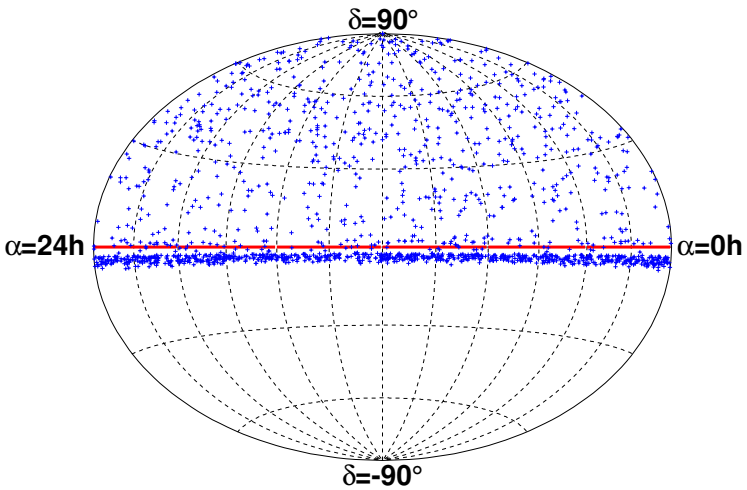

Figure 8.1: Distribution of the selected event sample in equatorial coordinates δ vs. α.

which shows the zenith spectrum of the selected events. The comparison to the expectation from simulated atmospheric neutrino events, scaled by the normalization factor 0.86 derived in section 6.6.1, shows a good agreement between the experimental data and the simulation at zenith angles $\theta \gtrsim 100°$ (Fig. 8.2).

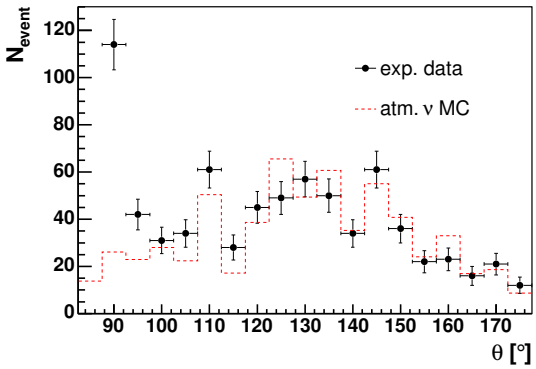

Figure 8.2: Zenith spectrum of the selected event sample. The dashed histogram indicates the expectation from atmospheric neutrinos, scaled by a factor 0.86 (cf. section 6.6.1).

The increased background from above the horizon makes it impossible to detect a weak neutrino point source in this region. Therefore, we restrict the further analysis to the declination range below the horizon, $\delta > 0°$. 699 events have been reconstructed in this range. This reduced sample, consisting mainly of upward moving atmospheric neutrinos, is searched for excesses from certain directions, i.e. clusters in the (α, δ) distribution. We present different approaches to this task in the following sections. Anticipating the result, no significant excess has been found. This leads to the calculation of flux limits, that restrict the possible flux of neutrinos from certain directions at a 90% confidence level.

8.2 Preselected source candidates

The most obvious way to search for point sources of neutrinos is the selection of a list of astrophysical objects for which detectable neutrino fluxes are predicted or at least expected under certain conditions.

For this analysis, we have selected 30 sources listed in Tab. 8.1 from the classes of astrophysical objects described in chapter 2, according to the following criteria:

- Five blazars, which have been confirmed as TeV γ-ray sources (two

Candidate	α [h]	δ [°]	$n_{\rm obs}$	n_b	μ^{90}	$\Phi_\mu^{\rm lim}$	$E^2\frac{{\rm d}\Phi_\nu^{\rm lim}}{{\rm d}E}$	$\Phi_\mu^{\rm prev}$
TeV Blazars								
Markarian 421	11.07	38.2	3	1.50	7.55 (5.92)	3.2	3.7	3.2^C
Markarian 501	16.90	39.8	1	1.57	3.24 (2.85)	1.3	1.6	6.5^C
1ES 1426+428	14.48	42.7	1	1.62	3.20 (2.81)	1.3	1.6	1.0^C
1ES 2344+514	23.78	51.7	1	1.23	3.52 (3.13)	1.5	2.0	6.4^C
1ES 1959+650	20.00	65.1	0	0.93	2.02 (1.64)	1.0	1.4	1.7^C
GeV Blazars								
QSO 0528+134	5.52	13.4	1	1.09	3.64 (3.26)	2.5	2.0	8.6^C
QSO 0235+164	2.62	16.6	1	1.49	3.30 (2.91)	2.0	1.7	4.8^C
QSO 1611+343	16.24	34.4	0	1.29	1.83 (1.44)	0.8	0.9	14^C
QSO 1633+382	16.59	38.2	1	1.50	3.29 (2.90)	1.4	1.6	5.8^B
QSO 0219+428	2.38	42.9	1	1.63	3.19 (2.80)	1.3	1.6	6.6^A
QSO 0954+556	9.87	55.0	1	1.66	3.17 (2.78)	1.3	1.7	
QSO 0716+714	7.36	71.3	2	0.74	6.36 (5.17)	3.1	4.8	
Microquasars								
SS433	19.20	5.0	0	2.38	1.27 (1.23)	1.0	0.7	6.7^M
GRS 1915+105	19.25	10.9	1	0.91	4.20 (3.44)	3.2	2.4	6.5^C
GRO J0422+32	4.36	32.9	2	1.31	5.79 (4.60)	2.8	3.1	2.0^C
Cygnus X-1	19.97	35.2	2	1.34	5.76 (4.57)	2.5	2.9	3.9^C
Cygnus X-3	20.54	41.0	3	1.69	6.96 (5.73)	2.9	3.4	4.0^C
XTE J1118+480	11.30	48.0	1	0.92	4.09 (3.43)	1.8	2.3	1.7^C
CI Cam	4.33	56.0	0	1.72	1.60 (1.22)	0.6	0.9	1.4^B
LS I +61 303	2.68	61.2	0	0.75	2.12 (1.75)	1.0	1.5	4.3^C
SNR and pulsars								
SGR 1900+14	19.12	9.3	0	0.97	2.00 (1.62)	1.6	1.2	9.9^C
Geminga	6.57	17.9	3	1.78	6.87 (5.64)	3.8	3.3	9.1^A
Crab Nebula	5.58	22.0	2	1.76	4.94 (4.15)	2.6	2.5	4.1^K
Cassiopeia A	23.39	58.8	0	1.01	1.98 (1.60)	0.9	1.3	6.9^C
Miscellaneous								
3EG J0450+1105	4.82	11.4	2	0.89	6.21 (5.02)	4.6	3.5	24^B
M 87	12.51	12.4	0	0.95	2.01 (1.63)	1.4	1.1	6.3^K
UHE CR Triplet	1.28	20.4	2	1.84	4.86 (4.07)	2.5	2.3	50^B
NGC 1275	3.33	41.5	1	1.72	3.12 (2.73)	1.3	1.5	8.5^B
J2032+4131	20.54	41.5	3	1.72	6.93 (5.70)	2.8	3.4	
UHE CR Triplet	12.32	56.9	1	1.48	3.31 (2.92)	1.4	1.9	1.4^B

Table 8.1: 90% upper limits on neutrino flux and (neutrino induced) muon flux limits for 30 candidate sources, calculated for assumed neutrino spectra ${\rm d}\Phi^\nu/{\rm d}E \propto E^{-2}$. Also listed are the number $n_{\rm obs}$ of events observed in the search bins, the number n_b of expected background events in the bin, and the upper limit μ^{90} on the number of signal events in the search bin (in brackets: systematics not included). Differential neutrino flux limits on $E^2 \cdot {\rm d}\Phi/{\rm d}E$ are listed in units 10^{-7} GeV cm^{-2} s^{-1}, (integral) muon flux limits in units 10^{-15} cm^{-2} s^{-1}. The last column contains the best muon flux limits from previous analyses (same units as $\Phi_\mu^{\rm lim}$); the superscript indicates the experiment: A [A$^+$03c], B [Bir02]: AMANDA-B10 (1997); C [Con03]: AMANDA-B10 (1999); K: Super-Kamiokande; M: MACRO. Since [A$^+$03c] and [Bir02] are based on the same data set from the year 1997 using different event selections, we list the limits from [A$^+$03c] by default, and values from [Bir02] are only considered if for a specific source no limit is published in [A$^+$03c].

unconfirmed TeV γ-ray emitting AGNs, 3C 66A=QSO 0219+428 and M87, are also contained in the selected source candidates),

- seven GeV emitting blazars [NS02],
- eight galactic X-ray binaries classified as microquasars,
- four galactic supernova remnants and pulsars,
- the six individually selected source candidates listed in section 2.6.

The extent of this list has been chosen as a compromise between minimizing the probability of overlooking a possible neutrino source and at the same time maximizing the overall significance of a possible detection, which decreases with the number of trials.

For each neutrino source candidate, we place a circular bin with optimized radius as listed in table 6.3 around the source position. The number n_{obs} of events observed in the bin as well as the number n_b of background events estimated from the number of observed events per declination band according to equation (5.2) are listed in Tab. 8.1. The evaluation of observed versus expected event numbers makes use of an "excess parameter" ξ, calculated for each neutrino source candidate:

$$\xi \equiv -\log_{10} P_{\mathrm{binom}}(\geq n_{\mathrm{obs}} | n_{\mathrm{band}}, f_{\mathrm{bin}}), \tag{8.1}$$

where $f_{\mathrm{bin}} = \frac{n_b}{n_{\mathrm{band}}}$, given by (5.2), is the fraction of the search bin area divided by the area of the declination band of width $2R_{\mathrm{bin}}$ around the source declination δ_0, n_{band} is the total number of observed events in this band, and $P_{\mathrm{binom}}(\geq k|n,f) = \sum_{i=k}^{\infty} \left(\begin{array}{c} n \\ i \end{array} \right) f^i (1-f)^{n-i}$ is the binomial probability of observing at least k out of n events inside the search bin if the events are uniformly distributed within the declination band, i.e. if each event has a probability f to be reconstructed inside the search bin.

The calculation of excess parameters is equivalent to the usually stated n_σ significances: an excess of n_σ standard deviations means a chance probability $P = 10^{-\xi} = \frac{1}{2} - \frac{1}{2}\mathrm{erf}(n_\sigma/\sqrt{2})$ of obtaining at least the observed number of events in the absence of a signal. In this work, we only specify the excess parameter ξ to describe single-bin probabilities.

The ξ distribution for the 30 source candidates is shown in Fig. 8.3. For the evaluation of the significance of the largest excess, the same distribution is calculated for 10000 randomized data sets with the right ascension values of the selected 699 events replaced by random values. Similarly to the background estimation by averaging over declination bands, this results in simulated data sets with the same zenith distribution as the real data, but events from any possibly contained point source are scrambled in right ascension. The comparison of the true and the simulated excess parameters allows us to calculate the overall probability that the largest observed excess parameter is due to a fluctuation of background events. The largest

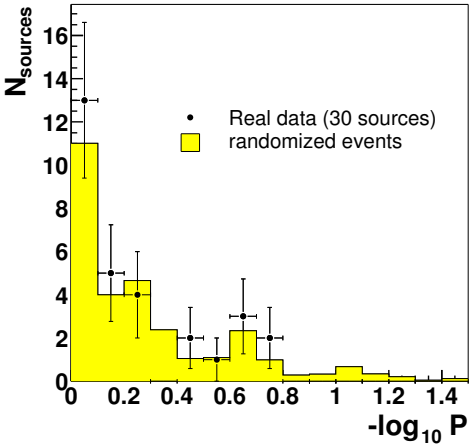

Figure 8.3: Distribution of the excess parameter $\xi = -\log_{10} P$ for the observed data as well as simulated event sets with randomized right ascension values. The distribution decreases roughly exponentially with ξ. Due to the small average number of about 1–2 events per search bin, the discrete values of ξ cause deviations from the exponential decrease.

excess parameter $\xi \approx 0.77 \approx -\log_{10}(0.17)$ has been obtained for the GeV Blazar QSO 0716+714. The simulation of randomized event samples reveals a probability of 60% of observing at least this value in any of the 30 search bins as a random fluctuation of only background events. Therefore, there is no indication of a significant source among the selected candidates.

Having found no significant excess, we calculate flux limits for each of the source candidates. The differential neutrino flux limits[1] and the integral muon flux limits for an assumed spectrum $\mathrm{d}\Phi_\nu/\mathrm{d}E \propto E^{-2}$ are listed in Tab. 8.1. These values have been calculated according to (5.4) from the numbers n_{obs} and n_b (defining the upper limit μ^{90} on the number of signal events, also listed in the table) and n_{sig} (for an assumed flux $\mathrm{d}\Phi_\nu/\mathrm{d}E = 10^{-6}\ \mathrm{GeV cm^{-2} s^{-1}} \cdot E^{-2}$, obtained from the simulation of point sources producing this flux); muon flux limits have been calculated using (7.8). The limits include systematic uncertainties as described in section 5.1.1.

For comparison, the best previously published limits on neutrino induced muon fluxes are also shown in the table (last column). These results were ob-

[1] Other experiments as well as previous AMANDA point source analyses published *integrated* neutrino flux limits. However, the integral neutrino fluxes depend on the integration range, so that we prefer to state differential neutrino flux limits. Integral neutrino flux limits (e.g. above $E_\nu = 10$ GeV) can be easily calculated: $\int_{10\ \mathrm{GeV}}^{\infty} \mathrm{d}\Phi_\nu/\mathrm{d}E\mathrm{d}E = (10\ \mathrm{GeV})^{-1}(E^2\mathrm{d}\Phi_\nu/\mathrm{d}E)$ for an assumed E^{-2} spectrum.

tained with the MACRO [A+01c] and the Super-Kamiokande [Mat01] experiment as well as in point source analyses of data obtained in the years 1997 and 1999 with the 10-string AMANDA-B10 sub-detector [A+03c, Bir02, Con03]. Only muon flux limits are listed, because – in contrast to neutrino flux limits – they are only weakly dependent on the energy threshold. The MACRO flux limits are derived under the assumption of an initial neutrino flux $\mathrm{d}\Phi^{\nu}/\mathrm{d}E \propto E^{-2.1}$ in contrast to the E^{-2} spectrum assumed in the Super-Kamiokande and AMANDA analyses and can therefore not be directly compared to the limits for an E^{-2} spectrum listed in the table. Neutrino induced muon flux limits derived with AMANDA-II for an $E^{-2.1}$ spectrum are approximately 15% worse than for an E^{-2} spectrum.

Fig. 8.4 shows the declination dependence of the limits on neutrino induced muon fluxes for different experiments. Due to the location of the other detectors in the Northern hemisphere, the flux limits obtained by IMB, MACRO and Super-Kamiokande improve towards negative declinations. The AMANDA-II sensitivity improves significantly from $\delta = -5°$ to $+5°$ and slightly at higher declinations. The flux limits derived with data recorded during one year of operation with the AMANDA-II detector are currently the best flux limits on neutrino point sources at positive declinations.

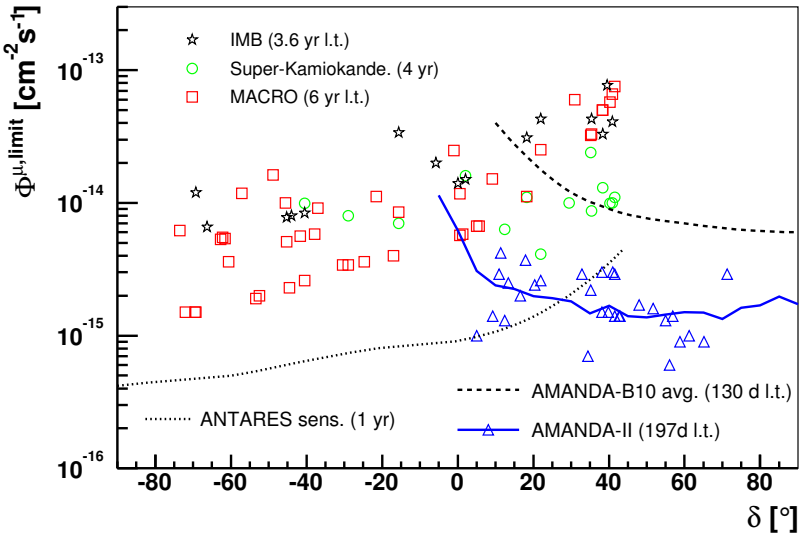

Figure 8.4: Muon flux limits and sensitivities at 90% CL vs. source declination obtained with different experiments. The flux limits are derived assuming E^{-2} neutrino spectra, except for the MACRO results which are based on $E^{-2.1}$ spectra. Limits obtained in the presented AMANDA-II analysis of 197 days lifetime (l.t.) are shown by the triangles, the average sensitivity by the solid curve; the dashed curve shows the sensitivity of the AMANDA-B10 sub-detector after 130 days lifetime, and the sensitivity of the ANTARES experiment [Mon03] expected after 365 days of data taking is given by the dotted curve. The results of IMB, Super-Kamiokande or MACRO were obtained after more than three years of detector operation.

8.3 Search for unexpected neutrino sources

No significant source has been detected among the 30 selected source candidates. However, a neutrino source might have been overlooked due to the restricted number of sources in the list, or an unexpected ("hidden") source of astrophysical neutrinos might exist in a direction from where no other high energy particles have been detected.

Therefore, we also perform a binned search looking for clusters of events from any direction, which need not coincide with a known source of high energy charged particles or γ-rays. This method is applied to the complete Northern hemisphere $\delta > 0°$. "Candidate sources" are placed on a grid with an approximate distance of 1° between adjacent grid points, resulting in overlapping circular search bins. Compared to previous searches for neutrino point sources with AMANDA (e.g. [Bir02, You01, Con03]), two details have been changed: in those analyses, a system of *rectangular* bins was defined, which was shifted by *half* the bin size in both dimensions (right ascension α and declination δ). In the current work, events are counted in *circular* bins around the grid points, and the shift between the single points is *small* compared to the bin radius. The angular distance of 1° between the grid points and the zenith-dependent bin radii from 2.6° to 4.6° correspond to $N_{\text{shift}} \approx 5 \ldots 9$ with the denotation of chapter 5.

Circular bins have the advantage of containing a larger fraction of the signal (assuming there is a source in the center of the bin). The smaller distance of grid points improves the detection probability. As demonstrated in section 5.3, the rising probability for the observation of a large background fluctuation in one of the search bins only partly compensates the increase of the detection probability.

In principle, this search in the whole Northern hemisphere is identical to the method of investigating selected source candidates as described in the previous section. Only the background estimation and the calculation of chance probabilities has to be adapted at high declinations: the highest declination of the preselected sources is 71.3°. At this declination, the fraction of the search bin solid angle compared to the declination band is still small, so that the background estimation (5.2) can be used. At higher declinations however, the search bins cover a substantial fraction of the declination band. At $\delta = 85°$, this fraction reaches 17%, so that in the presence of a neutrino point source the number of background events would be overestimated. This would lead to an underestimation of the signal flux and therefore to the calculation of too low excess parameters and flux limits. This problem can be avoided by estimating the background event density close to $\delta = 90°$ from a region at lower declination ($75° < \delta < 85°$). This yields a background density of 205 events/sr, i.e. 2.27 events per search bin of radius 3.4°. Varying the range of the declination interval leads to slightly larger background estimates by up to about 10%. Therefore, flux

limits calculated assuming 2.27 background events per bin are conservative.

The different way of background estimation also implies a changed definition of the excess parameter, since the binomial probability (8.1) is not appropriate if the number of events in the declination band might be dominated by events from the search bin. At declinations $\delta > 85°$, we define the excess parameter via Poissonian probabilities:

$$\xi \equiv -\log_{10} P_{\text{Poisson}}(\geq n_{\text{obs}}|\langle n_{\text{bg}}\rangle) \tag{8.2}$$

$$= -\log_{10} \sum_{i=n_{\text{obs}}}^{\infty} \frac{\langle n_{\text{bg}}\rangle^i e^{-\langle n_{\text{bg}}\rangle}}{i!}, \tag{8.3}$$

where $\langle n_{\text{bg}}\rangle = 2.27$ is the estimated average event number per search bin.

The excess parameters are shown in Fig. 8.5 as a function of the search bin position in equatorial coordinates (α, δ). Excess parameters $\xi \geq 2.4$ are present at four distinct positions (separated by at least 3° in space angle), listed in Tab. 8.2.

In a similar way as for the preselected source candidates, we evaluate the overall probability to obtain these excess parameters as fluctuations of background in absence of a point source by simulating event sets with randomized right ascension coordinates. Fig. 8.6 shows the comparison of the excess parameter distribution as observed in the experimental data and expected in the case of the simulated event sets. For each of the simulated event sets ($i_{\text{sim}} = 1...N_{\text{sim}}^{\text{total}}$, $N_{\text{sim}}^{\text{total}} = 40000$), we register the four most significant excesses $\xi_l^{i_{\text{sim}}}$, $l = 1..4$. We define that a simulated event set i_{sim}

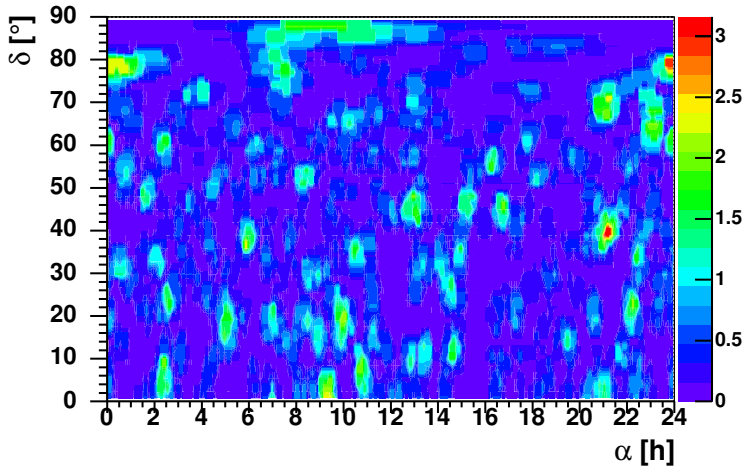

Figure 8.5: Excess parameter $\xi = -\log_{10} P$ as a function of the direction in equatorial coordinates. The values of ξ are defined by the color scale to the right.

Level l	ξ_l	$\alpha[h]$	$\delta[^\circ]$	$P_l^{\rm sim}$
1	3.16	21.1	37.9	40%
2	2.97	23.8	77.9	20%
3	2.46	21.2	69.9	19%
4	2.40	9.3	0.2	17%

Table 8.2: Positions and probabilities of the four most significant excesses. $P_l^{\rm sim}$ (calculated with simulated event samples) is the probability of observing a background fluctuation with at least the significance observed in the experimental data at level l.

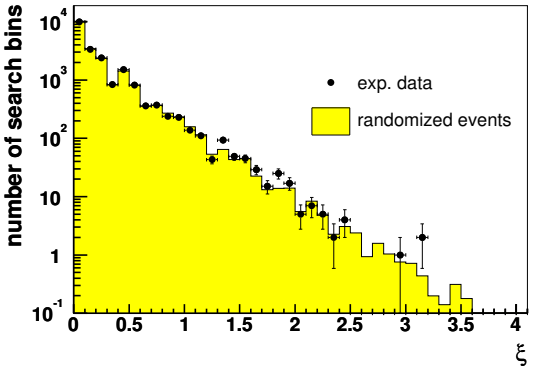

Figure 8.6: Distribution of the excess parameter ξ measured in the overlapping search bins covering the Northern hemisphere. The shaded histogram shows the expectation in absence of point sources, obtained by randomizing the right ascension coordinates of all events.

has a higher significance than the observed event set at level l, if at levels $1 \ldots l$ the excess parameters in the simulation are larger than the excess parameters in the observed data:

$$\xi_{l'}^{i_{\rm sim}} > \xi_{l'}^{\rm data},\ l' = 1...l \tag{8.4}$$

Counting the numbers $N_{\rm sim}^l$ of simulated events sets with higher significance than the observed data, we calculate the probabilities $P_l^{\rm sim} = N_{\rm sim}^l / N_{\rm sim}^{\rm total}$ that the observed excess parameters occur as a fluctuation of background event densities. This is a generalization of the evaluation of the probability for the most significant excess which was done for the preselected sources: if there are a few neutrino point sources each contributing too few events for a significant detection, the combined contribution might still be significant. The probability for a fluctuation with an excess parameter of 3.16 (the most significant single excess observed in the experimental data) or higher in any of the search bins is 40% (cf. Tab. 8.2 and Fig. 8.7). If we extend the list to

the 10 most significant excesses ($\xi_{10}^{\mathrm{data}} = 2.05$), the probability that fluctuations with at least the significances as observed in the experimental data occur is still $P_{10}^{\mathrm{sim}} = 8\%$. This means that there is no significant evidence for a contribution of one or a few neutrino point sources in the data; the observed distribution of event numbers as a function of right ascension and declination is compatible with a uniform distribution in the right ascension.

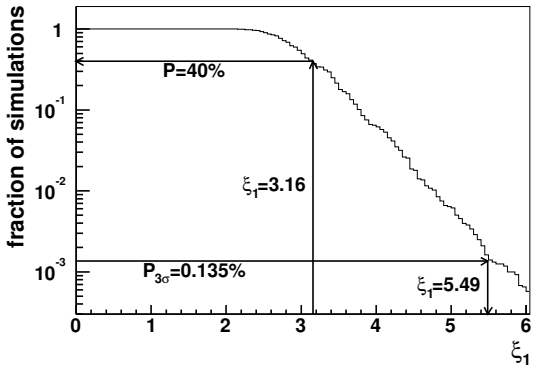

Figure 8.7: Fraction of background simulations with a maximum excess parameter $\geq \xi_1$ in any of the search bins, obtained by the simulation of 40000 event sets with randomized right ascension values. This distribution allows us to estimate the probability that a bin with excess parameter $\xi = 3.16$ as observed in the real data set occurs as a random fluctuation of statistically distributed background events. The distribution also determines the excess parameter which is necessary for a 3 sigma detection.

We calculate neutrino flux limits for an assumed spectrum $\mathrm{d}\Phi_\nu/\mathrm{d}E \propto E^{-2}$ in the same way as for the preselected source candidates by considering each grid point as a candidate source. The only difference is that we do not include the effect of systematic uncertainties in this limit calculation. This results in the neutrino flux limit map of the Northern sky shown in Fig. 8.8. As expected, local maxima of the flux limits occur approximately at positions where we observe the highest excess parameters. However, due to the increasing neutrino absorption in the earth at large declinations, the worst limits of about $8 \cdot 10^{-7}$ GeV cm^{-2} s^{-1} are obtained at $\delta \gtrsim 80°$, while the neutrino flux limit at the position of the largest excess parameter ($\alpha = 21.1$ h, $\delta = 38°$) is $6.5 \cdot 10^{-7}$ GeV cm^{-2} s^{-1}.

Finally, we estimate the neutrino flux level which is necessary for a significant detection. We call a detection "significant" if the overall probability to reach the detection criterion in absence of a neutrino point source is $P_{3\sigma} = 0.135\%$, corresponding to a 3 sigma detection. As demonstrated in Fig. 8.7, in a fraction $P_{3\sigma}$ of 40000 background simulations (event samples with randomized right ascensions) an excess parameter $\xi \geq 5.49$ occurs in any of the overlapping search bins. In order to estimate the point source flux

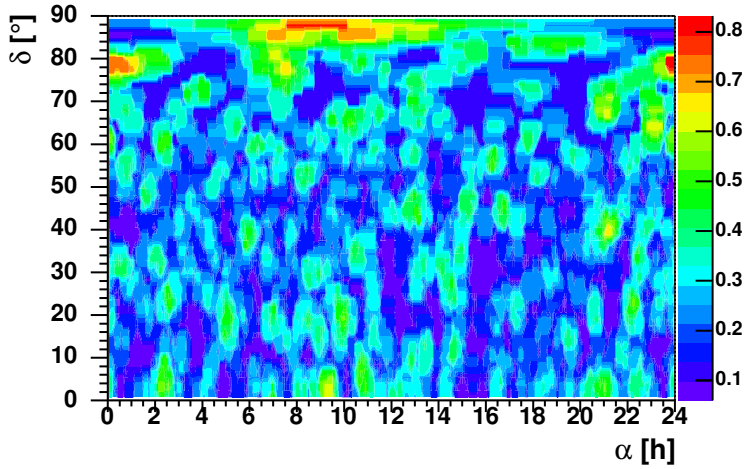

Figure 8.8: Neutrino flux limits at 90% confidence level as a function of the hypothetical source position in equatorial coordinates. The limits on $E^2 \cdot \frac{\mathrm{d}\Phi}{\mathrm{d}E}$ have been calculated under the assumption of an E^{-2} neutrino spectrum, in units of 10^{-6} GeV cm^{-2} s^{-1}. In this figure the effect of systematic uncertainties has not been included in the limit calculation, in contrast to the limits listed in Tab. 8.1 for selected source candidates.

for a 3 sigma detection with e.g. 50% probability, we calculate the signal contribution $\langle n_s \rangle$ to the number of events reconstructed in the search bin, which would result in a 3 sigma detection probability of at least 50%:

$$P_{\mathrm{det}} = \sum_{n_b=0}^{\infty} \sum_{n_s=n_{\mathrm{obs}}^{\mathrm{min}}(\langle n_b \rangle)-n_b}^{\infty} P_{\langle n_b \rangle}(n_b) P_{\langle n_s \rangle}(n_s) \overset{!}{>} 0.5. \tag{8.5}$$

The mean number of background events per bin is $\langle n_b \rangle \approx 0.8...2.2$ (cf. Tab. 6.3); $P_\mu(k) = \mu^k e^{-k}/k!$ are Poissonian probabilities, and $n_{\mathrm{obs}}^{\mathrm{min}}(\langle n_b \rangle)$ is the number of events per search bin which would result in a 3 sigma detection, i.e. which would lead to $\xi \geq 5.49$. If we approximate the binomial probabilities in (8.1) by Poisson probabilities, this number $n_{\mathrm{obs}}^{\mathrm{min}}(\langle n_b \rangle)$ is defined by

$$\sum_{k=n_{\mathrm{obs}}^{\mathrm{min}}(\langle n_b \rangle)}^{\infty} P_{\langle n_b \rangle}(k) \leq 10^{-5.49}. \tag{8.6}$$

The required mean signal contribution ranges from $\langle n_s \rangle = 6.9$ events (if the mean background in the search bin is $\langle n_b \rangle = 0.8$) to $\langle n_s \rangle = 10.5$ events (in the case of $\langle n_b \rangle = 2.2$). Assuming an E^{-2} signal spectrum, the expected number of events detected in the search bin from a point source emitting a flux $\mathrm{d}\Phi^\nu/\mathrm{d}E = E^{-2} \cdot 10^{-6}$ GeV cm^{-2} s^{-1} is between $n_{\mathrm{sig}} \approx 13$ at $\delta \approx 90^\circ$ and $n_{\mathrm{sig}} \approx 20$ at low declinations (cf. Tab. 6.3). Therefore,

the necessary neutrino flux level for a 3 sigma detection ranges from about $4 \cdot 10^{-7}$ GeV cm^{-2} s^{-1} (at $\delta = 15°$) to $8 \cdot 10^{-7}$ GeV cm^{-2} s^{-1} (at $\delta = 85°$).

8.4 Limits for different spectra

In the previous sections, neutrino flux limits have been calculated under the assumption of an initial neutrino spectrum $\frac{\mathrm{d}\Phi_\nu}{\mathrm{d}E} \propto E^{-2}$. As explained in section 2.1, this spectrum is expected in the case of the acceleration of particles at strong shock fronts ($M \gg 1$). Here we investigate the flux limits for power law spectra with spectral indices deviating from the generic value $\gamma = -2$, as well as limits based on flux predictions for a specific class of sources, the blazars emitting GeV γ-rays [NS02].

We calculate flux sensitivities for different spectra according to (5.5) via the model rejection factor (6.26), which is the ratio of the event upper limit $\langle \mu^{90}(n_b) \rangle$ (independent of the assumed neutrino spectrum) to the expected number of detected events n_{sig} for an (arbitrarily normalized) assumed neutrino flux. Flux limits are correspondingly obtained, if $\langle \mu^{90}(n_b) \rangle$ is replaced by $\mu^{90}(n_b, n_{\mathrm{obs}})$. n_{sig} is directly obtained from a sample of simulated neutrino events taking into account energy-dependent weight factors.

Fig. 8.9 shows sensitivities for different assumptions on the neutrino energy spectrum: different power law spectra and the neutrino flux from GeV blazars[2] predicted in [NS02]. A presentation of flux limits for all candidate sources and a series of different flux assumptions would go beyond the scope of this work, but the figure allows to draw conclusions for the estimation of flux limits for different spectra: in the case of power law spectra with indices $-\gamma = -2... - 2.75$, the lines indicating the flux sensitivities for a fixed declination, but different spectral indices, approximately intersect in one point. If the detectable neutrinos originated from a small energy interval around a most probable energy $\hat{E_\nu}$, which does not depend on γ, the intersection would occur at this energy. As shown in Fig. 7.8, the neutrino energy distribution extends over a few decades, and is shifted towards higher energies for harder spectra or lower declinations. Therefore, $\hat{E_\nu}$ is not well defined, but we can still define a declination-dependent "intersection energy", listed in Tab. 8.3. At this energy, the flux limits and sensitivities deviate by at most 30% from the corresponding values for $\gamma = -2$, so that flux limits can be calculated for any spectral index between -2 and -2.75.

While the shown sensitivities for power law spectra depend only weakly on the declination, sensitivities for the predicted GeV blazar spectrum (thin curve peaking at 10^8 GeV) get worse by two orders of magnitude from low

[2] The predicted neutrino flux in the GeV blazar model depends on different parameters like opening angle of the cone in which high energy neutrinos are emitted and the maximum energy E_p to which protons are accelerated, which produce the neutrinos. The figure shows the prediction for the most optimistic case of a collimation of the neutrino flux within 1°, and $E_p \approx 10^{19}$ eV.

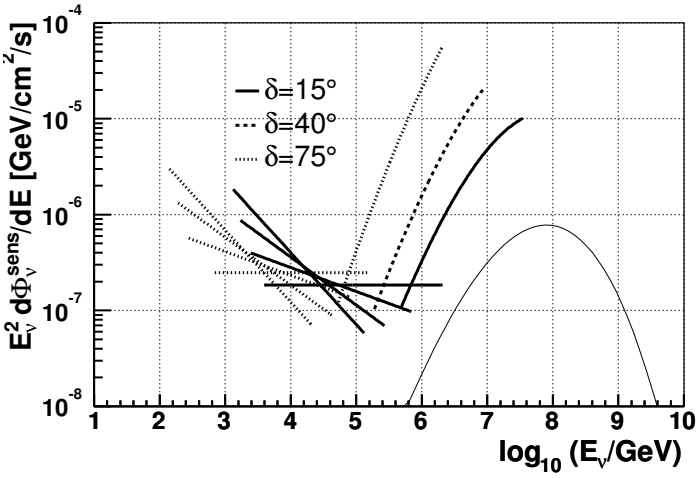

Figure 8.9: Neutrino sensitivities (multiplied by E_ν^2) vs. neutrino energy for different spectral shapes and different declinations. Shown are the sensitivities for four different power law spectra $-\gamma = 2, 2.25, 2.5, 2.75$, indicated by the straight lines at neutrino energies from approximately 10^2 to 10^6 GeV – the horizontal lines represent $\gamma = -2$, the most steeply falling lines represent $\gamma = -2.75$. The power-law sensitivities are only shown for $\delta = 15°$ and $\delta = 75°$. Sensitivities on predicted neutrino fluxes from GeV blazars are indicated by the curves from 10^5 to $10^{7.5}$ GeV. The thin curve peaking at 10^8 GeV is the predicted GeV blazar neutrino flux. Curves are drawn in the energy range which contains 90% of the detectable events.

Declination [°]	0–15	20–30	35–40	45–90
Intersection energy [TeV]	30	20	10	5

Table 8.3: Neutrino energy, at which differential neutrino flux limits for power law spectra with indices from $\gamma = -2$ to -2.75 deviate by $< 30\%$ from the limit for $\gamma = -2$, in dependence of the source declination.

($\delta = 15°$) to high ($\delta = 75°$) declinations. This is due to the absorption of high energy neutrinos in the earth, which increases with the zenith angle and therefore reduces the detectable flux from neutrino point sources at large declinations emitting hard spectra. The model rejection factor at $\delta = 15°$, which is approximately the lowest declination of GeV blazars in the source catalog, is about 15, i.e. the sensitivity would need to be improved by more than one order of magnitude to probe this model. It should be mentioned, that we obtained this result with an event selection optimized for an assumed E^{-2} neutrino spectrum. For the E^{-2} spectrum, neutrinos with energies below 2.5 PeV contribute 90% of the detectable events (at $\delta = 15°$), while 90% of the detectable muons from a GeV blazar with the predicted

spectrum would originate from neutrinos with 0.6 PeV $< E_\nu <$ 40 PeV. A cut optimization for the high energy spectrum slightly improves the average expected model rejection factor to 12.4.

For the blazar Markarian 501, the neutrino flux limit has been calculated for a spectral shape $\mathrm{d}\Phi_\nu/\mathrm{d}E \propto E^{-1.8}$ [A$^+$04a, Ste04], an approximation to the intrinsic γ-ray spectrum of the source (corrected for IR absorption [JS02]) from 500 GeV to 20 TeV, during the flare in 1997. The neutrino flux limit is approximately 30–50% below the intrinsic γ-ray flux, at energies $E_{\nu,\gamma} \lesssim 10$ TeV. Although the neutrino flux limit is calculated under the assumption that the neutrino power-law spectrum continues beyond 20 TeV and that the high state persists for approximately one year, the comparison shows that the AMANDA-II sensitivity is approaching a neutrino flux level close to realistic γ-ray fluxes.

Finally we note that in section 7.1 we described an alternative procedure of calculating neutrino flux limits for arbitrary spectral shapes. This allows the calculation of the expected event numbers n_{sig} for different assumed neutrino fluxes by scaling the flux limits with the energy averaged effective area (cf. equation 7.10). The necessary information is contained in Fig. 7.5 showing neutrino effective areas as a function of neutrino energy, so that this procedure can be carried out if no simulated neutrino event samples are available.

8.5 Angular correlations

Even if no single source emits a flux of neutrinos sufficiently strong for a significant detection, it might be possible to observe a combined effect from several weak neutrino sources by an unexpectedly large number of reconstructed event pairs separated by small space angles.

The analysis of angular correlations has been originally proposed in [Pee73] for the investigation of source catalogs in view of a clustering of extragalactic objects. A two-point correlation function $w(\psi)$ is defined by

$$n(\psi)d\psi \equiv n_{\mathrm{rand}}(\psi)(1 + w(\psi))d\psi, \tag{8.7}$$

where $n(\psi)d\psi$ is the average number of sources in the catalog separated from a randomly chosen source by an angular distance between ψ and $\psi + d\psi$. $n_{\mathrm{rand}}(\psi)$ is the corresponding distribution which is expected if all sources are independently and isotropically distributed. A clustering of the objects at small angles ψ_{corr} would be indicated by values $w(\psi)$ significantly larger than zero for $\psi \approx \psi_{\mathrm{corr}}$.

This method can be applied to the neutrino analysis by treating the events in the selected data sample as objects in the catalog (not to be confused with the list of 30 neutrino source candidates). If we observe a significant clustering of these events in equatorial coordinates at separation angles comparable

to the angular resolution, this is an indication for the existence of one or more astrophysical sources emitting neutrinos. The number of contributing sources and their positions would remain unknown. Only if one or a few sources were sufficiently strong, their positions would be evident in a two-dimensional histogram of reconstructed event directions, where each event is weighted with the number of near neighbors (e.g. separated by less than 6° in space angle).

Instead of $n(\psi)$, we use the cumulative number[3]

$$N(\psi) \equiv \sum_{i=1}^{N_\nu} \sum_{j=i+1, \psi_{ij}<\psi}^{N_\nu} 1 \tag{8.8}$$

of event pairs separated by a space angle of less than ψ. N_ν is the total number of neutrino event candidates in the selected event sample. We obtain the background distribution $N_{\mathrm{rand}}(\psi)$ in the usual way by creating a large number N_{bg} of event sets with right ascension coordinates of each event replaced by random values. By this method the created background samples have the same declination distribution as the observed data; events from any astrophysical neutrino source possibly contained in the original event sample are spread over 24 h in the right ascension. Therefore, we can use the background samples to estimate the background distribution $N_{\mathrm{rand}}(\psi)$ as the average of the distributions $N_{k,\mathrm{bg}}(\psi)$ (defined by (8.8), calculated for the randomized event samples $k = 1..N_{\mathrm{bg}}$):

$$N_{\mathrm{rand}}(\psi) \equiv \frac{1}{N_{\mathrm{bg}}} \sum_{k=1}^{N_{\mathrm{bg}}} N_{k,\mathrm{bg}}(\psi). \tag{8.9}$$

We exclude the region $\delta > 85°$ from this analysis of angular correlations, because close to vertical events would not be sufficiently separated by the randomization. Furthermore, events at low declination $\delta < 5°$ are excluded. Otherwise, a small number of event pairs with small separation angles at medium declination might become insignificant due to the increasing event density close to the horizon.

The correlation function

$$W(\psi) = N(\psi)/N_{\mathrm{rand}}(\psi) - 1 \tag{8.10}$$

for the observed 594 events in the restricted declination range is shown in Fig. 8.10. For the estimation of the significance, the shaded area indicates for each ψ bin the range of $W(\psi)$ values covered by 68% of the randomized event sets. The observed correlation function is compatible with the hypothesis of uncorrelated event directions.

[3] The relation between $n(\psi)$ and $N(\psi)$ is: $N(\psi) = \frac{N_\nu}{2} \int_0^\psi n(\psi')d\psi'$.

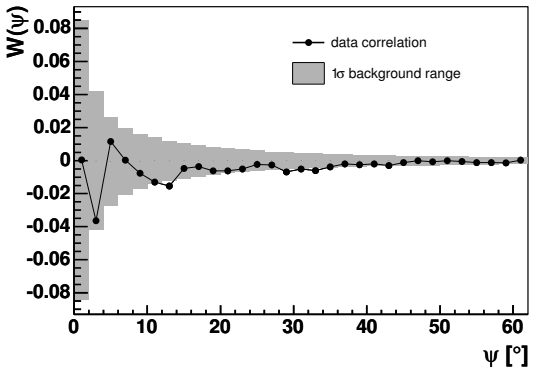

Figure 8.10: Correlation function, obtained by comparing the number of event pairs separated by a space angle less than ψ to the number of pairs expected from randomized event sets. The correlation function $W(\psi)$ is calculated also for each randomized event set. The shaded area shows for each ψ bin the range of $W(\psi)$ covered by 68% of all randomized event sets.

Which number n_{src} of sources would be necessary for a significant deviation from $W(\psi) \approx 0$, assuming each source contributes a number n_{ev} of events to the final data sample? To answer this question, we replace $n_{\mathrm{src}} \cdot n_{\mathrm{ev}}$ events in the experimental data set by events from simulated sources. The sources are simulated at random positions from $\delta = 5°$ to $85°$, and n_{ev} events per source are randomly added according to a Gaussian distribution with standard deviation $2.1°$, which is approximately the 39% quantile of the angular mismatch between true and reconstructed event direction at $\delta < 30°$ (cf. Fig. 7.6). For each parameter pair (n_{src}, n_{ev}) we create 50 event sets with the same number, but different random positions of the simulated source events. Additionally, 10000 event sets with randomized right ascension values are created for each "signal enriched" data set in the same way as for the pure experimental data set. These randomized samples are used to assign a significance as a function of ψ to each non-randomized data set depending on its correlation function $W(\psi)$: if a fraction P of all 10000 randomized event sets has higher values $W(\psi)$ than the value obtained for the non-randomized data set, the n_σ significance is given by (5.6).

The significance distribution of the 50 data sets is shown (by the filled circles) in Fig. 8.11 as a function of ψ for $n_{\mathrm{src}} = 5$ and $n_{\mathrm{ev}} = 5$. The mean significance increases with ψ up to a few times the angular resolution ($2.1°$) and decreases again at large separation angles $\psi \gtrsim 6°$.

Since only an average significance of 1.2 sigma can be reached by the default method, we try to improve this method by making use of the expected different energy spectrum of background and signal events. In section 6.5.4 we showed that flux limits can only be improved by up to 8% if we apply a

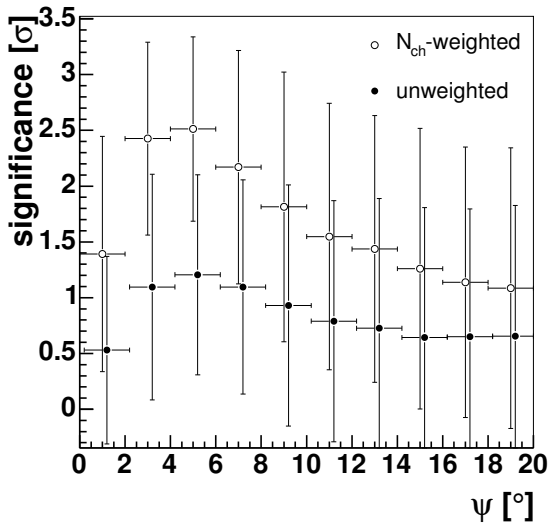

Figure 8.11: Significance distribution of correlation values $W(\psi)$ calculated in 50 event sets. The vertical error bars show the RMS of the significances. For each event set, 25 events are exchanged by signal events from 5 simulated sources. As an alternative to the default "unweighted" method (filled circles), an $N_{\rm ch}$-dependent weight (described in the text below) has been assigned to each event, resulting in the significances shown by the open circles. In both cases, we calculate significances for number of event pairs separated by $2^\circ, 4^\circ, ...$ and show the unweighted results slightly displaced.

cut on the number of hit optical modules, $N_{\rm ch}$. Nevertheless, a significant improvement can be expected for the investigation of the correlation function, because the number of event pairs scales with the *squared* number of selected events. Instead of rejecting all events below a certain $N_{\rm ch}$ value, we assign weights

$$p(N_{\rm ch}) \equiv \begin{cases} 0 & \text{if } N_{\rm ch} < 7 \\ 1 & \text{if } N_{\rm ch} > 92 \\ (N_{\rm ch} - 7)/86 & \text{if } 7 \leq N_{\rm ch} \leq 92 \end{cases} \tag{8.11}$$

to each event. This weight function is obtained by comparing the $N_{\rm ch}$ distributions $\mathrm{d}N^{\rm data,signal}/\mathrm{d}N_{\rm ch}$ for experimental data (mainly atmospheric neutrinos, restricted to $\delta > 5^\circ$) and for a simulated signal following an E^{-2} spectrum (isotropic at $\delta > 5^\circ$). $p(N_{\rm ch})$ is a rough approximation to the ratio $\frac{\mathrm{d}N^{\rm signal}/\mathrm{d}N_{\rm ch}}{\mathrm{d}N^{\rm signal}/\mathrm{d}N_{\rm ch}+\mathrm{d}N^{\rm data}/\mathrm{d}N_{\rm ch}}$, after normalization of both the data and the signal distributions to the same number of entries.

We change the definition of $N(\psi)$ to

$$N(\psi) \equiv \sum_{i=1}^{N_\nu} \sum_{j=i+1,\psi_{ij}<\psi}^{N_\nu} p(N_{\mathrm{ch},i})p(N_{\mathrm{ch},j}), \tag{8.12}$$

and perform the same procedure of simulating signal and background distributions as described above, with the only difference of assigning to each added signal event an N_{ch} value randomly chosen according to the $\mathrm{d}N^{\mathrm{signal}}/\mathrm{d}N_{\mathrm{ch}}$ distribution and using N_{ch}-dependent weights for the calculation of $N(\psi)$. The significances of the obtained $W(\psi)$ values are shown (by the empty circles) in Fig. 8.11. The suppressed contribution of low-N_{ch} event pairs to $N(\psi)$ increases the average significance from about 1.2 σ to 2.5 σ. The correlation function for the observed data without added signal events, calculated with N_{ch}-dependent weights, is shown in Fig. 8.12. Also with the improved method no significantly large correlation can be observed.

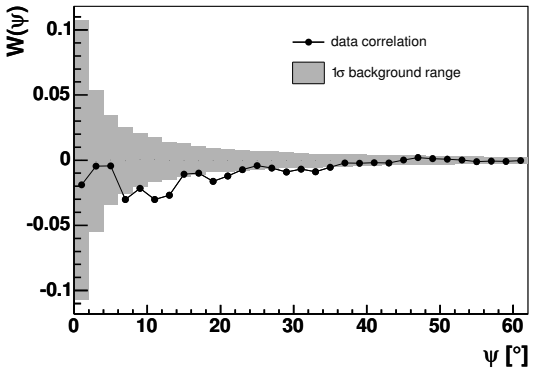

Figure 8.12: Correlation function, calculated with N_{ch}-dependent event weights. Except for the weighting, this figure has been obtained in the same way as Fig. 8.10.

Assuming that a certain number n_{src} of neutrino point sources exists, each of which produces the same number of detectable events, we estimate the number of events n_{ev} per source in dependence of the number of sources, which is necessary for a 3 sigma detection with 50% probability: for each parameter pair $(n_{\mathrm{src}}, n_{\mathrm{ev}})$ we determine the angle ψ, at which we expect the largest significance (e.g. for $n_{\mathrm{src}} = 5$, $n_{\mathrm{ev}} = 5$: $\psi = 6°$, as shown in Fig. 8.11). The detection probability P_{det} is the fraction of simulated signal enriched event sets, for which the significance at this angle is at least 3 sigma. The parameter pairs resulting in $P_{\mathrm{det}} > 50\%$ are listed in Tab. 8.4. Compared to the contribution of 7–10.5 signal events from a single source[4], which would be necessary for a 3 sigma detection in the binned search, the

[4]In the case of a single source, we estimated the required *mean* of the (Poissonian)

n_{src}	4	5	6	7	8	9	10
n_{ev}	6	6	5	5	5	4	4
P_{det} [%]	68	68	68	72	90	52	62

Table 8.4: 3 sigma detection probabilities P_{det} for $n_{\mathrm{src}} = 4...10$ sources each contributing n_{ev} detected events. n_{ev} has been chosen so that $P_{\mathrm{det}} \geq 50\%$.

required number of detectable events per source is reduced to 6 (in the case of at least $n_{\mathrm{src}} = 4$ sources) or 4 if $n_{\mathrm{src}} \geq 9$.

In principle, we can also calculate neutrino flux limits for a set of $n_{\mathrm{src}} = 2, 3, 4, ...$ equally strong astrophysical neutrino point sources. Although similar neutrino luminosities might be expected for a certain class of objects, the detectable fluxes depend on the distances of the sources from the earth. Therefore, we do not want to carry the angular correlation analysis too far. We end with the conclusion that – using a larger data sample – it might be possible with the presented method to prove the existence of astrophysical neutrino point sources even if no single source can be significantly detected.

number of signal events contributing to the search bin. However, if we make the simplified assumption of a *constant* signal contribution as in the angular correlation analysis, also 7–11 events from a single source are needed. Note that, due to the finite search bin size, this number is smaller by approximately 20% compared to the total necessary number of detected signal events.

Chapter 9

Summary

We analyzed the AMANDA-II data recorded in the year 2000 with the aim of detecting astrophysical point sources of high energy muon-neutrinos or specifying as low as possible flux limits.

Within a detector lifetime of 197 days, $1.3 \cdot 10^9$ events triggered the detector. This event sample, consisting mainly of down-going atmospheric muon events, was reduced by applying cuts on reconstructed zenith angles to less than 1% with a significantly increased portion of upward moving atmospheric neutrinos. The reduced event sample is still dominated by misreconstructed down-going muon events. Well reconstructed upward moving neutrino induced muons can be identified by a number of observables calculated for each event. A multi-dimensional zenith-dependent selection cut, based on an artificial neural network, resulted in a final sample of 699 events reconstructed as up-going. It is strongly dominated by atmospheric neutrino events.

We optimized the tightness of the cuts for best average limits on astrophysical neutrino point source fluxes, i.e. for a high passing rate of high energy up-going neutrino events and for an efficient rejection of misreconstructed atmospheric muon events. This optimization was performed independently of observed event rates around single source candidates, but only based on observed event numbers averaged over large solid angles. Thereby we excluded a bias of the cuts due to possible signal indications and guaranteed the "blindness" of the optimization procedure. A comparison to atmospheric neutrino simulation revealed that the rate and the zenith spectrum of the events coming from at least 10° below the horizon are in good agreement with the expectation of atmospheric neutrinos, which constitute an inevitable background for the neutrino point source search.

We applied different methods in order to search for enhancements of events from a certain direction in the final data sample, which would indicate the presence of astrophysical neutrino point sources. No significant source was detected among the candidates from a catalog of 30 astrophysical objects

which possibly emit high energy neutrinos. Flux limits were specified with an average of about $E^2 \mathrm{d}\Phi_\nu^{\mathrm{limit}}/\mathrm{d}E = 2{\cdot}10^{-7}$ GeV cm^{-2} s^{-1}. These are currently the best neutrino flux limits for point-like objects at positive declinations, and the AMANDA-II sensitivity is close to certain flux predictions, e.g. for the microquasar SS433. However, one should notice that due to downward fluctuations of the observed number of events compared to the background expectation (e.g. in the case of SS433, we observed 0 events compared to 2.48 expected events), flux limits for single candidate sources are better than the sensitivity.

Extending the method to the whole Northern hemisphere resulted in a sky map of neutrino flux limits.

Finally, we investigated correlations of the reconstructed event directions in order to possibly detect a combined signal from a small number of weak neutrino sources. In the analyzed data set, we did not find an indication of an unexpectedly large number of event pairs separated by small angles.

Outlook

This analysis was based on the first year of data recorded with the completed AMANDA-II detector. In the meantime, the detector has been running for more than four years. The operation of the detector improved from year to year, i.e. the number of functioning optical modules could be increased, and the normal data taking time per year increased from 248 days in 2000 to $\geq$276 days per year since 2002. Based on the selection technique presented in this work, the enlarged data sample might reveal the first sources of high energy neutrino emission. Conservatively assuming the same detector performance and the same lifetime of 197 d per year, we expect an improvement of the sensitivity by a factor of approximately 2.6–2.9 for the combined data set of four years. In absence of sufficiently strong neutrino sources, we may therefore expect a considerable improvement of the average flux limit and the confirmation of flux limits, which are lower than the current sensitivity due to downward fluctuations.

A further significant improvement of the sensitivity to neutrino point sources is expected with the future Icecube detector [A$^+$04b], planned to be deployed from 2005 to 2010. With a volume of about 1 km^3 instrumented with 4800 photomultipliers, this detector is expected to reach a sensitivity of $\mathrm{d}\Phi_\nu^{\mathrm{sens.}}/\mathrm{d}E \approx E^{-2} \cdot 5.5 \cdot 10^{-9}$ GeV cm^{-2} s^{-1} after one year of operation.

Bibliography

[A+99] Apollonio, M. *et al.*, Limits on neutrino oscillations from the CHOOZ experiment, *Phys. Lett. B* **466**:415 (1999).

[A+01a] Aharonian, F. *et al.*, Evidence for TeV gamma ray emission from Cassiopeia A, *Astron. Astrophys.* **370**:112 (2001).

[A+01b] Ahmad, Q. R. *et al.*, Measurement of the Rate of $\nu_e + d \rightarrow p + p + e^-$ Interactions Produced by ^{8}B Solar Neutrinos at the Sudbury Neutrino Observatory, *Phys. Rev. Lett.* **87**:071301 (2001).

[A+01c] Ambrosio, M. *et al.*, Neutrino Astronomy with the MACRO Detector, *Astrophys. J.* **546**:1038 (2001).

[A+02] Aharonian, F. *et al.*, An unidentified TeV source in the vicinity of Cygnus OB2, *Astron. Astrophys.* **393**:L37 (2002).

[A+03a] Aharonian, F. *et al.*, Is the Giant Radio Galaxy M87 a TeV Gamma-Ray Emitter?, *Astron. Astrophys.* **403**:L1 (2003).

[A+03b] Ahrens, J. *et al.*, Limits on diffuse fluxes of high energy extraterrestrial neutrinos with the AMANDA-B10 detector, *Phys. Rev. Lett.* **90**:251101 (2003).

[A+03c] Ahrens, J. *et al.*, Search for Point Sources of High Energy Neutrinos with AMANDA, *Astrophys. J.* **583**:1040 (2003).

[A+04a] Ahrens, J. *et al.*, Search for extraterrestrial point sources of neutrinos with AMANDA-II, *Phys. Rev. Lett.* **92**:071102 (2004).

[A+04b] Ahrens, J. *et al.*, Sensitivity of the IceCube detector to astrophysical sources of high energy muon neutrinos, *Astropart. Phys.* **20**:507 (2004).

[AATV00] Atoyan, A. M., *et al.*, On the gamma-ray fluxes expected from Cassiopeia A, *Astron. Astrophys.* **355**:211 (2000).

[AC03] AMANDA-Collaboration, Siegmund documentation (2003), URL `http://amanda.wisc.edu/software/siegmund/`.

[AJJ00] Athar, H., Jezabek, M., and Jasuda, O., Effects of neutrino mixing on high-energy cosmic neutrino flux, *Phys. Rev. D* **62**:103007 (2000).

[B+03a] Balkanov, V. *et al.*, The BAIKAL neutrino project: status report, *Nucl. Phys. B (Proc. Suppl.)* **118**:363 (2003).

[B+03b] Butt, Y. M. *et al.*, Chandra/Very Large Array Follow-up of TeV J2032+4131, the Only Unidentified TeV Gamma-Ray Source, *Astrophys. J.* **597**:494 (2003).

[BD02] Boettcher, M. and Dermer, C. D., An Evolutionary Scenario for Blazar Unification, *Astrophys. J.* **564**:86 (2002).

[Bir00] Biron, A., Reconstruction Uncertainties due to Time Calibration Errors, AMANDA Internal Report 20001101 (2000).

[Bir02] Biron von Curland, A., Search for Atmospheric Muon-Neutrinos and Extraterrestric Neutrino Point Sources in the 1997 AMANDA-B10 Data, Ph.D. thesis, Humboldt-Universität zu Berlin (2002).

[Boe02] Boeser, Sebastian, Separation of atmospheric neutrinos with the AMANDA-II detector, Diploma thesis, Technische Universität München, Germany (2002).

[BP97] Bednarek, W. and Protheroe, R. J., Gamma Rays and Neutrinos from the Crab Nebula Produced by Pulsar Accelerated Nuclei, *Phys. Rev. Lett.* **79**:2616 (1997).

[BPV03] Berezhko, E., Pühlhofer, G., and Völk, H., Gamma-ray emission from Cassiopeia A produced by accelerated cosmic rays, *Astron. Astrophys.* **400**:971 (2003).

[BZ77] Blandford, R. D. and Znajek, R. L., Electromagnetic Extraction of Energy from Kerr Black Holes, *Mon. Not. Roy. Astron. Soc.* 433 (1977).

[C+03a] Chirkin, D. *et al.*, New Techniques: Muon Glaciology (2003), URL `http://amanda.berkeley.edu/~dima/work/BKP/DCS/ICE_FLOW/poster.ps.gz`, poster contribution at the annual AGU meeting.

[C+03b] Conrad, J. *et al.*, Including systematic uncertainties in confidence interval construction for Poisson statistics, *Phys. Rev. D* **67**:012002 (2003).

[CH01] Cowen, D. and Hanson, K., Time Calibration of the AMANDA Neutrino Telescope with Cosmic Ray Muons, in [HKS01], 1133, Hamburg, Germany (2001).

[CO96] Carroll, B. W. and Ostlie, D. A., An Introduction to Modern Astrophysics, Addison-Wesley, Reading, Massachusetts, USA (1996).

[Con03] Conrad, J., A Search for Neutrinos from Cosmic Point Sources using AMANDA-B10 with Emphasis on Limit Calculation Techniques, Ph.D. thesis, Uppsala University, Sweden (2003).

[CS03] Cooley-Sekula, J. A., Searching for High Energy Neutrinos with the AMANDA-II Detector, Ph.D. thesis, University of Wisconsin - Madison (2003).

[D+02] Distefano, C. *et al.*, Neutrino Flux Predictions for Known Galactic Microquasars, *Astrophys. J.* **575**:378 (2002).

[DS93] Dermer, C. D. and Schlickeiser, R., Model for the high-energy emission from blazars, *Astrophys. J.* **416**:458 (1993).

[E+03] Eguchi, K. *et al.*, First Results from KamLAND: Evidence for Reactor Antineutrino Disappearance, *Phys. Rev. Lett.* **90**:021802 (2003).

[F+98] Fukuda, Y. *et al.*, Evidence for oscillation of atmospheric neutrinos, *Phys. Rev. Lett.* **81**:1562 (1998).

[F+02] Fukuda, S. *et al.*, Determination of solar neutrino oscillation parameters using 1496 days of Super-Kamiokande-I data, *Phys. Lett. B* **539**:179 (2002).

[F+03] Feser, T. *et al.*, Online Search for Neutrino Bursts from Supernovae with the AMANDA Detector, in [K+03], 1325 (2003).

[FC98] Feldman, G. J. and Cousins, R. D., A Unified Approach to the Classical Statistical Analysis of Small Signals, *Phys. Rev. D* **57**:3873 (1998).

[Fer49] Fermi, E., On the Origin of the Cosmic Radiation, *Phys. Rev.* **75**:1169 (1949).

[G+98] Gandhi, R. *et al.*, Neutrino interations at ultrahigh energies, *Phys. Rev. D* **58**:093009 (1998).

[Gai90] Gaisser, T. K., Cosmic Rays and Particle Physics, Cambridge University Press, New York, USA (1990).

[Gee02] Geenen, H., Energy reconstruction and spectral unfolding of atmospheric leptons with the AMANDA detector, Diploma thesis, Bergische Universität Wuppertal (2002).

[GH02] Gaisser, T. K. and Honda, M., Flux of Atmospheric Neutrinos, *Annu. Rev. Nucl. Part. Sci.* **52**:153 (2002).

[GK03] Gazizov, A. and Kowalski, M. P., High Energy Neutrino Generator for Neutrino Telescopes, in [K$^+$03], 1459 (2003).

[H$^+$98] Heck, D. *et al.*, CORSIKA: A Monte Carlo code to simulate extensive air showers, Wissenschaftlicher Bericht FZKA 6019, Forschungszentrum Karlsruhe (1998).

[H$^+$99] Hartman, R. C. *et al.*, The Third EGRET Catalog of High-Energy Gamma-Ray Sources, *Astrophys. J. Suppl. Ser.* **123**:79 (1999).

[H$^+$02] Hagiwara, K. *et al.*, Review of Particle Physics, *Phys. Rev. D* **66**:010001 (2002), URL `http://pdg.lbl.gov`.

[Hau02] Hauschildt, T., 2000 Data filtering (2002), URL `http://amanda.wisc.edu/software/filter00/`.

[Hil96] Hill, G. C., Experimental and Theoretical Aspects of High Energy Neutrino Astrophysics, Ph.D. thesis, University of Adelaide, Australia (1996).

[Hil01] Hill, G. C., Bayesian event reconstruction and background rejection in neutrino detectors, in [HKS01], 1279 (2001).

[Hil03] Hill, G. C., Comment on "Including Systematic Uncertainties in Confidence Interval Construction for Poisson Statistics", *Phys. Rev. D* **67**:118101 (2003).

[HKS01] Heinzelmann, G., Kampert, K.-H., and Spiering, C. (eds.), Proceedings of the 27^{th} International Cosmic Ray Conference, Hamburg, Germany (2001).

[HP98] He, Y. D. and Price, P. B., Remote sensing of dust in deep ice at the South Pole, *Journal of Geophysical Research* **103**:17041 (1998).

[Hun99] Hundertmark, S., AMASIM Neutrino Detector Simulation Program, in C. Spiering (ed.), Proceedings of Workshop on Simulation and Analysis Methods for Large Neutrino Telescopes, 276, Zeuthen, Germany (1999), DESY-Proc-1999-01.

[Jac96] Jackson, J. D., Classical Electrodynamics, Wiley, New York, USA, 3rd edition (1996).

[JKG96] Jungman, G., Kamionkowski, M., and Griest, K., Supersymmetric dark matter, *Phys. Rep.* **267**:195 (1996).

[JS02] de Jager, O. C. and Stecker, F. W., Extragalactic Gamma-Ray Absorption and the Intrinsic Spectrum of Markarian 501 during the 1997 Flare, *Astrophys. J.* **566**:738 (2002).

[K+99] Kouveliotou, C. *et al.*, Discovery of a Magnetar Associated with the Soft Gamma Repeater SGR 1900+14, *Astrophys. J.* **510**:L115 (1999).

[K+03] Kajita, T. *et al.* (eds.), Proceedings of the 28^{th} International Cosmic Ray Conference, Tsukuba, Japan (2003).

[Kar99] Karle, A., Monte Carlo Simulation of Photon Transport and Detection in Deep Ice: Muons and Cascade, in C. Spiering (ed.), Proceedings of Workshop on Simulation and Analysis Methods for Large Neutrino Telescopes, 174, Zeuthen, Germany (1999), DESY-Proc-1999-01.

[Kow04] Kowalski, M. P., Search for Neutrino-Induced Cascades with the AMANDA-II Detector, Ph.D. thesis, Humboldt-Universität zu Berlin (2004).

[Leu01] Leuthold, M. J., Search for Cosmic High Energy Neutrinos with the AMANDA-B10 Detector, Ph.D. thesis, Humboldt-Universität zu Berlin (2001).

[Lip93] Lipari, P., Lepton spectra in the earth's atmosphere, *Astropart. Phys.* **1**:195 (1993).

[LM00] Learned, J. and Mannheim, K., High-Energy Neutrino Astrophysics, *Ann. Rev. Nucl. Part. Sci.* **50**:679 (2000).

[LS91] Lipari, P. and Stanev, T., Propagation of multi-TeV muons, *Phys. Rev. D* **44**:3543 (1991).

[LW01] Levinson, A. and Waxman, E., Probing Microquasars with TeV Neutrinos, *Phys. Rev. Lett.* **87**:1101 (2001).

[M+79] Margon, B. *et al.*, The Bizarre Spectrum of SS 433, *Astrophys. J. Lett.* **230**:L41 (1979).

[Man93] Mannheim, K., γ rays and neutrinos from a powerful cosmic accelerator, *Phys. Rev. D* **48**:2408 (1993).

[Mat01] Matsuno, S., A search for astronomical neutrino sources with the Super-Kamiokande detector, in [HKS01], 1065 (2001).

[Mon99] Montaruli, T., MACRO as a Telescope for Neutrino Astronomy, in D. Kieda, M. Salamon, and B. Dingus (eds.), Proceedings of the 26^{th} International Cosmic Ray Conference, 213 (1999).

[Mon03] Montaruli, T., High Energy Neutrino Astrophysics (2003), arXive:astro-ph/0312558.

[MR93] Meszaros, P. and Rees, M. J., Relativistic fireballs and their impact on external matter - Models for cosmological gamma-ray bursts, *Astrophys. J.* **405**:278 (1993).

[N$^+$02] Neronov, A. *et al.*, Large-Scale Extragalactic Jets Powered by Very-High-Energy Gamma Rays, *Phys. Rev. Lett.* **89**:051101 (2002).

[Neu03] Neunhöffer, T., Die Entwicklung eines Verfahrens zur Suche nach kosmischen Neutrino-Punktquellen mit dem AMANDA-Neutrinoteleskop, Ph.D. thesis, Universität Mainz (2003).

[NMB93] Nellen, L., Mannheim, K., and Biermann, P. L., Neutrino production through hadronic cascades in AGN accretion disks, *Phys. Rev. D* **47**:5270 (1993).

[NS02] Neronov, A. and Semikoz, D., Which blazars are neutrino loud?, *Phys. Rev. D* **66**:123003 (2002).

[Olb03] Olbrechts, P., Search for Muons from WIMP Annihilation in the Center of the Earth with the AMANDA-B10 Detector, in [K$^+$03], 1677 (2003).

[OW01] Olbrechts, P. and Wiebusch, C., On the Angular Sensitivity of Optical Modules in Ice, AMANDA Internal Report 20010102 (2001).

[Pad99] Padovani, P., High Energy Emission from AGN and Unified Schemes, in F. Giovannelli and G. Mannocchi (eds.), Vulcano Workshop "Frontier Objects in Astrophysics and Particle Physics", volume 65, 159 (1999), arXive:astro-ph/9901130.

[Pan96] Pandel, D., Bestimmung von Wasser - und Detektorparametern und Rekonstruktion von Myonen bis 100 TeV mit dem Baikal-Neutrinoteleskop NT-72, Diploma thesis, Humboldt-Universität zu Berlin, Germany (1996).

[PDR03] Protheroe, R., Donea, A.-C., and Reimer, A., TeV gamma rays and cosmic rays from the nucleus of M87, a mis-aligned BL Lac object, *Astropart. Phys.* **19**:559 (2003).

[Pee73] Peebles, P. J. E., Statistical Analysis of Catalogs of Extragalactic Objects, *Astrophys. J.* **185**:413 (1973).

[RC01] Rhode, W. and Chirkin, D., Muon Monte Carlo: a new high-precision tool for muon propagation through matter, in [HKS01], 1017, Hamburg, Germany (2001).

[Rib02] Ribordy, M., AMANDA-II/2000 data statistics, OM selection and retriggering procedure, AMANDA Internal Report 20020601 (2002).

[RMS91] Ritter, H., Martinez, T., and Schulten, K., Neuronale Netze – Eine Einführung in die Neuroinformatik selbstorganisierter Netzwerke, Addison-Wesley, 2nd edition (1991).

[RS] Resconi, E. and Schönert, S., A novel wavelength shifter based on a fluorothermoplastic substrate (THV-WLS): a leap in the future?, prepared for submission to *Nucl. Instr. Meth. A*.

[Spi03] Spiering, C., High Energy Neutrino Telescopes, *Nucl. Phys. B (Proc. Suppl.)* **125**:1 (2003).

[SS96] Stecker, F. W. and Salamon, M. H., High energy neutrinos from quasars, *Space Sci. Rev.* **75**:341 (1996).

[Ste02] Steffen, P., Direct-Walk II, AMANDA Internal Report 20020201 (2002).

[Ste04] Steele, D. A., A Search for Extraterrestrial Point Sources of Neutrinos with AMANDA-II, Ph.D. thesis, University of Wisconsin (2004).

[Sud01] Sudhoff, P., Transmission measurements with Amanda Glass and Evaluation for IceCube, AMANDA Internal Report 20010701 (2001).

[Tab02] Taboada, I., Search for High Energy Neutrino Induced Cascades, Ph.D. thesis, University of Pennsylvania (2002).

[U+00] Uchihori, Y. *et al.*, Cluster analysis of extremely high energy cosmic rays in the northern sky, *Astropart. Phys.* **13**:151 (2000).

[War84] Warren, S. G., Optical constants of ice from the ultraviolet to the microwave, *Applied Optics* **23**:1206 (1984).

[WB97] Waxman, E. and Bahcall, J., High Energy Neutrinos from Cosmological Gamma-Ray Burst Fireballs, *Phys. Rev. Lett.* **78**:2292 (1997).

[Wie99] Wiebusch, C., Muon reconstruction with AMANDA, in C. Spiering (ed.), Proceedings of Workshop on Simulation and Analysis Methods for Large Neutrino Telescopes, 302, Zeuthen, Germany (1999), DESY-Proc-1999-01.

[Wos99] Woschnagg, K., Matching/combining laser/drill geometries (1999), URL `http://amanda.berkeley.edu/kurt/interstring/matchgeo.html`.

[Wos00] Woschnagg, K., Preliminary (Non-Optical) Position Calibration of Strings 14 to 19, AMANDA internal report 20001002 (2000).

[WP01] Woschnagg, K. and Price, P. B., Temperature Dependence of Absorption in Ice at 532 nm, *Appl. Opt.* **40**:2496 (2001).

[You01] Young, S. M., A Search for Point Sources of High Energy Neutrinos with the AMANDA-B10 Neutrino Teslescope, Ph.D. thesis, University of California, Irvine (2001).

Appendix A

Minimum bias comparison

The following figures show comparisons between the minimum bias event samples for experimental data and atmospheric muon simulation. These event samples are used for the estimation of systematic uncertainties due to imprecisely simulated distributions of the NN input variables (cf. section 6.6.5).

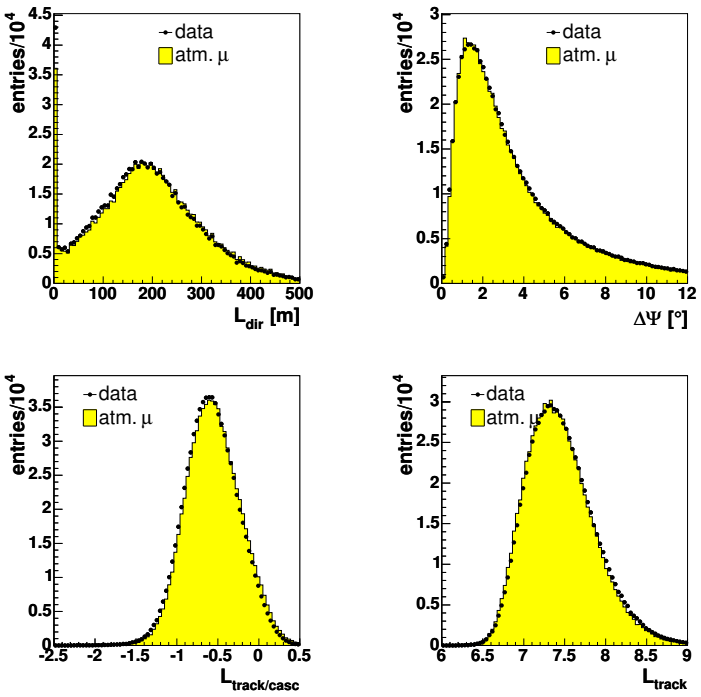

Figure A.1: One-dimensional distributions of the observables used for the calculation of the event quality Q_{NN}. Smoothness and number of direct hits are shown in Fig. 6.14.

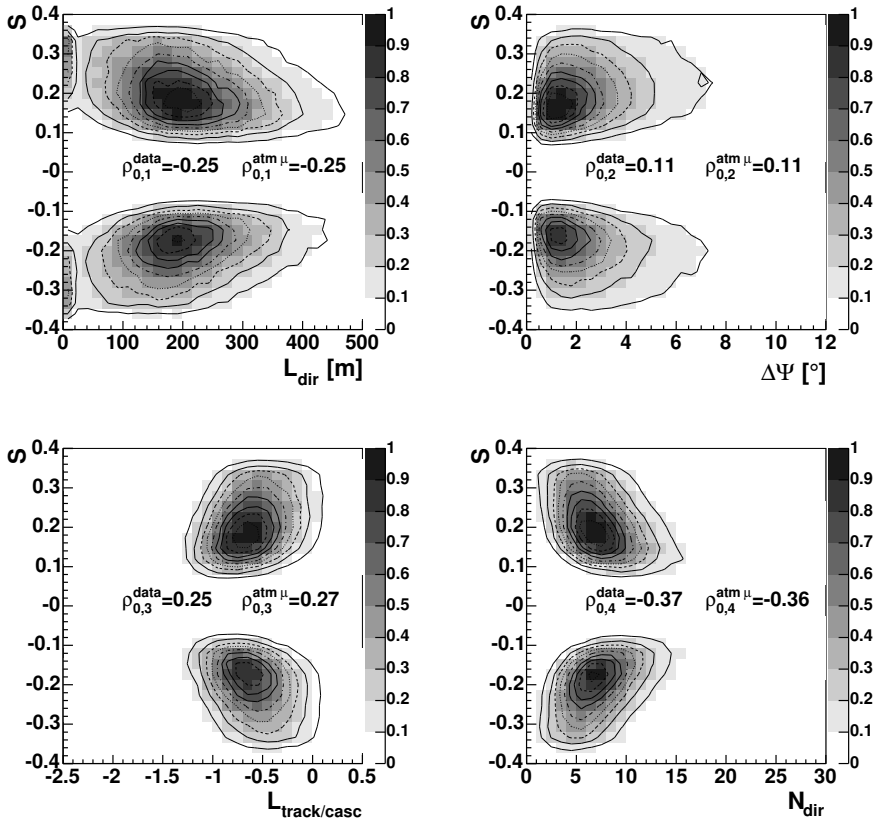

Figure A.2: Two dimensional distributions of the observables used for the calculation of the event quality Q_{NN}.

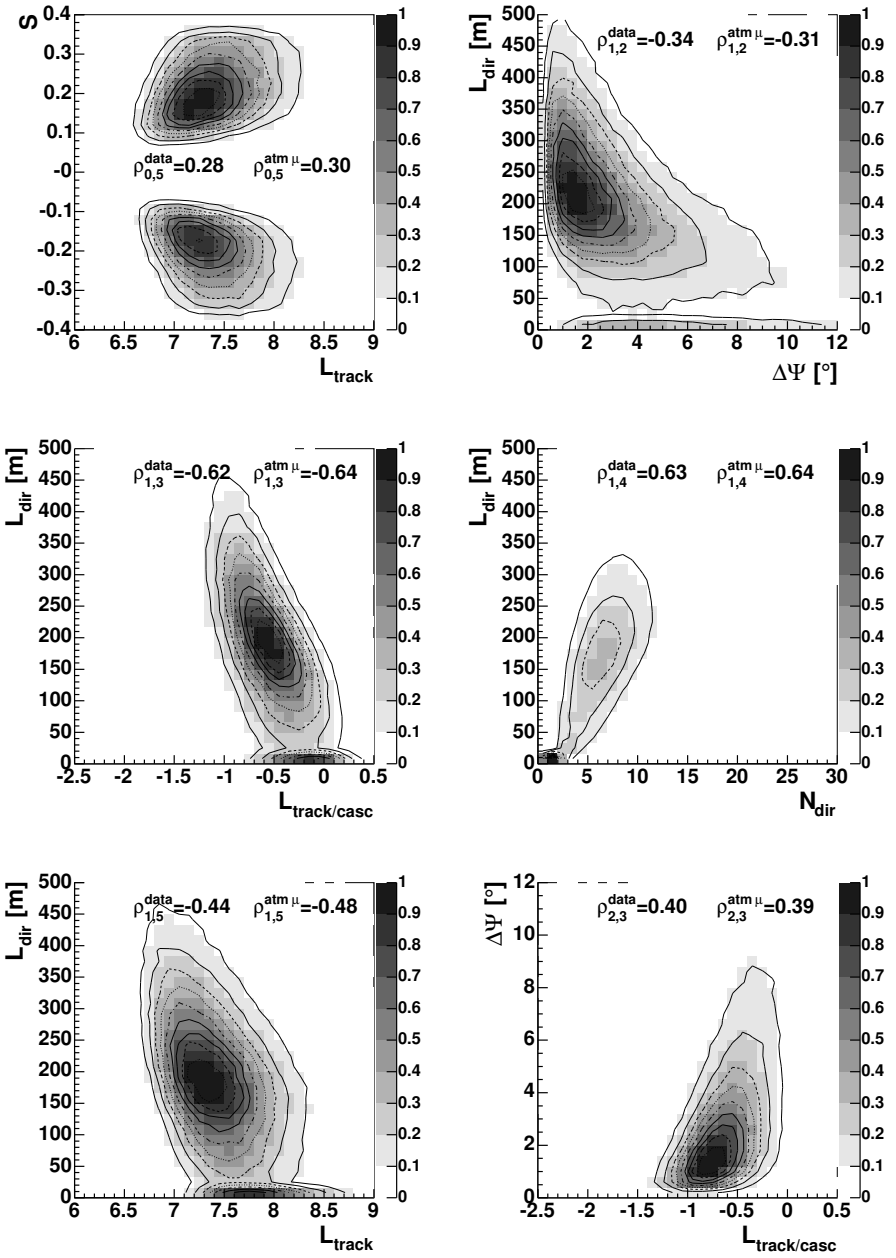

Figure A.3: Two dimensional distributions (continued).

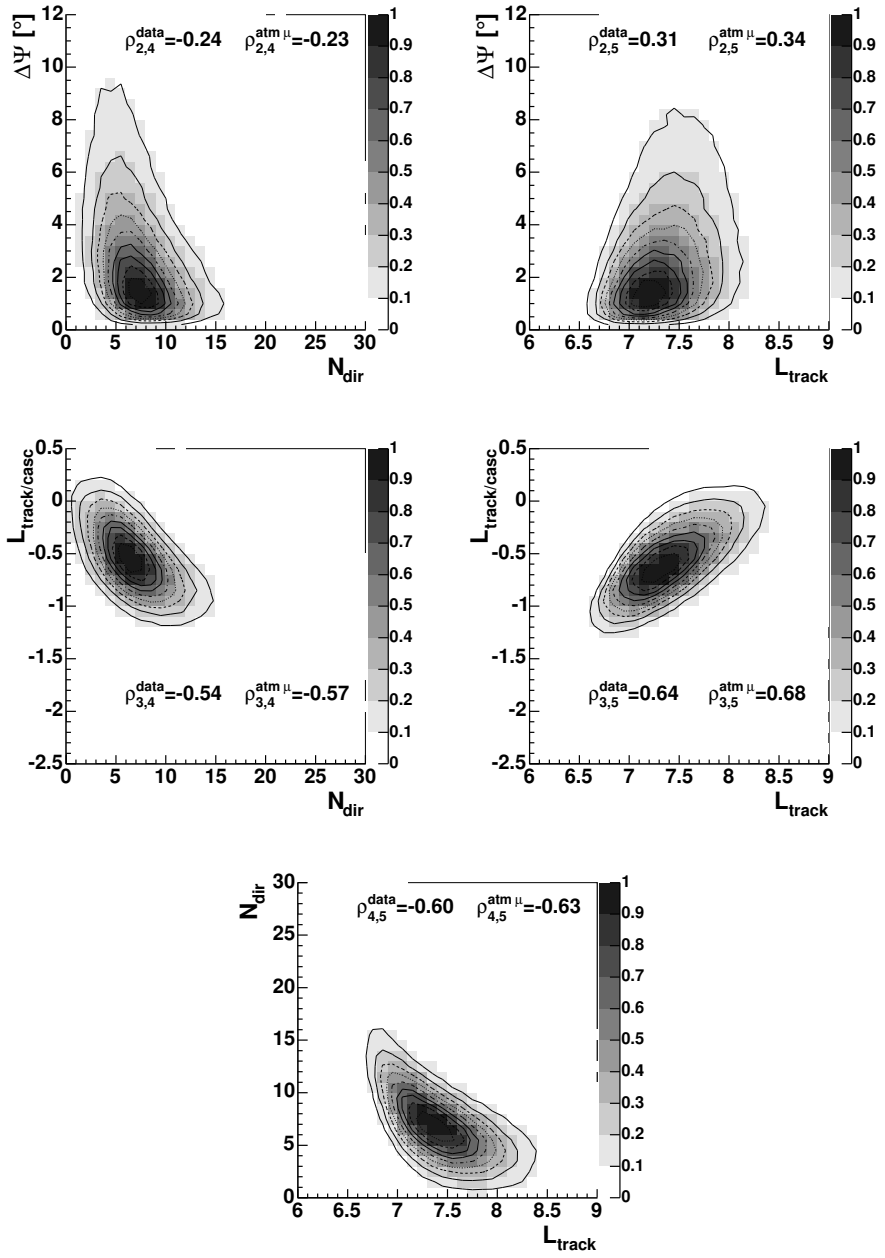

Figure A.4: Two dimensional distributions (continued).

Appendix B

Data Processing

The following tables list the programs executed for low level processing (up to level 2, Tab. B.1) and for the final reconstructions (Tab. B.2). The programs are contained in the AMANDA analysis package "Siegmund", documented in [AC03]. A more detailed description of the processing and filtering steps can be found in [Hau02]. Tab. B.3 contains the parameters for the calculation of the NN quality according to (6.15).

Command	Description
`reader`	Conversion binary - "f2k" data format
`deff -v -Y -yN=3 -yN=18 ... -yb=75:2000:1:307 -yb=5:2000:308:316 ...`	Removal of rejected OMs and TOT cleaning
`deff -Y -yN=303:310 ... -yN=555:596`	Removal of string 17 and distant OMs
`soff -v -e100`	Selection of multiplicity trigger
`amacalib -v -D ./Db/vmecal.db`	TDC correction
`soff -v -O 24:2500 -yu=9 -yu=10`	Retriggering
`deff -v -P 22875:2000:8000:all`	ADC assignment to all hits in same channel
`amacalib -Z`	Undo previous calibration
`amacalib -v -Aa -y0:20975 -D omdb-00-20010926.amacalib.txt -z`	ADC/TDC calibration
`deff -v -D -19000.`	Time shift
`deff -Y -yR=-2000:4500`	TDC time window
`deff -v -Y -yu=9 -yu=10 -yu=11 -ya=0.1:1000 -yI=100.:500.:1`	Removal of low ADC hits and "isolated" hits
`recoos -v -yu=9 -yu=10 -yu=11 -rn -is -Xg=n -Xs=n`	"Direct walk" reconstruction
`muff -v -Y zenith(1)>70`	Cut on reconstructed zenith angle
`recoos -v -yu=12 -mx -rg -pM=16 -pL=0. -if -Xg=n -Xs=c -za_upandel -pf=1 -lxyzza -xx:step=40,y:step=40,z:step=40,zenith:step=0.1, azimuth:step=0.2 -pn=1000:5000 -pj=15 -pa=96. -pt=1:5 -Xo=2`	Likelihood track reconstruction
`muff -v -Y zenith(2)>70`	Cut on reconstructed zenith angle
`muff -v -Y zenith(2)>80`	Tighter cut
`recoos -v -mx -rg -pM=16 -pL=0. -if -pf=2 -Xg=f -Xs=c -z a_upandel_mpe -l xyzza -x x:step=40,y:step=40,z:step=40,zenith:step=0.1,azimuth:step=0.2 -yA=1 -yu=12 -pn=1000:5000 -pj=15 -pa=96. -pt=1:5 -Xo=2`	MPE reconstruction
`recoos -v -mx -rg -pM=16 -pZ=0.:1. -if -pf=2 -Xg=n -Xs=c -z a_upandel+a_zenith_range+a_zwght3 -x x:step=40,y:step=40,z:step=40,zenith:step=0.1, azimuth:step=0.2 -yu=12 -pn=1000:5000 -pj=15 -pa=96. -pt=1:5 -Xo=2`	Zenith restricted reconstruction
`recoos -v -rn -im -Xg=f -pw=0. -Xs=o -yu=12 -yA=1 -pt=1:4 -pn=1000:5000 -pj=15 -pa=96. -pt=1:5 -Xo=2`	"Line fit"
`recoos -v -rn -id -Xg=f -Xs=c -yu=12 -yA=1 -pt=1:4 -pn=1000:5000 -pj=15 -pa=96. -pt=1:5 -Xo=2`	"Dipole fit"
`recoos -v -rn -ii -pp=e- -Xg=f -pw=1. -Xs=n -z user -yu=12| -yu=12 -yA=1 -pt=1:4 -pn=1000:5000 -pj=15 -pa=96. -pt=1:5 -Xo=2`	"Tensor fit"
`recoos -v -mp -pm=0 -rm -rm -if -pp=e- -Xg=n -Xs=n -z a_pp_upandel -l xyzt -x x,y,z,time -pf=7 -yu=12 -pn=1000:5000 -pj=15 -pa=96. -pt=1:5 -Xo=2`	Likelihood cascade reconstruction

Table B.1: Programs executed for the processing and filtering of AMANDA-II data up to level 2.

Command	Description
`deff -v -D 19000`	Cancel time shift
`amacalib -Z`	Cancel calibration
`xt-filt -yu=12 -yb=200:2000:87:87 ... -a87:302 -t20. -p20. -b adc_tot_2000-20020524.fit -m -d -f 40`	Cross talk filter
`amacalib -v -G -Aa -y0:20975 -D omdb-00-20010926.amacalib.txt -z`	Redo calibration
`deff -v -D -19000.`	Redo time shift
`recoos -v -mx -rg -pM=16 -if -pf=2 -z a_upandel -l xyzza -x x:step=40,y:step=40,z:step=40,zenith:step=0.1 azimuth:step=0.2 -pn=1000:5000 -pj=15 -pa=96. -pt=1:5 -Xo=2 -Xg=n -Xs=c -yu=13`	Likelihood track reconstruction
`recoos -v -mx -rg -pM=16 -if -pf=9 -pZ=0.:1. -z a_upandel+a_zenith_range+a_zwght3 -l xyzza -x x:step=40 y:step=40,z:step=40,zenith:step=0.1,azimuth:step=0.2 -pn=1000:5000 -pj=15 -pa=96. -pt=1:5 -Xo=2 -Xg=n -Xs=c -yu=13`	Zenith restricted reconstruction
`recoos -v -mx -rg -pM=16 -pL=0. -if -pf=9 -Xg=f -Xs=c -z a_upandel_mpe -l xyzza -x x:step=40,y:step=40 z:step=40,zenith:step=0.1,azimuth:step=0.2 -yA=1 -yu=13 -pn=1000:5000 -pj=15 -pa=96. -pt=1:5 -Xo=2`	MPE reconstruction
`topf -TSC -v -i 8 -yu=13`	Smoothness calculation
`nn_rdmc_v1 -v -yu=13 -k kernel_xt_v1.txt`	NN qual. calculation

Table B.2: Programs executed for the processing of AMANDA-II data to the final level.

$w_{00}^{(1)} = -0.050$	$w_{01}^{(1)} = -3.257$	$w_{02}^{(1)} = 0.205$	$w_{03}^{(1)} = 1.367$	$w_{04}^{(1)} = -0.043$	$w_{05}^{(1)} = 1.423$	$b_0^{(1)} = -0.114$
$w_{10}^{(1)} = -1.346$	$w_{11}^{(1)} = 0.232$	$w_{12}^{(1)} = -0.384$	$w_{13}^{(1)} = 2.321$	$w_{14}^{(1)} = -2.342$	$w_{15}^{(1)} = 0.376$	$b_1^{(1)} = -1.007$
$w_{20}^{(1)} = 0.699$	$w_{21}^{(1)} = -1.124$	$w_{22}^{(1)} = -0.322$	$w_{23}^{(1)} = -1.774$	$w_{24}^{(1)} = 0.573$	$w_{25}^{(1)} = -1.340$	$b_2^{(1)} = -1.064$
$w_{30}^{(1)} = 0.748$	$w_{31}^{(1)} = 1.683$	$w_{32}^{(1)} = 4.713$	$w_{33}^{(1)} = 1.334$	$w_{34}^{(1)} = 1.974$	$w_{35}^{(1)} = 1.121$	$b_3^{(1)} = -0.848$
$w_{40}^{(1)} = -2.453$	$w_{41}^{(1)} = 0.406$	$w_{42}^{(1)} = -0.698$	$w_{43}^{(1)} = -5.449$	$w_{44}^{(1)} = 1.346$	$w_{45}^{(1)} = -5.268$	$b_4^{(1)} = 5.104$
$w_{50}^{(1)} = -1.259$	$w_{51}^{(1)} = 3.486$	$w_{52}^{(1)} = -1.753$	$w_{53}^{(1)} = -0.118$	$w_{54}^{(1)} = 2.799$	$w_{55}^{(1)} = -1.281$	$b_5^{(1)} = 0.251$
$w_{00}^{(2)} = -2.378$	$w_{01}^{(2)} = -1.834$	$w_{02}^{(2)} = -0.147$	$w_{03}^{(2)} = -2.365$	$w_{04}^{(2)} = 5.197$	$w_{05}^{(2)} = 1.875$	$b_0^{(2)} = -3.103$

Table B.3: Weights $w_{ij}^{(l)}$ and thresholds $b_i^{(l)}$ for the calculation of the NN quality.

Erklärung

Hiermit erkläre ich, die vorliegende Arbeit selbständig ohne fremde Hilfe verfasst und nur die angegebene Literatur und Hilfsmittel verwendet zu haben. Ich habe mich anderwärts nicht um einen Doktorgrad beworben und besitze keinen Doktorgrad. Die Promotionsordnung der Mathematisch-Naturwissenschaftlichen Fakultät I der Humboldt-Universität ist mir bekannt.

Tonio Hauschildt
7. April 2004

List of publications

Refereed journals

(principal authorship in the 5. listed publication)

1. M. Ackermann *et al.*, "Search for neutrino induced cascades with AMANDA", Astropart. Phys. **22**, 127 (2004).

2. J. Ahrens *et al.*, "Measurement of the cosmic ray composition at the knee with the SPASE-2/AMANDA-B10 detectors", Astropart. Phys. **21**, 565 (2004).

3. J. Ahrens *et al.*, "Muon Track Reconstruction and Data Selection Techniques in AMANDA," Nucl. Instrum. Meth. A **524**, 169 (2004).

4. J. Ahrens *et al.*, "Calibration and survey of AMANDA with the SPASE detectors," Nucl. Instrum. Meth. A **522**, 347 (2004).

5. J. Ahrens *et al.*, "Search for Extraterrestrial Point Sources of Neutrinos with AMANDA-II", Phys. Rev. Lett. **92**, 071102 (2004).

6. J. Ahrens *et al.*, "Sensitivity of the Icecube Detector to Astrophysical Sources of High Energy Muon Neutrinos", Astropart. Phys. **20**, 507 (2004).

7. J. Ahrens *et al.*, "Limits on diffuse fluxes of high energy extraterrestrial neutrinos with the AMANDA-B10 detector", Phys. Rev. Lett. **90**, 251101 (2003).

8. J. Ahrens *et al.*, "Search for point sources of high energy neutrinos with AMANDA", Astrophys. J. **583**, 1040 (2003).

9. J. Ahrens *et al.*, "Search for neutrino-induced cascades with the AMANDA detector", Phys. Rev. D **67**, 012003 (2003).

10. J. Ahrens *et al.*, "Observation of high energy atmospheric neutrinos with the Antarctic Muon and Neutrino Detector Array", Phys. Rev. D **66**, 012005 (2002).

11. J. Ahrens *et al.*, "Limits to the muon flux from WIMP annihilation in the center of the earth with the AMANDA detector", Phys. Rev. D **66**, 032006 (2002).

Selected conference proceedings

T. Hauschildt and D. Steele, "Search for Extraterrestrial Point Sources of Neutrinos with AMANDA-II", in "Proceedings of the 28th International Cosmic Ray Conference", Tsukuba, Japan, eds. T. Kajita *et al.*, p. 1305 (2003).